THE GLASS SASHIMONO JOINT

DESIGNING A RIGID AND DEMOUNTABLE CONNECTION FOR A PORTAL FRAME

THE GLASS SASHIMONO JOINT

DESIGNING A RIGID AND DEMOUNTABLE CONNECTION FOR A PORTAL FRAME

Graduation thesis

to obtain the degree of Master of Science
at the Technische Universiteit Delft,
to be defended publicly on Friday April 14, 2023 at 15:00.

by

Helene Catherina BOUWMEESTER

Graduation committee:

Dr. ir. F.A. Veer,	Chair, Technische Universiteit Delft
Ir. C. Noteboom,	Technische Universiteit Delft
Dr. F. Messali,	Technische Universiteit Delft
Ir. E.H.J. ten Brincke,	ABT bv





Front: Picture of the Kanawa and Gooseneck samples for the tensile tests.

An electronic version of this dissertation is available at
http://repository.tudelft.nl/.

Vaak verwarren we verwachtingen met vertrouwen.
In onze families, bij het behalen van onze doelen en ook in onszelf.
Maar waar verwachtingen slechts teleur kunnen stellen en beklemmen,
zal vertrouwen groeien. En allerbelangrijkst, verrassen.

Opa Kees, mijn trouwste supporter.
Helaas deze eindstreep zelf net niet gehaald.

Contents

Summary xi

1 Intro 1
- 1.1 Problem statement . . . 2
- 1.2 Research questions . . . 3
- 1.3 Research methodology . . . 4

I Theoretical framework 7

2 Glass connections 9
- 2.1 Mechanical connections . . . 9
  - 2.1.1 Bolted connections . . . 10
  - 2.1.2 Embedded connections . . . 11
- 2.2 Adhesive connections . . . 12
- 2.3 Conclusions and discussion . . . 14

3 Material properties 15
- 3.1 Glass characteristics . . . 15
  - 3.1.1 Composition . . . 15
  - 3.1.2 Structure . . . 16
  - 3.1.3 Properties . . . 17
  - 3.1.4 Fracture behaviour . . . 18
  - 3.1.5 Glass processing . . . 20
- 3.2 Interlayers . . . 25
  - 3.2.1 Previously used materials . . . 26
  - 3.2.2 Criteria . . . 26
  - 3.2.3 Friction coefficients . . . 28
  - 3.2.4 Material selection . . . 29
- 3.3 Conclusions . . . 31

4 Sashimono 35
- 4.1 Tsugite . . . 36
  - 4.1.1 Combinations . . . 44
- 4.2 Shiguchi . . . 46
- 4.3 Conclusions and discussion . . . 47

II Design 49

5 Analytical modelling 51
- 5.1 Physical models . . . 51

5.2 Sketches . . . 53
5.2.1 Gooseneck under tension . . . 53
5.2.2 Gooseneck under bending . . . 56
5.2.3 Kanawa under tension . . . 58
5.2.4 Kanawa under bending . . . 59
5.3 Hand calculation . . . 62
5.3.1 Gooseneck under tension . . . 62
5.4 Conclusions . . . 63

6 Numerical modelling **65**
6.1 General model description . . . 65
6.1.1 Grasshopper setup . . . 65
6.1.2 Finite element model . . . 66
6.2 Design choices . . . 70
6.3 Results . . . 72
6.4 Sensitivity analysis . . . 76
6.4.1 Friction coefficient . . . 76
6.4.2 Stiffness interlayer material . . . 78
6.5 Conclusions and discussion . . . 80

III Experimental research **83**

7 Experimental research **85**
7.1 Interlayer . . . 86
7.1.1 Cutting . . . 86
7.1.2 Direct assembly . . . 86
7.1.3 Assembly after heating . . . 87
7.1.4 Alternative assembly . . . 89
7.2 Tensile tests . . . 91
7.2.1 Description setup . . . 91
7.2.2 Results . . . 95
7.2.3 Comparison finite element analysis . . . 100
7.2.4 Failure mechanism . . . 105
7.2.5 Conclusions and recommendations . . . 107
7.3 Bending tests . . . 113
7.3.1 Description setup . . . 113
7.3.2 Results . . . 118
7.3.3 Comparison FEA . . . 120
7.3.4 Failure mechanism . . . 122
7.3.5 Stiffness joint . . . 124
7.3.6 Conclusions and recommendations . . . 126

IV Conclusions and recommendations **133**

8 Conclusions and recommendations **135**
8.1 Subquestions . . . 135
8.2 Main research question . . . 139

8.3 Recommendations . . . 140
8.3.1 Design geometry . . . 140
8.3.2 Production . . . 141
8.3.3 Interlayer . . . 141
8.3.4 Glass type . . . 142
8.3.5 Out of plane behaviour . . . 143
8.3.6 Validation . . . 143
8.3.7 Global structure . . . 143

Acknowledgements **145**

V Appendices **151**

A Calculations **153**
A.1 Stresses Sashimono . . . 153
A.1.1 Gooseneck . . . 153
A.1.2 Kanawa . . . 157
A.2 Dimensions tensile tests . . . 163
A.2.1 Shear strength bolts . . . 163
A.2.2 Bearing resistance plate . . . 163
A.2.3 Tensile resistance plates . . . 164
A.2.4 Yielding resistance plates . . . 164

B Numerical models **165**
B.1 Grasshopper models . . . 165
B.1.1 Gooseneck model . . . 165
B.1.2 Kanawa model . . . 168

C Material properties **173**
C.1 EduPack data . . . 174
C.1.1 Surlyn . . . 174
C.1.2 PVC . . . 175
C.1.3 PA6 . . . 176
C.1.4 POM . . . 177
C.2 Supplier data . . . 180
C.2.1 PVC . . . 180
C.2.2 PA6 . . . 182
C.2.3 POM . . . 183
C.2.4 PU . . . 184
C.2.5 Araldite . . . 185

D Derivations **191**
D.1 Definition axes . . . 191
D.2 Mechanical scheme portal frame . . . 191
D.3 Deflection four point bending . . . 193

SUMMARY

Glass is gaining more and more popularity as a structural material and has become a big share of the building industry. Unfortunately, the building industry is the largest polluter in terms of industrial waste and is responsible for 40% of Europe's energy demand (CIB, 1999), and glass is also playing a significant role in this number. One strategy to reduce the amount of pollution from a product or industry is by making it circular (PBL, 2019). Meaning the amount of waste is minimized and the energy needed to produce new material is also decreased. In the Netherlands, buildings have to be completely circular from 2050 (Rijksoverheid, 2016). In order for glass to contribute to this goal, elements have to be able to be reused or recycled, taking demountability into account during the design of a structure.
One way of creating such a demountable joint, is by making use of portal frames, which require a rigid connection between the columns and beams. Currently, this connection is designed using either mechanical connections or adhesives. Rigid mechanical connections are visually not aesthetically pleasing and cause impurities right at the points where stresses are highest. This makes the joint more sensitive to failure. Rigid adhesive connections are very prone to execution and design errors, and are uncertain regarding their long-term strength. Currently, there is no efficient way to properly remove adhesives, making them non-demountable joints. This research will therefore design a demountable and rigid joint using contact pressure, taking inspiration from traditional Japanese joinery. To develop this joint, first, theory is studied, followed by the design and lastly by experimental testing.

From literature, the Kanawa and Gooseneck joints are selected, because they have the capacity to take up both shear and a bending moment. These joints are then further optimized to determine the optimal geometry for a rigid glass joint. This means a geometry that minimizes tensile stresses in the glass, decreasing the chance an existing flaw will tear and cause the material to fail. This optimization is done using analytical and numerical analyses, followed by full-scale experiments. To determine the optimal force transfer the geometries were first schematized, and the relevant parameters were determined for later variation. From hand calculations, it follows that the optimal geometry finds a balance between the stresses resulting from normal force and the stresses resulting from the eccentricity of the internal line of force.

Using a parametric Grasshopper model, the geometries are further optimized by varying dimensions and curvature. Several designs are imported into DIANA FEA and Abaqus to acquire numerical values for the expected stresses of these set parameters. The models are set up as two 2D glass panes with a polymer interlayer in between them. In DIANA FEA a lot of difficulties arose with the combination of complex geometry and multiple contact surfaces. Therefore all designs were mitigated to Abaqus, because this software

is more suitable for complex contact surfaces. Comparing the heavily simplified hand calculations to the FEA, there was a constant increase of peak stresses with a factor of 4.

The Gooseneck design was manufactured using a CNC milling machine and afterwards, its edge was polished, resulting in optimal edge quality. Due to the nature of the geometry, the Kanawa design had to be manufactured using a waterjet. There was a large difference between the accuracy of the two production methods, resulting in the Kanawa joint having a lot more space between the glass plates. This strongly influences the placement of the interlayer materials, but also the stiffness of the joint during the experiments.

Before these models could be validated using experiments, a suitable interlayer to place between the edges of the glass panes was researched. POM, PVC, Surlyn, PA6 and PU85 are deemed suitable and are examined. Eventually, only PU85 could be fitted between the glass panes, which seemed to have the least favourable mechanical properties. The angle of the geometry was too small for most materials to bend them into, even after heating the plastics. The other issue lay with the tight tolerances of the polished glass panes. These had to be additionally polished by hand and the PU85 was treated with silicone spray, in order for the whole joint to fit. The disadvantage was that this manual polishing damaged the edge quality, increasing the probability of failure at a lower strength.

Experiments were then conducted to validate earlier analytical and numerical calculations, using full-scale single-pane annealed glass. The joints were tested in pure tension and a bending moment, using polarizing filters to visualize the stress trajectories. For the Gooseneck model, the stress trajectories and expected stiffness corresponded well with the models. The samples failed at an average force of 6.0 kN. The model predicted peak stresses of 300 N/mm^2 and stiffness of 2.8 N/m at this point, the experiments displayed a stiffness of 3.0 N/m. This means the model turned out to be 5.7% less stiff than the experiments.

The stress trajectories coincided less clearly with the model for the Kanawa tension model. The samples failed at an average force of 4.1 kN. The expected peak stresses at this point were 150 N/mm^2 and the stiffness 0.73 N/m based on the model. The experiments showed a stiffness of 1.1 N/m. The model underestimates the stiffness of the experiments by 33%.

Interestingly, because the tolerances in the Kanawa joint were larger, there was more movement possible in this joint. This influenced the force transfer and therefore resulted in different peak stresses than expected. The Gooseneck model turned out to be almost 3 times as stiff as the Kanawa model. This has two likely reasons. First of all, the geometry of the Kanawa joint is not designed to take up pure tension in the direction that it was tested. Therefore, the geometry itself was a lot less stiff than that of the Gooseneck joint. Secondly, the tolerances were of large influence. Because the Kanawa samples were produced using a waterjet, with quite large tolerances, there was a lot of movement possible in the joint. This meant little force was necessary to displace the joint, resulting

in a lower stiffness.

The Kanawa design was tested under a bending moment, because the force transfer is very different compared to pure tension for this design. The full beam had dimensions of 2400 mm x 400 mm x 10 mm. Locations of peak stresses were similar to the models. The samples failed at an average of 4.0 kN, which corresponds with a moment of 1.1 kNm. The force-displacement graph of the experiments was not linear, but showed varying stiffness with plateaus where the stiffness was around 0. Most likely, this was caused by a combination of the plastic deformation of the PU85 and movement and/or sliding in the machine itself. It was attempted to calibrate the model to the experiments, by increasing the stiffness of the interlayer. This did not result in sufficient stiffness, which implies the stiffness originates from another element in the setup. The rotational stiffness was 611 kNm/rad, which is 9.1% of the stiffness compared to a solid beam of the same dimensions.

This means the designed joint is not fully rigid, but this exploratory study shows there is great potential for such a system. Further optimizing the geometry and finding a more suitable interlayer could result in a rigid and demountable glass joint, as part of a portal frame.

1

Intro

Glass architecture speaks to the imagination of many designers and users, due to its transparency and strength. It allows for lightness in a structure, both in the sense of daylight and in that of structural elegance. For this reason, it is gaining more and more popularity as a structural material and is becoming an increasing share of the building industry.
Unfortunately, the building industry is the largest polluter in terms of industrial waste and is responsible for 40% of Europe's energy demand (CIB, 1999). Currently, glass is playing a significant role in this, having high shadow costs and producing lots of waste material. The problem with glass is that it is produced at 1600-1800 degrees Celsius (Haldimann et al., 2008), requiring a lot of energy. This energy is mostly produced in a non-sustainable way.

One strategy to reduce the amount of pollution from a product or industry is by making it circular (PBL, 2019). Meaning the amount of waste is minimised and the energy needed to produce new material is also decreased. In the Netherlands, buildings have to be completely circular from 2050 onward (Rijksoverheid, 2016). Glass is very well recyclable without loss of strength. However, this hardly happens in practice. In the Netherlands, approximately 5-10% of float glass is recycled and put back onto the float glass market (Nederland, 2021). Progress is being made to increase this number, but as can be seen in Figure 1.1 the reuse of material is a more efficient way than recycling to reduce waste and CO_2 emissions. Research by Tuna Kayılı et al., 2016 shows that if laminated glass is reused, a tenfold saving of energy and a fourfold saving of CO_2 can be achieved. In order to be able to reuse or recycle glass elements, they have to be demountable from the structure. This means that demountability has to be taken into account during the design of a structure.

1

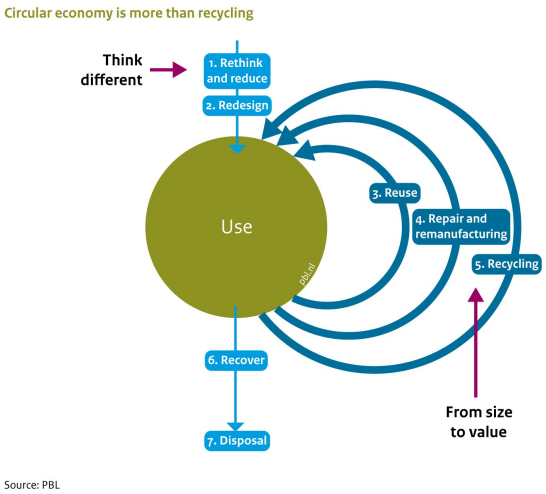

Figure 1.1: Schematic representation of a circular economy, (PBL, 2019)

Demountable glass structures could come in many different shapes and sizes. One interesting type of structure is the portal frame, providing structural stability in its plane direction. This portal frame requires moment-resisting connections between the columns and beam, of which the mechanical scheme can be found in Appendix D.2. The advantage of portal frames is that no additional stabilizing elements like a shear wall or bracing are required in this direction. This allows for a more open structure and flexibility in the design. Currently, this connection is designed making use of either mechanical connections or adhesives. Each has its own advantages and disadvantages in the aspect of structural performance, sustainability and demountability.



(a)



(b)

Figure 1.2: Example of glass portal frame in Broadfield House (a) and Ruurlo castle (b)

1.1. PROBLEM STATEMENT

Demountable connections are highly necessary to ensure a sustainable circular future for this magnificent structural material. Currently, rigid connections for a portal frame

are not satisfactory. Rigid mechanical connections are visually not aesthetically pleasing and cause high stress intensification. Rigid adhesive connections are very prone to execution and design errors, and are currently non-demountable. Existing rigid glass joints will be discussed in detail in Chapter 2.

There is however another opportunity, which is currently not being considered. Namely, what if we could connect the glass with the glass using contact pressure?

Glass is used mainly for its excellent aesthetic features. Making the connection an artwork by itself would definitely add to the quality of the construction as a whole. The principle of using contact pressure as a way of connecting elements is not new, it can be observed in nature, but more famously in Japanese wooden joinery. Sashimono is a technique of joining wooden elements without nails or screws, which has been around and admired for centuries. This research will therefore attempt to assemble the ultimate demountable connection: the Sashimono glass connection.

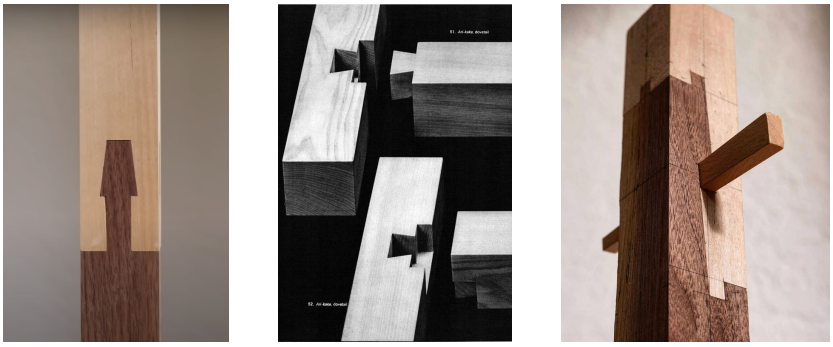

(a) (b) (c)

Figure 1.3: Examples of three Sashimono joints

Considering the disadvantages of both mechanical and adhesive connections for a glass portal frame connection, it would be worthwhile to try and execute it using contact pressure instead. This could remove many disadvantages of a mechanical rigid connection, but still be demountable and suitable for reuse and recycling. Designing and testing this connection succesfully, would allow for lots of other connections like splicing joints to be designed in a similar way.

1.2. RESEARCH QUESTIONS

The objective of this research is to show that it is possible to design a glass rigid connection using contact pressure as part of a portal frame, in order to promote the use of demountable connections in structural glass constructions. This will contribute to the

knowledge of demountable connections, allowing for more circularity in the building industry, specifically glass.

The main research question is then formulated as follows:

What is a suitable design for a rigid and demountable glass connection using contact pressure?

Subquestions to help answer the main questions are:

1. What types of rigid glass connections exist and how do they work?
2. What are relevant material properties of glass and suitable interlayers to properly interact with these properties?
3. Which types of relevant Sashimono joints exist and which would be suitable to execute in glass?
4. What is the influence of shape on force transfer and how can this interaction be optimized in a glass Sashimono connection design?
5. What is the failure behaviour of the designed Sashimono connection?

1.3. RESEARCH METHODOLOGY

For this research approach, each subquestion will be evaluated and a suitable strategy will be chosen. Each question and its corresponding strategy can be found in the table below. The main research question will thus be answered using a mix of the case study and desk research strategy. In this research, many different research methods are used, namely, design, literature research, numerical research and experimental research.

The first research question aims to dive further into the problem statement. Existing rigid joints in glass will be discussed along with their advantages and disadvantages. By consulting literature on structural glass joints, an overview of existing rigid joints can be generated. This can be used as input for the design of the Sashimono joint.

Since this research will mainly look at a structure in the material glass, it is important to understand its properties for optimal design and properties. What are its weaknesses and its strengths, and which properties require additional attention? To connect the glass elements, an interlayer will be required. Which ones have been researched and applied in the past and how do they support the optimal behaviour of glass? For the final design and modelling, an overview of these properties would be very useful. The easiest way to generate this data is through a literature survey, which is therefore used as a strategy for the second research question.

In order to be designing a specific Sashimono connection, it is relevant to investigate

existing Sashimono joints and their applicability to a glass connection. Using a literature survey, a lot of data can be quickly generated analyzing material produced by others (Verschuren and Doorewaard, 2010). This is a method to create an overview of existing options, including which ones work in which situation, and most importantly why. This overview can be used as a framework for the design of the glass Sashimono connection. The extensive data collection is a large advantage, however, it should be kept in mind that the objective of these research studies might be very different and the results should be interpreted accordingly.

For the fourth research question, insight is required into the influence of shape on force transfer. By using the output from the literature study, several concepts can be designed and modelled. This is first done by hand and with basic physical model making, after which this interaction in the connection can be modelled using finite element modelling. This geometry can be modelled in Grasshopper, using output from finite element modelling (FEM) to optimize the shape of the connection in an iterative process. This insight is further developed with the use of experimental testing. Analysing the stresses and behaviour of several variants enables the designer to further improve the final design. The designs will first be tested in pure tension and later under four-point bending.

Another important piece of information for the designed connection is its failure mode. Since modelling this in a finite element model is complex and outside of the scope of a graduation thesis, the best way to determine this is with experimental testing.

Question	Breadth/ depth	Quantitative/ qualitative	empirical/ non-emprical	Strategy	Variant	Method	Product
1	breadth	quantitative	empirical	desk research	literature survey	literature	overview rigid connections
2	depth	both	non-empirical	desk research	literature survey	literature	overview properties
3	breadth	qualitative	empirical	desk research	literature survey	literature	overview sashimono joints
4	depth	both	non-empirical	case study	single case study	design/numerical/experimental	models/designs joint
5	depth	qualitative	empirical	case study	-	experimental	testing results

Table 1.1: Overview research methodology, based on Verschuren and Doorewaard, 2010

I

THEORETICAL FRAMEWORK

2

GLASS CONNECTIONS

The devil is in the details and this is definitely the case for glass structures, since this is where it is most sensitive. Especially in a portal frame where the connections have to take up a moment, high stresses will occur in this area. High tensile stress concentrations can be the cause of present flaws developing to complete failure of the glass element (Katsivalis et al., 2018). Furthermore, the design of the connection can be normative for the determination of the sustainability of the designed glass structure in terms of shadow costs and demountability (Hoogerwaard, 2020). Lastly, the connection of the portal frame is a very visible part of the construction, having a great influence on its transparency and architectural quality. Herein also lies an interesting opportunity to enhance the architectural design with an elegant connection.

In this chapter, existing glass connections will be discussed. Their common use, advantages, disadvantages and execution as a rigid joint will be elaborated on. Because the objective of this research is to design a rigid portal frame, the focus of this chapter will lie on beam-column connections. The subquestion answered in his chapter is:

What types of rigid glass connections exist and how do they work?

This will give more insight into why the Sashimono joint could pose a suitable alternative to existing joints. Glass joints are mostly divided into two categories: mechanical and adhesive connections.

2.1. MECHANICAL CONNECTIONS

Mechanical connections are most commonly used in the building industry and make use of additional metals that show plastic behaviour like bolts or more structure-specific connectors (Schittich, 2007). A general great advantage of mechanical connections is that their demountability makes it possible to reuse or recycle the materials used. In this

section, bolted and embedded connections will be discussed.

2.1.1. BOLTED CONNECTIONS

Bolted connections are the most conventional connection type for many different materials, including glass. The reason is that they are relatively easy to assemble and disassemble. The connection is mostly used to transfer in-plane forces from glass components to the surrounding structure, for example in the case of glass facade panels. But they are also used to connect structural glass elements to each other, for example column to beam. Forces from one glass panel are transferred to the bolt, which then transfers the forces to the connecting (glass) panel. A schematization of this force transfer is shown in Figure 2.1. The bolt prevents sliding of the two glass panes. This causes a reaction force of the bolt onto the glass. To produce such a joint, holes are drilled through the glass panes, some sort of mortar is injected and the bolt is lastly inserted and fastened. This injection mortar is necessary to prevent contact area between the bolt and glass and to distribute the stresses over a larger surface of the glass (Schittich, 2007).

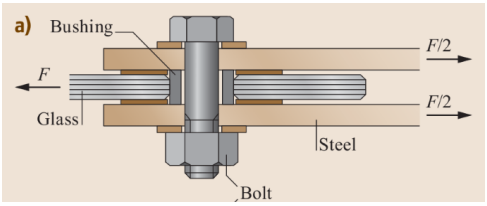

Figure 2.1: Schematic representation of a through-bolt connection, Musgraves et al., 2019

Around the drilled holes, high stress intensification will occur, which is visualized in Figure 2.2(a) and can be seen in Figure 2.2(b). This behaviour and the stress concentration factor will be discussed in Chapter 3. This stress concentration is problematic, because it increases the chance of failure of the glass. Furthermore, the drilling of the glass will result in imperfections of the edges, making this area even more susceptible to failure in case of high stresses (Haldimann et al., 2008). These two factors usually require the use of tempered glass, as well as special attention to the design and assembly of these joints (Bedon and Santarsiero, 2018).

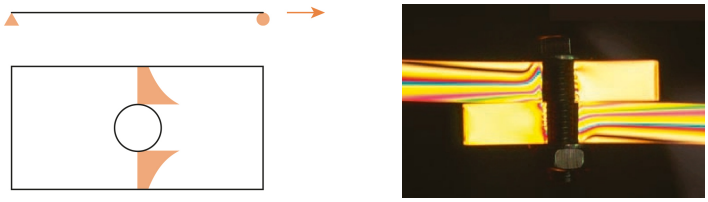

(a) (b)

Figure 2.2: Schematization of stresses around holes of a bolted connection under tension (a) and an optical display of the stressed from the side of such a bolted joint (b), (Wurm, 2007)

To enable moment capacity, a row or grid of these connectors is required to create a lever arm. These metals will always remain visible through the transparent glass and are not always desired from an architectural point of view (Afghani Khoraskani, 2015). To withstand the high stresses around the bolts due to the moment, the panel is often strengthened using extra glass or an additional metal plating, seen in Figure 2.3(b).



(a) (b)

Figure 2.3: Stresses around holes of a bolted connection under tension (a) and an example of a mechanical portal frame (b)

2.1.2. EMBEDDED CONNECTIONS

In the case of embedded connections, metal parts are inserted and glued between laminated glass. So technically, they are considered adhesive connections, but since they allow the construction to be demounted, they are still considered relevant for the objective of this research. In practice, it is mostly used to connect fins to the facade, facade panel to facade panel and rarely column to beam connections. Laminated glass is produced by stacking several glass panes with a thin silicone layer in between, called an interlayer. For the embedded connection, usually one of the panes is shortened and a metal insert is placed in this cavity. Different types of embedded connections are shown in Figure

2.4. The standard autoclave process to bond the layers is then performed including the metal insert, making it fully bonded to the glass pane (Bedon and Santarsiero, 2018).

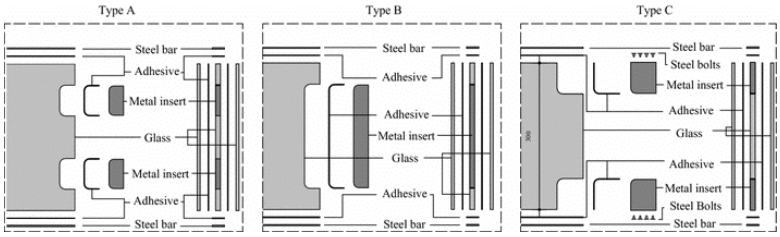

Figure 2.4: Exploded schemes of types of embedded connections, Santarsiero et al., 2017

A great advantage is that no drilling is required, which weakens the glass, nor complex bonding on site, which is prone to execution errors or environmental circumstances. Mostly titanium inserts are used, since they have the same heat expansion properties as glass and will therefore cause the least problems (Johnson, 2014). This material is however expensive and has high shadow costs. To create a moment capacity, either a wide insert is used, or two more narrow inserts, shown in Figure 2.5. The compressive part of the insert will cause high peak stresses in the glass, often being the area in which this type of joint fails (Bedon and Santarsiero, 2018). Partly because the insert cannot have a large length, its moment capacity is limited and not often used to create portal frames.

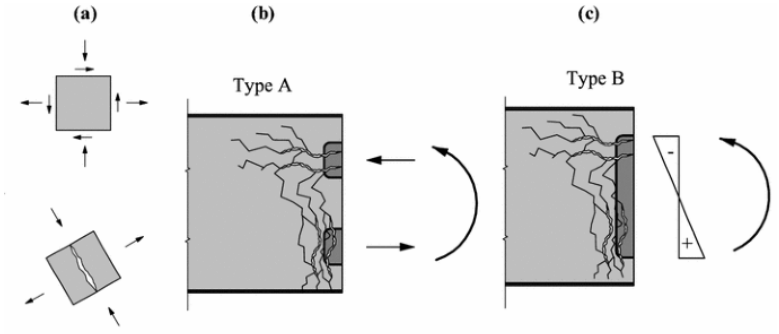

Figure 2.5: Expected failure in embedded connection under a moment in an element with two inserts (b) and one large insert (c), Santarsiero et al., 2017

2.2. ADHESIVE CONNECTIONS

Adhesive connections connect glass elements with silicone adhesives, which will, depending on the material chosen, not be visible in the connection. When using this type of connection between beam and column, it can provide sufficient moment capacity in most cases. An example is shown in Figure 2.6(a). Different from mechanical connections, where the glass is joined through the glass panels themselves, adhesive con-

nections are joined on the surface of the glass. This increases the area of force transfer, shown in red in Figure 2.6(b). Therefore adhesive connections usually result in a more equal distribution of stresses and no drilling is required (Katsivalis et al., 2018). This makes the material less vulnerable to additional flaws and thus failure in a later stage.

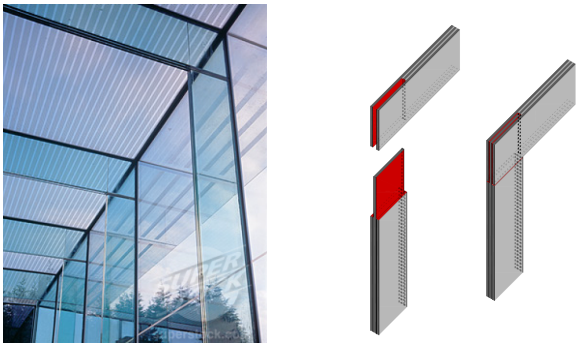

(a) (b)

Figure 2.6: Picture of adhesive connections seen in Broadfield House UK (a) and an a schematization of this same connection (b), copied from C. Louter, 2022

Since adhesive joints are loaded differently, the typical stress distributions are also quite different, seen in Figure 2.7. The properties of the adhesive itself will determine the strength of the joint. It is therefore the weakest link of the joint. Any forces out of plane of the joint, causing splitting or peeling is highly unfavourable.

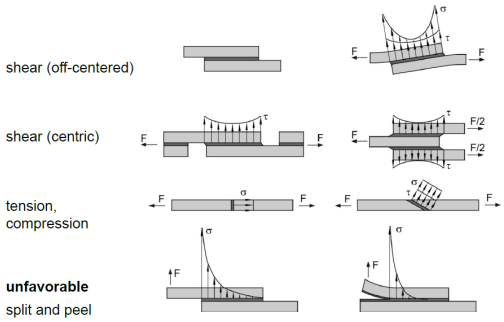

Figure 2.7: Typical stress distributions in adhesives, related to the force type, C. Louter, 2022

Several types of adhesives exist of which the main technologies are: acrylates, epoxies, polyurethanes, silicones and hybrid polymers. Each has its advantages and disadvantages in the fields of curing times, strength values, resistance against moisture, temper-

ature and UV, possibilities for removal, and degeneration of strength (Musgraves et al., 2019). As can be seen in Figure 2.8, the properties of the adhesive used is of influence on the stress distributions of the glass. The main points of attention are sensitivity to humidity and temperature, especially during assembly. Extra care should be taken to keep the assembly site dust free, since this will decrease the strength of the adhesive. In general, it can be said that adhesives are very hard to remove and would make the elements of a glass portal frame non-demountable

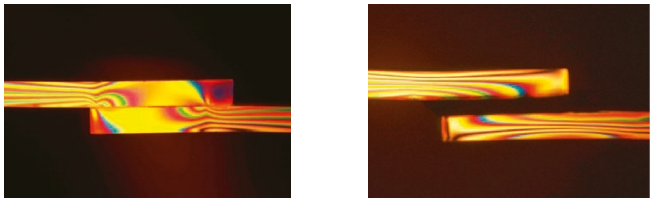

(a) (b)

Figure 2.8: Optical display of stress distribution with a hard adhesive (a) and a thick elastic adhesive (b), (Wurm, 2007)

2.3. CONCLUSIONS AND DISCUSSION

Currently several possibilities for rigid beam-column connections exist. Bolted connections create impurities right at the points where stresses are highest and therefore sensitive to failure. Additional metals for a rigid joint are also generally undesired from an architectural point of view. Costs and environmental issues considering the often used titanium for mechanical connections also pose a large disadvantage. Embedded connections seem to have limited capacity to function as a rigid joint. Especially from an aesthetic perspective, there is quite some potential for further research into this type of joint as a rigid beam-column connection.

Adhesives have the great advantage of creating a more even stress distribution in the glass and can work well as a rigid joint. When using them, however, the weakest link of the joint is the adhesives itself. It especially cannot take forces out of plane well. Adhesives are very sensitive to environmental circumstances and there is still limited data on the lifetime of structural adhesives. The strength drops severely at long term loads. Currently, there is no way to properly remove adhesives, making them non-demountable joints. Naturally, further research could prove a way to properly remove adhesives, but this is outside of the scope of this research.

A large number of joints exist outside of the examples listed in this chapter, but since this research aims to design a rigid portal frame, only existing possibilities for rigid beam-column connections were discussed.

3

MATERIAL PROPERTIES

The glass Sashimono joint, which will be designed in this research, will work purely on contact pressure. This means that forces have to be transferred through the glass via an interlayer. Proper interaction between the glass and interlayer is therefore crucial. Relevant glass properties and production methods are discussed. Possible interlayers are considered, along with their advantages and disadvantages. This data is used as input for the modelling of the joint. The subquestion answered is:

What are relevant material properties of glass and suitable interlayers to properly interact with these properties?

3.1. GLASS CHARACTERISTICS

3.1.1. COMPOSITION

The two most common types of glass are soda lime silicate glass and borosilicate glass, each having its own quantities of ingredients like silicon dioxide, calcium oxide and sodium oxide. These are listed in Figure 3.1. The primary ingredient is silicon dioxide, which is simply sand. The main difference between the two types is that borosilicate glass is more resistant to thermal shock, and therefore mostly used for kitchenware or laboratory purposes. In construction, soda lime silicate glass is used in the majority of cases.

		Soda lime silica glass	Borosilicate glass
Silica sand	SiO_2	69–74%	70–87%
Lime (calcium oxide)	CaO	5–14%	–
Soda	Na_2O	10–16%	0–8%
Boron-oxide	B_2O_3	–	7–15%
Potassium oxide	K_2O	–	0–8%
Magnesia	MgO	0–6%	–
Alumina	Al_2O_3	0–3%	0–8%
Others		0–5%	0–8%

Figure 3.1: Composition of soda lime silica glass and borosilicate glass, Haldimann et al., 2008

3.1.2. STRUCTURE

Glass has an amorphous structure, instead of a crystalline structure. For the production, all the ingredients listed in the section above are mixed together and heated to a temperature of 1600 C°, forming a liquid. This liquid is then cooled under controlled conditions, fast enough to ensure it transforms into a glass state instead of a crystalline state. This will result in the final amorphous structure, seen as the pyramid in Figure 3.2(a) below (P. C. Louter, 2011). Glass itself has the structure of a liquid, but behaves as a solid material. It is therefore sometimes referred to as a super-cooled liquid (Haldimann et al., 2008). This is different from for example metals, which form a crystalline structure when cooled down. This difference is clearly shown in Figure 3.2(b).

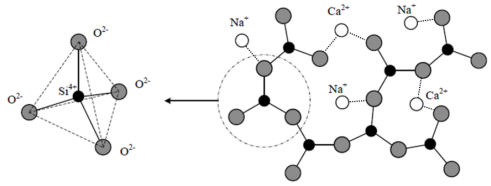

(a)

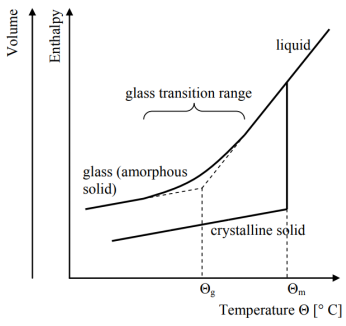

(b)

Figure 3.2: Cooling stages of glass (a) and the structure of soda-lime silica glass (b), (P. C. Louter, 2011)

3.1.3. PROPERTIES

A summary of important material properties of glass is given in Figure 3.3.

Property	Symbol	Unit	Soda-lime-silica glass	Borosilicate glass
Density	ρ	kg/m^3	2500	2200-2500
Hardness	$HK_{0.1/20}$	GPa	6	4.5-6
Modulus of elasticity	E	GPa	70	60-70
Poisson's ratio	n	-	0.2	0.2
Thermal expansion coefficient	α	$10^{-6}K^{-1}$	9	Class 1: 3.1-4.0 Class 2: 4.1-5.0 Class 3: 5.1-6.0
Thermal conductivity	λ	W/(mK)	1	1

Figure 3.3: Properties of soda lime silica and borosilicate glass (Schittich, 2007)

One of the most important mechanical properties of glass, is that it is a linear-elastic material and fails in a brittle manner. This means it has no ductility and therefore no warning mechanism, unlike for example steel. The material can either deform elastically or break. This has to do with the non-crystalline structure explained in section 3.1.2, lacking a crystal lattice. This prevents dislocations and therefore bonding between atoms cannot reform easily when broken (Veer, 2007). When it fails, it will fail completely, making safety mechanisms crucial.

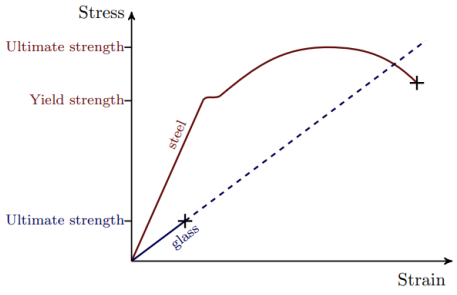

Figure 3.4: Glass and steel comparison. Stress-strain diagram under tension

Because glass is a brittle material, its fracture behaviour is determined by external factors and not by its inherent strength. It is therefore heavily dependent on scratches and impurities originating from production, handling or weather conditions. Additionally, it exhibits linear elastic behaviour. On a macroscopic level, it can therefore be modelled as an isotropic and homogeneous material. Some mechanical properties are inherent to the material, like its elasticity and hardness (Shelby, 2005).
The theory of linear elastic failure mechanics was originally developed using glass samples. Glass therefore has a nearly perfect stress-strain behaviour and thus elastic modulus (Musgraves et al., 2019). This is defined by the following expression:

$$\sigma = E \cdot \epsilon \tag{3.1}$$

Where σ is the stress, E the elastic modulus and ϵ the ratio of the strain. In practice, this means that when a stress is applied, the ratio of strain is multiplied by a constant. For Soda-lime-silica glass, which is the main glass used in architecture, this E-modulus is 70000-73000 N/mm^2 (Musgraves et al., 2019).
Another important factor is Poisson's ratio ν. When a material is elongated in a certain direction, the material will contract in the other directions. This ratio between transverse and axial strain is defined by ν and is 0.2 for glass. With these two constants known, the shear modulus G can be determined with the following formula:

$$G = \frac{E}{2(1+\nu)} \tag{3.2}$$

Stress concentration factor
An important factor for reducing stresses is taking into account the stress concentration factor K_t. It is a dimensionless factor, which is used to signify the difference between the regular stresses and additional stress concentrations. These usually occur around holes or sharp edges in a material, which discontinue regular stress flow, shown in Figure 3.5. It works with the following formula, (Edge, 2000):

$$\sigma_{max} = K_t \sigma_{ave} \tag{3.3}$$

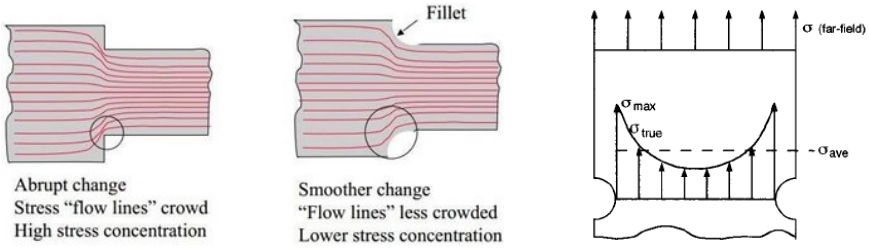

Figure 3.5: Influence stress concentration factor, (Calì, 2020)

3.1.4. FRACTURE BEHAVIOUR

In stress mechanics, three crack opening modes can be distinguished. For brittle materials, mode I from Figure 3.6 is the governing one. The cracks in question are already present in the glass on a micro scale due to production, handling and cleaning. When a tensile stress is applied to the material, these cracks will open further and can develop into a critical crack of significant size, causing the element to fail.

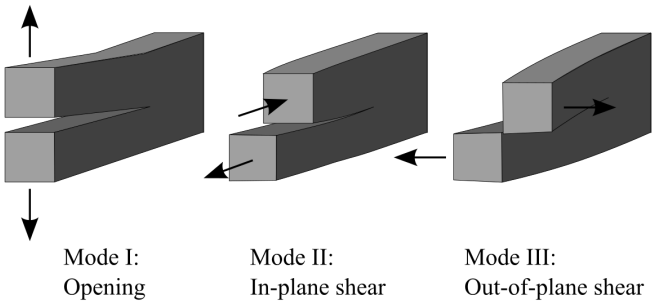

Figure 3.6: Fracture modes

Because these micro cracks and flaws cannot be determined effectively for every separate element, glass elements are evaluated using statistical methods instead. Most common is a two-parameter Weibull distribution and using a 5% quantile. In this model, the failure probability is related to the size of the stressed area. The larger the area, the larger the chance that a flaw is present in the material in this area. Therefore, larger stressed zones statistically fail at a lower strength. This results in the characteristic bending strengths as described in the Eurocodes. For annealed glass this is 45 N/mm^2 and for heat strengthened glass it is 70 N/mm^2 (Musgraves et al., 2019).
The strength of the glass is also dependent on the flaw size present in the material. This relationship is shown in Figure 3.7. This illustrates that the crack depth is of significant influence on the inherent strength of the glass. This decrease in strength can be avoided difficulty, because scratches and flaws will always be present.
Because the probability of the failure of the glass cannot be predicted accurately enough, especially for long term effects, laminated safety glass is almost always required. This will be further discussed in section 3.1.5.

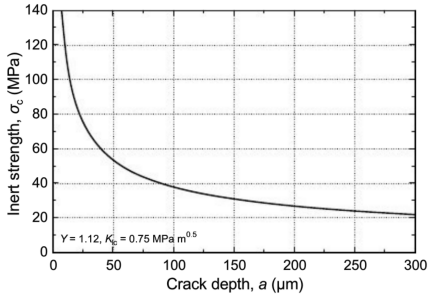

Figure 3.7: Glass tensile strength as a function of the crack depth, Haldimann et al., 2008

FRACTOGRAPHY

Although the present surface flaws are mostly impossible to see with the naked eye, the origin of failure is quite simple to detect post-breakage. Around the critical failure, a

very typical pattern is observed, which can be seen in Figure 3.8. This pattern is called the mirror, mist and hackle. After crack propagation, first a smooth surface emerges, called the fracture mirror. Then a smaller band with a slightly rougher surface forms, called the mist. This is still the stable part of the fracture. Then the unstable part of the fracture starts, where a chaotic and rough surface is created. This last part is called the hackle.

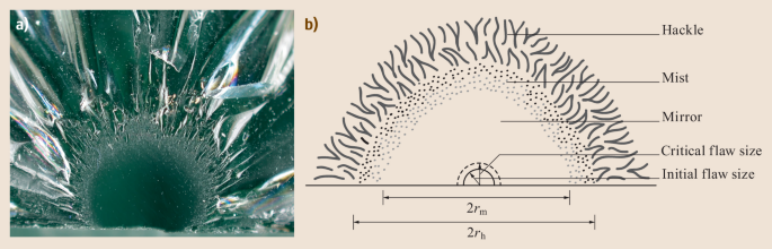

Figure 3.8: Picture (a) and schematic representation (b) of mirror, mist and hackle, (Musgraves et al., 2019)

Another surface pattern typical to glass are the Wallner lines. These lines can be used to predict not just the crack's direction but also to estimate its speed. They develop anytime a flaw or imperfection is reached by the crack front, and the ensuing elastic wave, which is moving faster than the crack front, eventually passes the crack front.

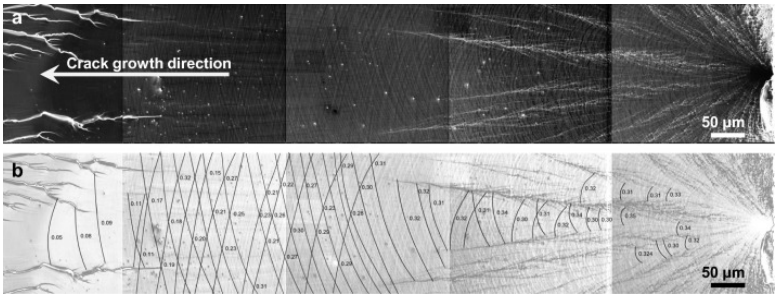

Figure 3.9: Wallner lines, (Narayan et al., 2014)

3.1.5. GLASS PROCESSING

PRODUCTION OF GLASS

The production method we currently use for the production of glass is called the float process, and was developed by Pilkington in 1959. It is a continuous industrial production method, which produces a smooth glass pane with a high level of transparency. The schematization of this process can be seen in Figure 3.10. In the first part, the raw materials are melted together to form melted glass. Also, a certain amount of recycled glass is added, to reduce the melting temperature. This results in a decreased energy demand. In the second section, the mixture is poured onto a bath of molten tin. This material is denser than the glass, and therefore causes the glass to float on top of it. Rollers present

in this bath move the glass over the surface. The thickness of the glass can be regulated by adapting the speed of these rollers. In the last compartment, the glass is slowly cooled, to prevent any residual stresses in the glass. The glass ribbon is then cut to the desired size. Remaining glass pieces are ground and reenter the process from the start. The typical width of the glass is 3.21 m. The maximum standard length is 6 m. This sizing is partially determined by the maximum size of a transportation truck.

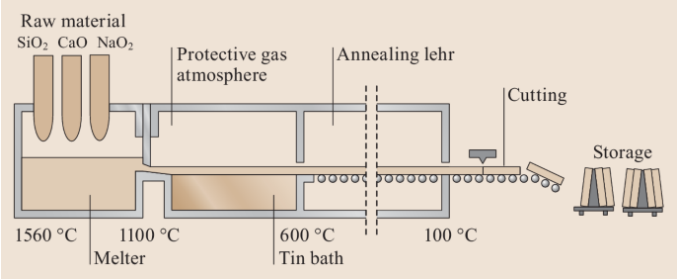

Figure 3.10: Schematization of float glass production, (Musgraves et al., 2019)

CUTTING AND EDGING

After finishing the glass in the float line, the material can be further finished. The most common types of edge finishing types are shown in Figure 3.11. As can be seen in a and b from Figure 3.12, there are a lot of defects in the edge of the glass. For quite some applications a more smooth surface is necessary. For example, because the glass is more susceptible to fatal damage due to local weakening and is also more dangerous to handle. It can also be for optical reasons. When grinding or polishing the edges, the edge quality of the glass can be restored. In this process, the edges of the glass get an additional angle, preventing peak stresses at the corners. These edges are visible in d and e from Figure 3.12.

Edge finishing	Characteristics	Sketch
As cut	Sharp edges	
Arrissed/seamed/chamfered	Sharp edges removed by small 45° chamfer	
Ground (with blank spots)	Flat edge finish with milky appearance including local shiny spots and 45° chamfer	
Ground (no blank spots)	Flat edge finish with milky appearance and 45° chamfer	
Polished	Flat edge finish with brilliant appearance and 45° chamfer	

Figure 3.11: Edge finishing types, (Musgraves et al., 2019)

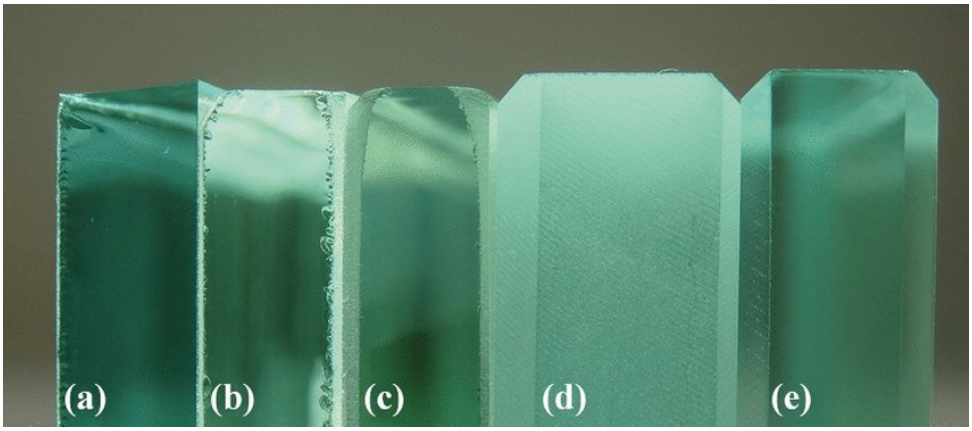

Figure 3.12: Edge finishing types, **a** cut (KG), **b**,**c** seamed (KGS) by different manufacturers, **d** ground (KGN), **e** polished (KPO) (Müller-Braun et al., 2020)

CNC METHODS

Cutting glass can also be done with a Computerized Numerical Control (CNC) machine. Meaning that the movements of the machine are pre-programmed and controlled by software. This allows for complex geometries like these designs to be accurately manufactured, which would be impossible by hand.
In the case of milling, a metal pin seen in Figure 3.13(a), which looks a bit like a drill, will go through the glass along the predefined movements. In essence, it functions like a basic jigsaw. Like with a jigsaw, the blade has a thickness. This has 2 implications. Firstly, the blade cannot make a sharp turn, because it might cause the glass to break. Secondly, the blade is quite thick (6-20 mm) having to take into account quite some loss of material (Diamut, n.d.).

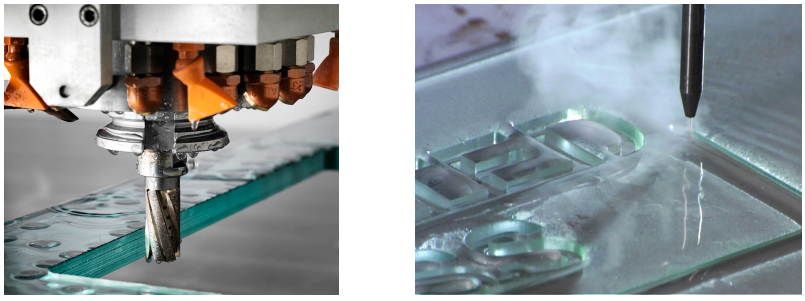

(a) (b)

Figure 3.13: Detail of the milling machine (a) (Diamut, n.d.) and waterjet (b) (PWJ, 2015)

A second method of cutting glass using CNC is by using a waterjet. Its name already implies its functioning: a mix of water and sand is aimed at the glass through a small nozzle,

seen in Figure 3.13(b), with jet speed. A great advantage of the waterjet is that the width of the cut is less than 1 mm (Christian, 2022). This allows for more freedom of shape and for the designs to be cut from one single glass pane. Because the edge quality of a waterjet sample is much better, polishing is sometimes no longer required. However, the edge will keep a non-transparent look at the edges, as can be seen in Figure 7.9(a). Comparing the polished edge to the waterjet, the quality of the polished edge will be of higher quality. Sanders et al., 2021, compare holes with a polished edge to holes manufactured by a waterjet. The maximum principal tensile stresses at the edge of the waterjet hole are 13% higher compared to core drilled holes at equal loads.
Next to the decreased edge quality, another disadvantage of the waterjet is the kerf angle. In Figure 3.14(a) one can see how the cutting pane of a waterjet sample will not often be perfectly straight. This kerf angle, and therefore alignment of the glass edge is dependent on the speed that the waterjet moves through the material, as shown in Figure 3.14(b). This speed needs to be calibrated for every type of material.

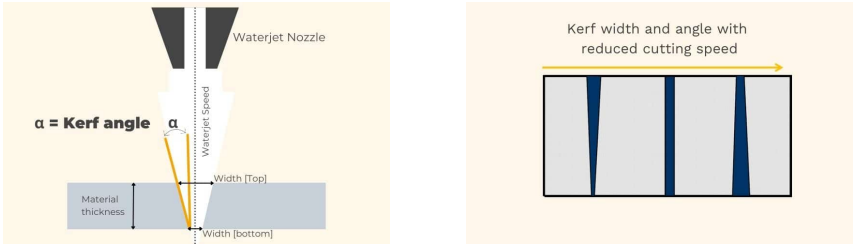

(a) (b)

Figure 3.14: Illustration explaining the kerf angle (a) and the influence of speed on the kerf (b), (Christian, 2022)

PRESTRESSING

Common float glass as described in section 3.1.5 is slowly cooled to prevent any residual stresses and is therefore referred to as annealed glass. In some cases, it is desired to use stronger glass, which can be achieved by heat-strengthening.
The process of thermally pre-stressing glass is shown in Figure 3.15. It is important to realize this process can only be done after any necessary treatment like cutting or drilling the glass, since pre-stressed glass can no longer be cut. After cleaning the glass, it is heated to 600 C^o, which is above its transition state. The panel is then cooled really fast, which causes the edges to cool quicker than the core of the glass. As the core solidifies, it will slightly contract, resulting in compressive stresses in the edges. However, the core will remain in tension. This significant difference in stresses will result in an almost parabolic stress state. Because the edges are in a permanent state of compression, the panel is able to take up higher tensile stresses.

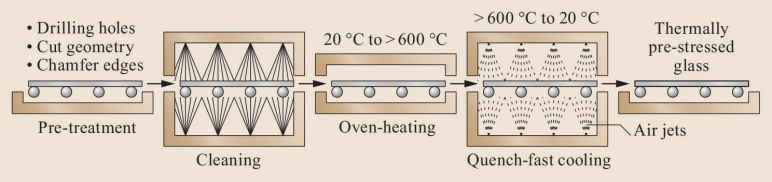

Figure 3.15: Schematization of prestressing glass, (Musgraves et al., 2019)

LAMINATING

Laminated glass consists of multiple glass panes, joined with polymeric sheet material. This is done for two different reasons. First of all, it allows for different thicknesses outside of the standard range of monolithic glass panes. It will also be less heavy than a monolithic pane. It is important however, to take different mechanical behaviour into account. The interlayer will mostly be loaded in shear due to bending of the panel, which will behave viscoelastically. The second reason is to create safety glass. In case one of the glass panes fails, the structure still has some remaining strength due to the other glass panes. The interlayer will also keep the glass shards together, instead of having them fly around. This could cause serious injuries.

Laminating glass is done as a final step, since cutting laminated glass would pose many problems. The procedure is shown in Figure 3.16. So after the glass pane is cut and drilled to the right size, it will be layered with other panes, the interlayers in between them. In the nip-roll process, most of the remaining air between the materials is pressed out. Mild heating ensures some pre-lamination of the panel. Then finally it is placed in an autoclave, where temperature and pressure are carefully controlled to complete the laminating process.

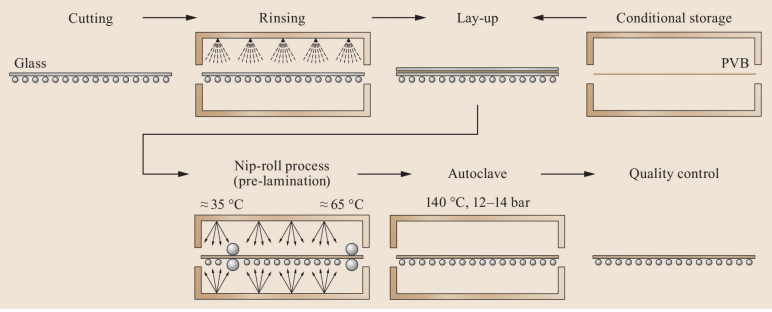

Figure 3.16: Schematization of laminating glass, (Musgraves et al., 2019)

SAFETY GLASS

The behaviour of the safety glass is strongly dependent on the type of glass used. In Figure 3.17 annealed, heat strengthened, and fully tempered glass are compared. With increasing strength due to treatment, the embodied energy also increases. Therefore, when annealed glass breaks, it will break into large sharp shards. Heat strengthened

glass will break into smaller pieces, and fully tempered glass will even break into tiny pieces. The smaller the pieces, the safer the material is for people nearby. However, the residual strength decreases significantly due to the small size of the shards. It is therefore highly dependent on the situation the material is applied in, which option would be the safest.

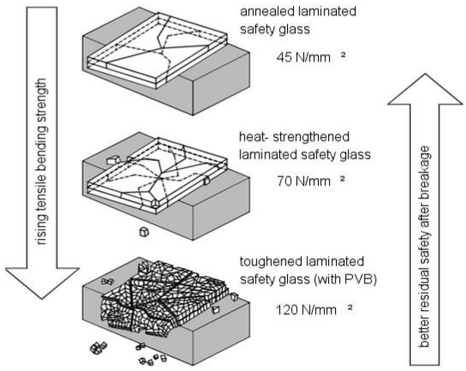

Figure 3.17: Breaking patterns safety glass, taken from (C. Louter, 2022)

3.2. INTERLAYERS

Glass is a very stiff material and unable to deform plastically. Because unevenness on the surface is inevitable, these will lead to peak stresses if loaded in direct contact. This will cause the glass to fail due to crack propagation, at a relatively low strength (Oikonomopoulou et al., 2019). Experiments conducted by Oikonomopoulou et al., 2015 showed that glass elements loaded in compression with direct contact failed at approximately 20% of the strength compared to elements loaded with an intermediary. The interface material should even out the imperfections and ensure a proper redistribution of the stresses. Therefore the interlayer should not be too thin or too stiff. The ideal function of the interlayer is illustrated in Figure 3.18. If the interlayer is too thin, the uneven edges will still touch and lead to peak stresses. If the interlayer is too stiff, the unevenness cannot penetrate the interlayer, causing all the stresses to pass through this point (Aurik, 2017).

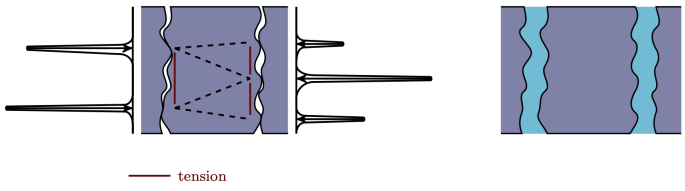

Figure 3.18: Peak stresses in glass due to unevenness and a perfect interlayer redistributing the stresses, (Aurik, 2017)

3.2.1. PREVIOUSLY USED MATERIALS

In previous research, a large variety of interlayers for glass has been used, depending on the selection criteria. For example a thermoplastic layer (Aiello et al., 2011), PU, PVC (Aurik, 2017), aluminium, lead (Oikonomopoulou et al., 2017), Vivak (Akerboom, 2016) wood and POM. Dimas et al., 2022 divide the often used selection criteria into primary and secondary criteria. The primary ones consider thickness, stiffness, compressive strength, creep resistance and tear strength. The secondary ones consider demountability, transparency, thermal expansion coefficient and durability against water and UV. The criteria recommended are shown in Table 3.1.

Primary criteria	Secondary criteria
Ability to be shaped in desired geometry and shape ($d \leq 3$ mm)	Enable Circularity
Slightly less stiff than glass (E <50 GPa)	Optical quality (enhance transparency)
Compressive strength ≥ 1 MPa	Compatible thermal expansion coefficient to glass
Satisfactory creep resistance	Durability: Water, Fire & UV
Tear strength≥ 34 N/mm	

Table 3.1: Overview of design criteria suggested by Dimas et al., 2022

3.2.2. CRITERIA

Each of the primary criteria suggested will be analyzed and adapted to the needs of this study.

DESIRED GEOMETRY

The chosen material will have to fit between the glass panes of the designs. In this situation, there is no need for any double curvature. Since the elements will interlock, there might be a desire for quite a small curvature. This means the thickness should be limited. In research performed by Aurik, 2017 interlayers of thicknesses between 1-4 mm were used. Oikonomopoulou et al., 2019 and Yost et al., 2022 both applied interlayers of 3 mm. Other research also uses interlayers within this range. Therefore 3 mm is chosen as a suitable thickness for the interlayer in this research.

STIFFNESS

A suitable stiffness is necessary to result in the desired distribution of peak stresses described in 3.2. The stiffness of a material can be described either using the Young's modulus or its Shore hardness. The difference is that hardness also shows size dependence in the material (Oikonomopoulou et al., 2019). Various theories exist about the suitable stiffness of the interlayer for glass. Dimas et al., 2022 state that the interlayer should be more ductile than the brittle material it is placed in between. When a material is too stiff however, creep is expected to occur and the overall stiffness of the structure strongly decreases. Therefore for the interlayer, it is recommended to have a lower, but comparable stiffness to the glass it is placed in between. Wurm, 2007 described the ideal stiffness similarly: "The load transfer layer should combine a low modulus of Elasticity similar to that of glass with good durability and as high a compressive strength as possible."

Aurik, 2017 uses a very different approach to find the suitable stiffness of an interlayer

between glass bricks. The compressive stress that caused the dry assembled bricks to fail was around 20-30 MPa during experiments performed by Oikonomopoulou et al., 2015. Therefore 20 MPa is taken as the value where the bricks and interlayer had to be in full contact over the full surface of the bricks. Taking the thickness of an irregularity on one contact surface as Δ, the following formulas are established:

$$\sigma_{contact} = E_{int} \cdot \frac{2\Delta}{t_{int}} \tag{3.4}$$

$$\frac{E_{int}}{t_{int}} \leq \frac{20}{2\Delta} \tag{3.5}$$

For the cast bricks a maximum surface deviation is determined to be $\Delta = 0.25$ mm. For a thickness of 3 mm, it would follow that the maximum stiffness is 120 MPa.

Oikonomopoulou et al., 2019 use shore hardness to describe the suitable stiffness for an interlayer. An estimate of a shore hardness between 60A and 80A is stated. Materials below these values would creep and higher values would prevent even distribution of stresses over the glass surface.

COMPRESSIVE STRENGTH

The compressive strength is relevant, because the material will likely start yielding and display very different behaviour than the original material. It will stiffen and permanently deform, after which it can no longer be expected to evenly transfer stresses over the surface. Dimas et al., 2022 describe a minimum of 2 MPa due to the self weight of the glass bricks. In Aurik, 2017 it is stated that the compressive strength of the whole glass structure is determined by the compressive strength of the interlayer. The required compressive strength is based on the specific loads occurring in the design. In the case of the glass brick arch, a strength $\geq$ 25 MPa was required. Oikonomopoulou et al., 2019 assume the elements should be in full contact at 20 MPa to prevent early failure of the assembly, as derived from the experiments by Oikonomopoulou et al., 2015. The minimal compressive strength should therefore also be 20 MPa.

CREEP RESISTANCE

Many plastics possess time-dependent behaviour at room temperature. Meaning that over time they could permanently deform when applying a prolonged application of forces. This will influence the distribution of stresses. Therefore, creep should be limited for long term applications. Meaning the material should retain sufficient strength over the lifespan of the structure. Aurik, 2017, showed that the thickness also strongly influences creep behaviour. From experiments, it was determined that the strength of PVC decreases strongly over time. Only sheets with a thickness of 1 mm and 2 mm proved to remain strong enough to ensure stability of the brick structure over a lifespan of 5 years. PU70 and PU90 showed a minimal decrease over the same time period. Similar results were shown by Oikonomopoulou, 2019.

TEAR STRENGTH

The tear strength of viscoelastic materials is defined as the maximum force required to tear a test specimen in a direction normal to the direction of the stress (Ciullo and Hewitt, 1999). In Dimas et al., 2022 this value was set to 34 MPa.

3.2.3. FRICTION COEFFICIENTS

When sliding a material over another surface with a certain force, this material is resisted with a resulting frictional force, often denotes with F. At the same time there is a normal force pressing the surfaces together, often denoted as N. The ratio between these two is the coefficient of friction, denoted as μ. The relationship is described as follows (Brittanica, 2020):

$$\mu = \frac{F}{N} \tag{3.6}$$

This value varies between for example 0.07 for PET on steel (Quaglini and Dubini, 2011) and up to 2.0 for rubber against glass (Tuononen, 2016). Most polymers have coefficients of friction in the range 0.2 to 0.6 (Zeus, 2005). An overview of the friction coefficients of some polymers on steel is given in Figure 3.19.

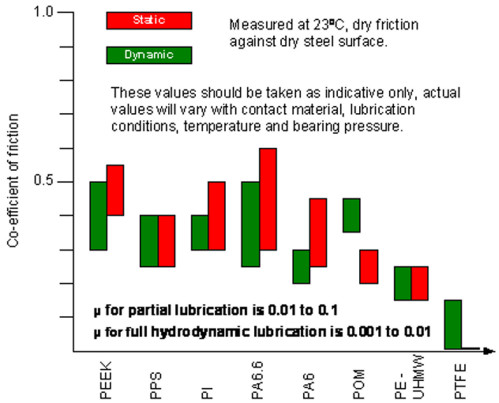

Figure 3.19: Friction coefficient polymers, (Zeus, 2005)

This value is relevant in the Sashimono joint, since it will also influence force transfer between the glass and interface material. This data will mostly be used for finite element modelling further in this research. Because exact data of selected polymers on the edge of glass is not available, an educated guess based on similar materials will have to be made.

3.2.4. MATERIAL SELECTION

Based on the existing criteria a selection of possible interlayer materials was made to apply in the Sashimono joint, which is shown in Table 3.2. For this research also the pricing, availability and manageability of the material have to be taken into account for the execution of the experiments. Secondary criteria like transparency and durability are listed, but not considered substantial.

Property	Value
Geometry	t = 3 mm, possibility for small curvature
Stiffness	$E \approx$ 70 GPa/ max 120 MPa/60A-80A shore
Compressive strength	20-25 MPa
Creep resistance	Sufficient
Tear strength	34 MPa

Table 3.2: Chosen criteria for Sashimono interlayer

Based on previous research and availability a selection of materials will be discussed, namely: Surlyn, PVC, PA6, POM and PU85.

SURLYN

In the research by Yost et al., 2022, Surlyn showed some very promising testing results being applied as an interlayer between glass. Additionally, the material is quite transparent at lower thicknesses, making it a very suitable interlayer material. However, in practise, the material turned out to be relatively high in price, but mostly very hard to ship to the Netherlands.

Property	Value
Geometry	t = 3, 5 & 6.5 mm
Stiffness	E = 100-380 MPa/90-100A
Compressive strength	18-22.8 MPa
Creep resistance	Unknown
Tear strength	113-131 MPa
Transparency	Translucent
Durability	Unknown
Pricing	€€€
Availability	Difficult
Manageability	Unknown

Table 3.3: Properties Surlyn

PVC

PVC is a very conventional material, often used in the construction industry in the form of piping. It has been used in previous research by Aurik, 2017. It is widely available and very cheap. PVC is also very easy to post process, since drilling or cutting the material

can be done with conventional machines. Additionally, it can be ordered in any colour, including a transparent execution.

Property	Value
Geometry	t = 1-50 mm
Stiffness	E = 2200-3100 MPa/77-82D
Compressive strength	37-44 MPa
Creep resistance	Bad, especially if $t \geq 3$ mm
Tear strength	-
Transparency	Transparent options
Durability	Unknown
Pricing	€
Availability	Easy
Manageability	Easy

Table 3.4: Properties PVC

PA6

PA6 is commonly named Nylon. Although it owes most of its fame to the textile industry, it is very commonly used in machines as for example gears. This is mainly due to its excellent gliding properties and wear resistance. The accuracy of the dimensions is also very high. It is often been tested in previous glass research and is a conventional material for the lining of bolt holes in glass. Availability is no problem, nor is the post-processing, the price is a little higher than PA6. The colour of the material can vary, but is most often seen in a milky-white execution, which is not transparent.

Property	Value
Geometry	t = 1-100 mm
Stiffness	E = 940-1200 MPa
Compressive strength	42-46 MPa
Creep resistance	Unkown
Tear strength	-
Transparency	Milky
Durability	Good
Pricing	€
Availability	Easy
Manageability	Easy

Table 3.5: Properties PA6

POM

POM is considered a high strength material which is famous for its hardness. It is therefore often used in industrial machines as a replacement for metals. However, it is not very wear-resistant and the sizing is also not very accurate. It is often used in research like Ebert and Weller, 2014, but not considering complex geometry. Due to its hardness, it is less easy to drill and cut the material, but with extra attention, it should be possible

with conventional machinery. It is widely available, but relatively expensive. The colour of the material is mostly black or white, non-transparent.

Property	Value
Geometry	t = 1-100 mm
Stiffness	E = 2800-3600 MPa
Compressive strength	110-120 MPa
Creep resistance	Unkown
Tear strength	-
Transparency	Nontransparent
Durability	Bad
Pricing	€€
Availability	Easy
Manageability	Difficult

Table 3.6: Properties POM

PU85

Polyurethane is found in both soft and hard executions, serving a wide range of purposes. These vary from insulation material, paint coatings or as a damper. It has been used in various research about structural glass, most famously in combination with cast glass bricks by Oikonomopoulou et al., 2019. This shows the large flexibility of the material to be formed into complex geometry, which has not been shown with the materials listed above. Availability and pricing are comparably reasonable, post processing is more complex since it cannot easily be sawed or drilled due to its flexibility. The colour is mostly amber or white, with a milky to translucent appearance.

Property	Value
Geometry	Easily shapable
Stiffness	E = 20-21 MPa/80-90A
Compressive strength	38-47 MPa
Creep resistance	Sufficient
Tear strength	78-95 MPa
Transparency	Translucent
Durability	Unknown
Pricing	€
Availability	Medium
Manageability	Medium

Table 3.7: Properties PU

3.3. CONCLUSIONS

In construction, soda lime silicate glass is used in the majority of cases, of which the ingredients are listed in Figure 3.1. For the production, all the ingredients are mixed together and heated to a temperature of 1600 C°, after which it is cooled under controlled

conditions. This ensures an amorphous structure, instead of a crystalline structure.

Glass is a linear-elastic material and fails in a brittle manner. This behaviour is not dependent on the material its inherent strength, but on external factors such as scratches on the surface. These micro cracks open up under tension and can develop into a larger crack of critical size. Since peak stresses are very determining in the strength of glass, the stress concentration factor should be limited as much as possible. All edges from the designs should therefore be rounded off. To determine a design strength, statistical methods are used. The origin of failure is quite simple to detect. Around the critical failure a very typical pattern is observed, called the mirror, mist and hackle.

For the design, this means peak stresses should be prevented to limit the probability of a critical flaw being present in that area. Because of the brittle failure, a safety mechanism should be designed for the Sashimono joint, to prevent total collapse of the portal frame. The origin of failure in the experiments can be determined by looking for the typical fracture behaviour of glass.

Float glass panels are produced in a float line, after which they are often further processed for structural, safety or optical reasons. Glass can also be cut using CNC methods, like milling and waterjetting. Both methods allow for a large freedom of form, each with its advantages and disadvantages. To enable a higher design strength, glass is sometimes prestressed. Glass can also be laminated for variation of thickness and to create safety glass. Safety glass has a different fracture pattern than annealed glass.

The choice of production method will also influence the design options and vice versa. Ensuring good edge quality will also improve the strength of the joint as a whole, since it decreases the chance of a critical flaw in the edge.

When joining glass panes, an interlayer is required to prevent peak stresses in the glass. This interlayer should have a sufficient thickness and should not be too stiff. Promising interlayers based on earlier research are Surlyn, PVC, PA6, POM and PU. For this research, these interlayers are examined. The selection criteria are, availability in a thickness of 3 mm, the ability to shape the material into the desired geometry, stiffness of 70 GPa or max 120 MPa, compressive strength of 20-25 MPa, sufficient creep resistance and a tear strength of minimum 34 MPa. Additionally, transparency, durability, pricing, availability and manageability are considered. Because this interlayer its primary purpose is to be able to perform the experiments in this research, the mechanical properties are considered most important. Due to pricing and availability PVC, PA6, POM and PU85 were ordered and used in section 7.1.

A theory for the optimal interlayer stiffness is determined as being a little lower than that of glass, so 70 GPa. In another theory, it is defined based on the maximum thickness of occurring impurities. For cast glass, it is determined to be 0.25 mm. It is unsure however what the maximum deviation of the edge of float glass would be, since it is heavily dependent on post-processing techniques. For glass cut by waterjet, perhaps 0.1 mm might

be a more realistic estimate. For polished edges, this might even be as low as 0.05 mm. This would result in maximum stiffnesses of respectively 300 and 600 MPa. From the material selection in this research, PVC and POM would be most suitable based on the first theory. For the second theory, Surlyn and PU might be more suitable interlayers.

For future research, it is suggested to consider more materials, so more materials can be tested. This could also help determine a suitable theory for the optimal stiffness of a float glass interlayer. Once this is determined, more attention can be paid to secondary criteria that mostly apply for practical use, like its transparency.

4

SASHIMONO

Traditionally, in Japan the responsibility for the architecture, engineering, carpentry and joinery rested with one single person. Therefore, the architecture and joinery cannot be considered separately in Japanese traditional architecture (Seike, 1977). It seems as if the Japanese joints were designed for refined appearance by an artistic craftsman. This is however a misconception, since they were simply a solution to building constructions that resist shear, bending and a moment during a period in history in which metals were scarce and suitable adhesives were non-existent. Because the construction is visible, the wood members serve a dual purpose. Firstly, as a structural element and secondly, as a finishing material. The construction therefore has to be durable and strong on one hand, and aesthetically pleasing on the other (Nakahara, 1967).
This is a beautiful analogy with glass structures, where the joinery is of great influence on the architectural design. The Japanese joints have improved over several centuries and have therefore developed into designs of optimal strength and exquisite beauty. Glass connection design is relatively new, and therefore still has a lot of room for improvement.
Traditional Japanese joints do not make use of adhesives or metal bolting. This technique is called Sashimono. This term derives from the traditional practice of using a woodwork ruler called a “monosashi” to carefully measure timber materials. In this technique, the elements are connected using contact pressure, which distributes the stresses evenly over the contact surface. Timber and glass have very different material properties. However, since glass is particularly vulnerable to peak stresses, but strong in compression, this concept of contact pressure could be very suitable for glass as it is for wood. The main objective of this research is to design a rigid connection using contact pressure. The Sashimono tradition is therefore a useful source of inspiration for design alternatives. The subquestion is therefore as follows.

What types of relevant Sashimono joints exist and which would be suitable to execute in glass?

In Japanese joinery, two main types can be determined. Namely, *Tsugite*, which are splicing joints and *Shiguchi*, which are connecting joints in an angle (Seike, 1977). Within these categories, hundreds of different joints exist. The main joints will be discussed using the following structure:

- How does the joint work in timber?
- How do forces work on the joint?
- How could the concept of this joint work in glass?

When discussing the points listed above, it is important to keep some relevant differences between timber and glass in mind:

- When executing a Sashimono joint in timber, tolerances are important, but not critical. If the joint is too tight, it can be sanded and hammered in place. If it is too loose, some sawdust can be added in between the elements to make them fit tighter. For glass joints, this is not a simple option. Forcing the material when it does not fit will cause it to fail. Adding material could be done in the form of extra interface material, but this is very impractical for local differences. Adding mortar or another injectable such as silicones could solve the tolerances, but will have an unknown effect on force transfer.
- The timber sections described in the chapter below consist of solid rectangular sections, making them stable in most directions. However, when executing such a joint in float glass, the section will be significantly more slender. This requires extra attention for out of plane stability.
- Wood is an anisotropic material and glass is an isotropic material. This means the material properties of timber are different, depending on the angle that forces are applied to it. For glass, this is not the case, and the material behaves identically in all directions.

4.1. TSUGITE

Koshikake tsugi, Lap joint

The lap joint (4.4(a)) is one of the most simple joints. Most Japanese joints consist of male and female members. In this case, they are identical. *Koshikake* literally means seat, referring to the lower member. The top member simply 'rests' on the seat member. Due to its plainly cut faces, it is easy to execute and has a large carrying surface. This makes the joint very suitable for heavy construction. Because of its large contact area, it distributes stresses evenly over its surface. This quality is the reason that it is often used in practice in combination with other joints. Unfortunately, due to its simple shape, it is unable to transfer tension forces or shear forces in both directions, as can be seen in Figure 4.1(a). When transferring shear forces, this will result in normal stresses and stresses

due to the eccentricity of the force application, seen in Figure 4.1(b). The joint is also quite unstable out of plane. For this reason, it is sometimes glued, but more often used in combination with other joints, see section 4.1.1 (Seike, 1977).

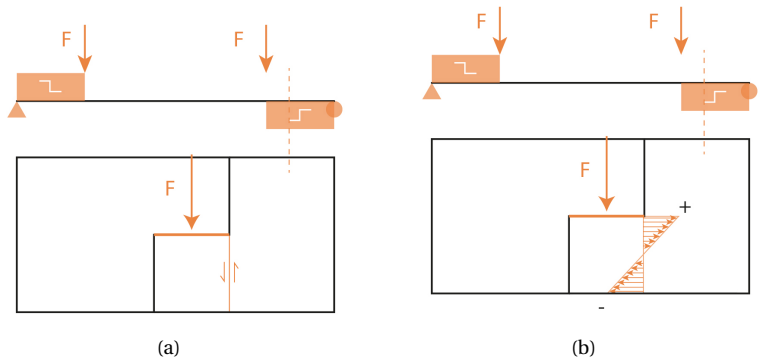

Figure 4.1: Lap joint in shear showing shear surface (a) and resulting stresses in the section (b)

In the case of a laminated glass joint, this principle could be interpreted in two ways. The first option would be to cut all panels to the same dimensions, and orientate the beam elements in the same direction as the timber joint. The force transfer would then also work in a similar way, as seen in Figure 4.1. In the second option, the lap joint could be used to enable some out of plane stability. In this scenario, some of the panels of both the laminated glass beams would be longer than the others. This way the beams could slide into each other. The main force transfer is now oriented in a different direction. A disadvantage is that the beams are locally weakened due to decreased thickness, which decreases the strength of the joint and also poses some problems with structural safety.

Mechigai tsugi, stub tenon joint
The joint consists of a clear male and female part, of which the shape knows many different variants. For example, the number (4.4(b) and 4.4(c)) and size of the "fingers" can vary. The more fingers, the more even normal stresses are distributed. Stresses due to the eccentricity as in Figure 4.3 will increase, because of the reduced "finger height". It is important to establish which of these stresses is more influential to determine whether it is beneficial for the stress distribution of the joint. More fingers also add complexity in terms of production. It is used to strengthen a splicing joint, and is therefore, like the lap joint, mostly used in combination with other joints. It is very suitable for transferring shear forces in both directions as can be seen in Figure 4.2, and will prevent the joint from twisting.

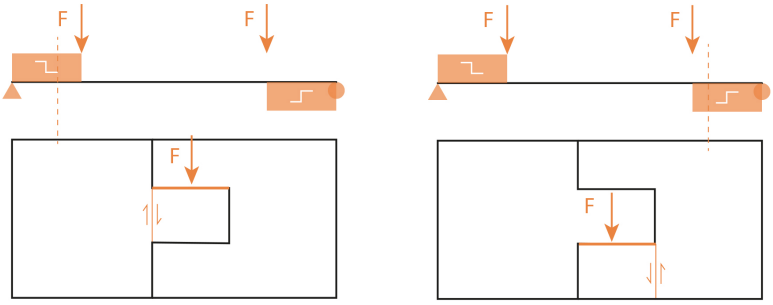

Figure 4.2: Stub tenon joint on left and right side of a beam, showing resulting shear surfaces

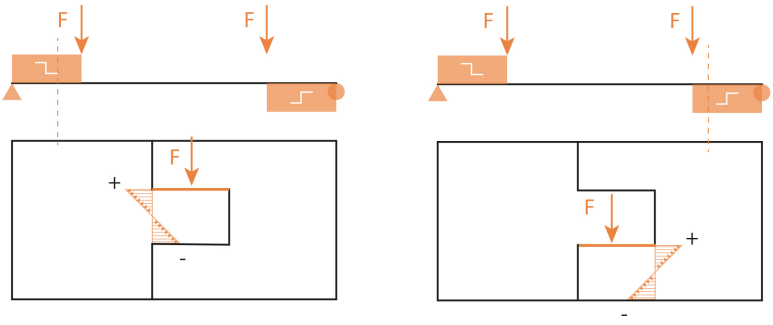

Figure 4.3: Stub tenon joint on left and right side of a beam, showing resulting stresses in the section

A somewhat similar principle is already used when splice laminating glass panels. This does require gluing of the plates. When rotating the orientation, the fingers could also be cut out of laminated glass panes. This could result in a rigid splicing joint, which is often used for glued glass portal frames. Similar as with timber, the optimal shape would depend on the ratio of the influence of the stresses as a result of transferring shear forces.

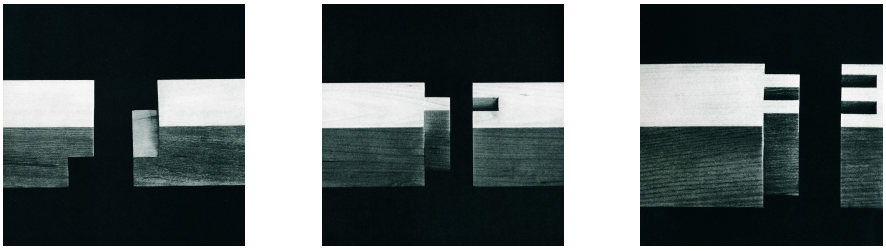

(a) (b) (c)

Figure 4.4: Lap joint (a) and stub tenon joints (b,c), (Seike, 1977)

Ari tsugi, Dovetail joint
Probably one of the more famous joints is the Dovetail joint (4.6(a)). It is the most simple self-locking joint. The Dovetail or pin of the male part of the connection is able to take shear, in the same way as the stub tenon joint in Figure 4.2. The Dovetail can also take up compression and tension. Depending on the angle of the tail, there will also be an resulting vertical force when taking up a tensile force, shown in Figure 4.5. Unfortunately, in basis it is not very strong. Due to its interesting shape it is more often used as a decorative connection instead. For construction purposes, it will have to be combined with another type of joint like the lap to ensure some stiffness. Peak stresses do occur in the slender part of the male piece and in the wide end of the female piece, often resulting in failure as seen in 4.6(b).

When performing tensile tests, the ultimate tensile strength was determined to be 480 kg (Sumiyoshi and Matsui, 1989) (approximately 4.7 kN). In comparison, the tensile strength of a massive block of black pine in the grain direction is 420 kg/cm^2 (approximately 41.1 MPa). The test setup used a block of 105x105 mm, so would fail at 46305 kg instead. This means the Dovetail joint has only 1% of the strength of the wood itself. An important factor to keep in mind is the anisotropic properties of wood. The failure has mainly to do with the resulting reaction force in the direction perpendicular to the tensile force. This causes a force perpendicular to the grain, in which direction the wood only has a strength of 3-5% compared to the longitudinal direction (Ravenshorst, 2021).

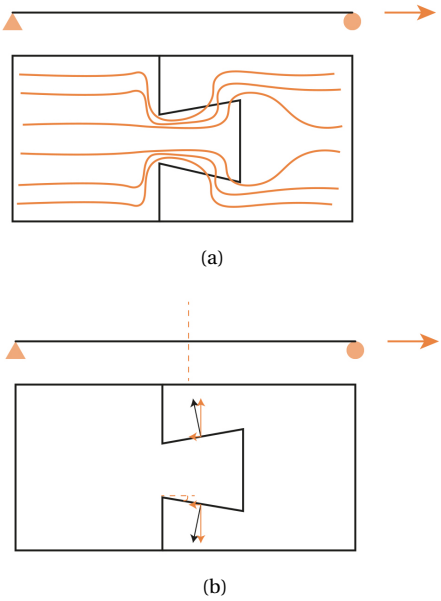

Figure 4.5: Schematization of stress "flow lines" showing concentration at corners Dovetail joint in tension (a) and schematization of influence angle on tensile capacity of Dovetail joint (b)

For a glass Dovetail, it could be used similarly to the *Mechigai* as a rigid splicing joint. Attention to the sharp edges and failure points of the timber tensile tests should be given, since these are expected to give peak stresses in the glass. However, since glass is an isotropic material, the difference between a solid section and the Dovetail joint is not expected to be as big.

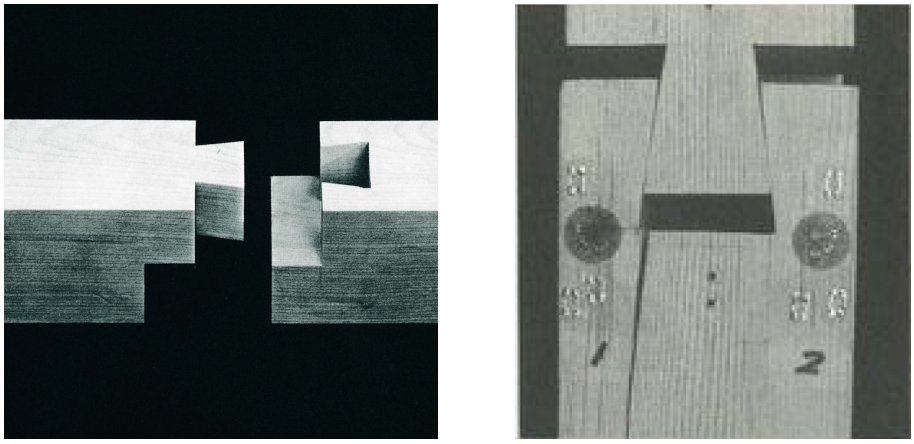

(a) (b)

Figure 4.6: Lapped Dovetail (a) (Seike, 1977) and failure mode (b) (Sumiyoshi and Matsui, 1989)

Kama tsugi, Gooseneck joint

The word *Kama* actually means both Gooseneck and snake head. The latter is the actual origin of the name, since the shape actually resembles a snake head (Seike, 1977). It is especially designed to resist tension forces and often used to join large lumber sections (Sumiyoshi and Matsui, 1989). It seems as if elongating the "neck" would increase the surface and therefore the tensile strength. However, it seems that in timber this is of little influence and it only decreases the effective length of the elements to be joined (Seike, 1977). When taking up pure tension, the force is divided over the two sides of the head, resulting in two shear surfaces, seen in Figure 4.7(b). This results in two normal stress parts and the forces also create stresses due to the eccentricity in the female part, shown in Figure 4.7(c). Because the Gooseneck can take up both tension and compression forces, it can take up a moment too (Figure 4.7(d)) with a decreased section height compared to the rest of the beam.

For the tensile tests, two failure modes developed. Namely, first in bearing, where the Gooseneck crushes the abutment of the female piece, see 4.8(b). Secondly, the head of the male end started shearing in a rib. Ultimate tensile strength is 2400 kg (Sumiyoshi and Matsui, 1989) (approximately 23.5 kN), which is a factor 5 larger than that of the Dovetail joint. Compared to the solid section, this joint has 5% of the strength.

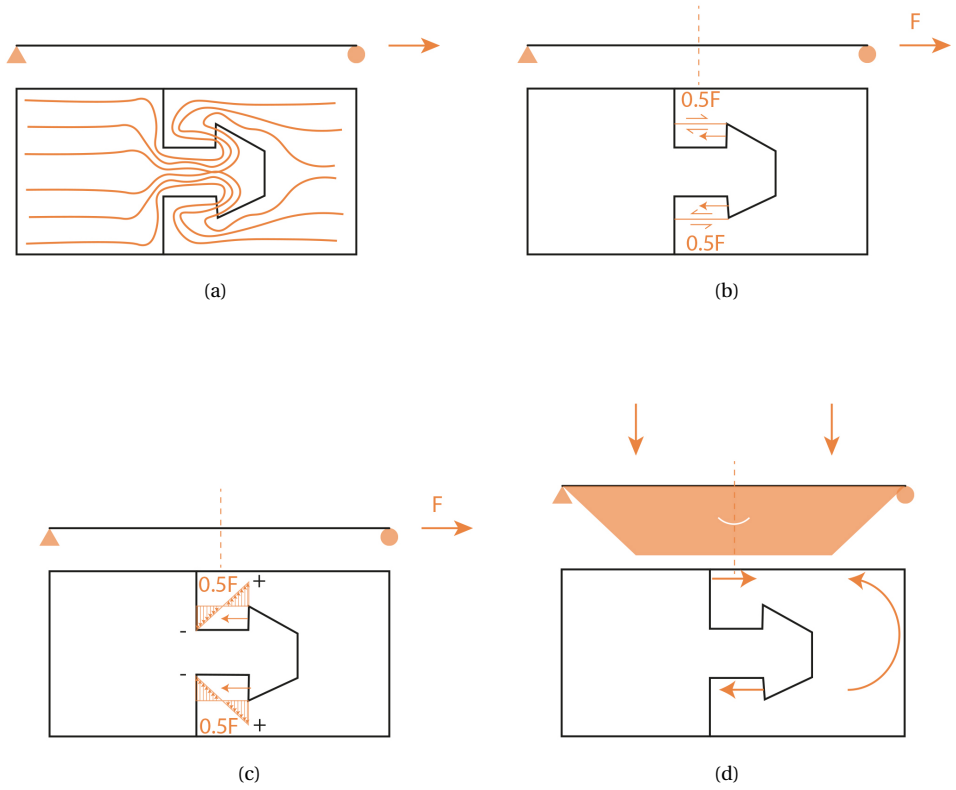

Figure 4.7: Lapped Dovetail and failure mode

If executing such a joint in glass, high compressive normal stresses would occur on the female element of the joint, and in the head. These are not likely to make the sample fail. The stresses due to the eccentricity in Figure 4.7(c) will require more attention, because tensile stresses will occur. Due to the way the forces are transferred in this joint, the stress concentration factor is high, as can be seen in Figure 4.7(a). This could be diminished by rounding the shapes, creating an easier flow.

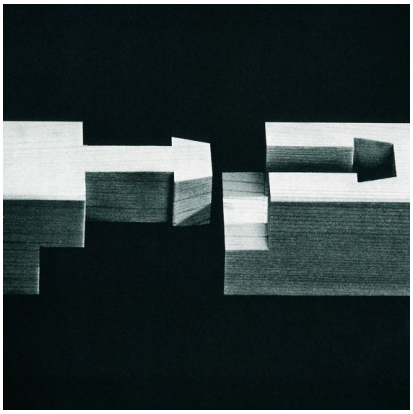

(a)

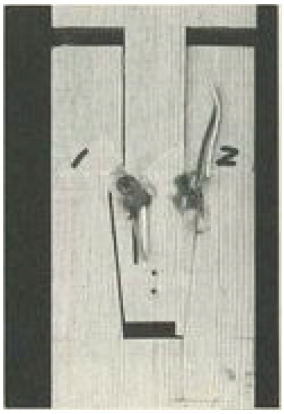

(b)

Figure 4.8: Lapped Gooseneck (a) (Seike, 1977) and failure mode in tension Gooseneck (b), (Sumiyoshi and Matsui, 1989)

Sogi tsugi, Scarf joints
In a scarf joint (4.10) both ends are identical, except being the exact opposite (Nakahara, 1967). The most basic version is actually a butt joint in which the ends are shaved at an angle to increase the contact surface. In traditional timber joints, adaptations of the scarf joint are most commonly used as splicing joints. The joints are often slid into place in quite ingenious ways using a key element. There is some tolerance in the joint, so the elements can be joined and once they are in place, they can be held in place by inserting the key element.

Okkake daisen tsugi and *Kanawa tsugi*
This key element can be either inserted in such a way that it takes up the shear of the sliding elements by penetration of the joint in plane as with the *Okkake daisen tsugi* seen in Figure 4.10(b). Or it can take up the shear by inserting the element out of plane as with the *Kanawa tsugi* seen in 4.10(c).

The *Okkake* joint is less suitable for taking up shear force (see Figure 4.9(a)), because like the lap joint it can only take up shear in one direction. The Kanawa joint (Figure 4.9(b)) is able to take up shear in both direction due to the interlocking system.
Because both joints have a large contact area and make use of interlocking systems, they are very strong in tension. For example, the *Okkake daisen tsugi* 4.10(b) and *Kanawa tsugi* 4.10(c) fail at a force of 4000 kg (Sumiyoshi and Matsui, 1989) (39.2 kN), which comes down to 9% of strength compared to a solid section.
The two joints mentioned above can also take up a moment because of this sliding principle. The interlocking pieces of the Kanawa create a lever arm horizontally, instead of over the height of the beam, see Figure 4.9(d). This increases the height of the lever arm. The *Okkake* joint can also take up a moment, but has quite a small lever arm, seen in Figure 4.9(c).

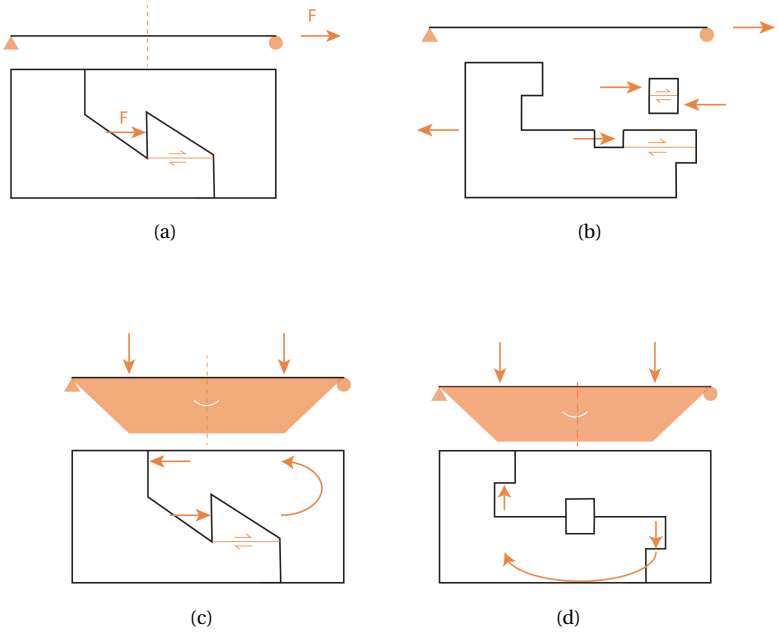

Figure 4.9: Okkake under tension (a), Kanawa under tension (b), Okkake under a bending moment (c) and Kanawa under a bending moment (d)

For glass, this scarf could have some interesting applications as well. The interlocking principle has a large surface area and could provide interesting assembly options. The key could for example be made from a stronger glass type of completely different material. The *Okkake* joint is not very stiff and allows for quite some movement, which makes it less suitable for glass. The *Kanawa* also displays and interesting way of enabling out of plane stability of the laminated glass beam. If one or multiple of the panels is slightly elongated, it could be slotted into the female part of the other beam.

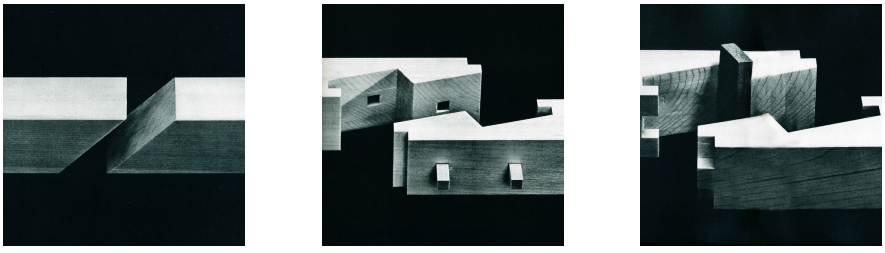

Figure 4.10: Scarf joints: Simple scarf (a), Okkake daisen tsugi (b) and Kanawa tsugi (c), (Seike, 1977)

Chigiri tsugi, Spline joints
In the case of a spline joint, a different material is used to connect two elements. This has several advantages. First of all, if at a certain joint, additional strength is required, a stronger type of timber can be chosen, without having to use stronger (and often more expensive) wood for the whole construction. The weakest link then becomes stronger. Additionally, spline joints can enable easier assembly of the structure. The main and often heavy construction can be put in place, after which only the small spline element has to be placed. Keeping tolerances in mind, this element is much easier to wiggle in place than a whole beam. The shape of the spline joint can vary. Some examples are the *Ari kata* (butterfly spline), *Kine kata* (bow-tie spline) and *Are kata* (dumb-bell spline, seen in Figure 4.11(b)).
For glass, this principle could also apply. For example by using a stronger and more expensive type of glass as a joining element, whilst keeping the global structure of a lower quality (and more sustainable) glass type. Or a softer material, which might limit the peak stresses around it.

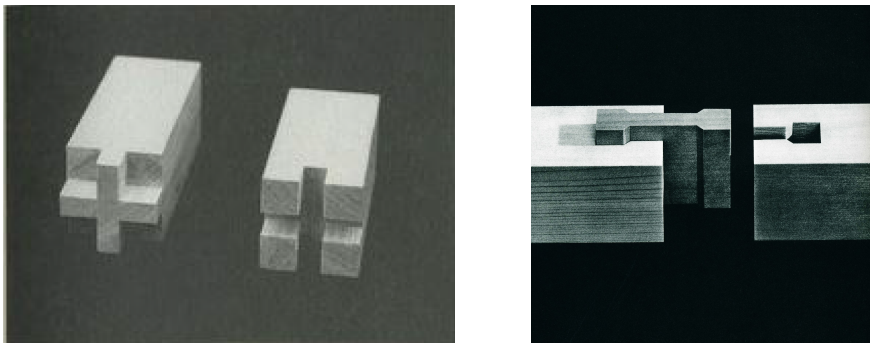

(a) (b)

Figure 4.11: Cross-shaped (a) (Sumiyoshi and Matsui, 1989) and spline joint (b), (Seike, 1977)

4.1.1. COMBINATIONS

Since the *Ari tsugi* and *Kama tsugi* have already been discussed separately and behave quite similar in combination with other joints, they will be discussed interchangeably in de section below.

Koshikake ari/kama tsugi, lapped Dovetail/Gooseneck joint
The lapped Dovetail 4.6 works very much like the regular Dovetail, as for the lapped Gooseneck 4.8. Due to the lap and increased contact surface the joint is more stable as a whole. However, it does not increase the tensile capacity of the Dovetail itself. In laminated glass beams, this principle could be used to create some out of plane stability. Some of the panes would then be elongated, keeping the joint in place, while the Dovetail or Gooseneck enables some moment and shear resistance.

Mechigai ari/kama tsugi, stubbed Dovetail/Gooseneck
Since the Dovetail and Gooseneck provide quite some shear strength, but very limited moment resistance, they are often combined with a stub tenon. This can be done either on just the bottom of the joint 4.12(a), or it can also be done next to the Gooseneck or Dovetail 4.12(b). The latter prevents it from wiggling and can reduce normal stresses due to shear. A disadvantage lies in the production of the joint, since it is quite detailed and therefore sensitive to tolerances.

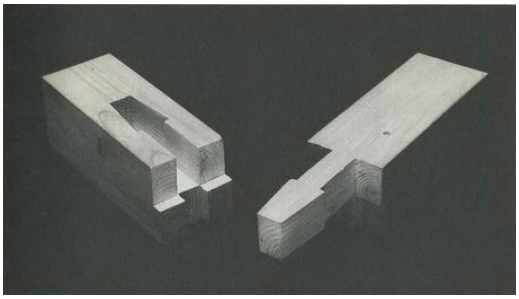

(a)

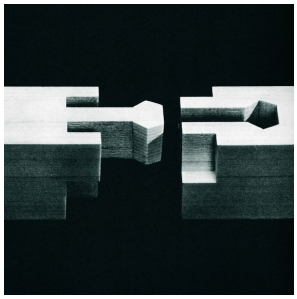

(b)

Figure 4.12: Stubbed Gooseneck (a) (Sumiyoshi and Matsui, 1989) and double stubbed Gooseneck (b), (Seike, 1977)

4.2. SHIGUCHI

Ai jakuri, End lap joint or shiplap

The *ai jakuri* in Figure 4.13(a), can be considered one of the simplest joints and can often be found in ancient structures. Because the halves slide off each other easily, they are currently only used as ground sill joints (Seike, 1977). Unless glued, it does not provide any stiffness. Another disadvantage is that the thickness of each element is halved at the joint, therefore weakening the structure. In glass, this joint could be produced by adjusting the lengths of the panes on half of the present panes on each beam and column. Similar to the timber joint, the weakening of the beams at the joint is disadvantageous. Without adhesives, this connection will not provide sufficient stability and will simply fall off. However, the principle could be used as in the lapped joint, in helping provide some stability out of plane.

Sammai gumi, Open slot mortise

The literal meaning is "three-leaf set", where the flanges on the column form two leaves and the beam the third one. It can be seen in Figure 4.13(b). This joint is quite similar to the shiplap, but then supported in both out of plane directions. It is actually quite a standard adhesive connection in glass. It is not possible to make this joint rigid without the use of adhesives. Since the objective of this research is to create a demountable connection, this joint is less suitable.

Mechigai dome, Stub tenon

This joint is very suitable for transferring shear forces to the column, but is not too strong. It can be seen in Figure 4.13(c). The purpose is to conceal the actual structure of the joint (Seike, 1977). The joint will have some stiffness, but will not be fully rigid due to the shape of the stub tenon. The full width of the beam is able to rest on the column. In the case of glass this ensures safety of the structure. Only the middle pane would then be extended to provide lateral stability. If this pane would fail, the global structure would still remain in place.

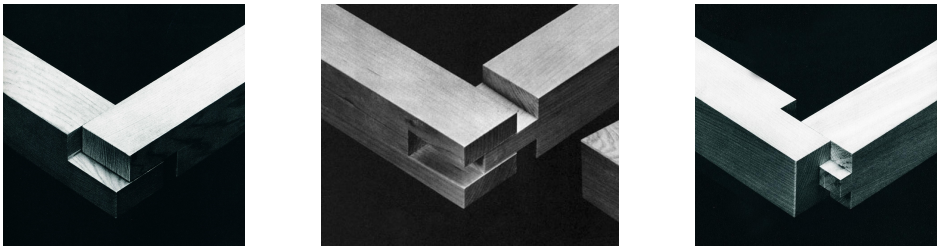

(a) (b) (c)

Figure 4.13: Ai jakuri (a), Sammai gumi (b) and Mechigai dome (c), (Seike, 1977)

Hako dome, Rabeted tenoned miter joint

The origin of this joint is to minimize the effect of shrinkage and the opening of the joint that could follow (Seike, 1977). Due to its diagonal cut, the *hako dome* has an enlarged

contact surface. Because of the finger, seen in Figure 4.14(a), this joint is rigid and can therefore transfer shear and moment forces. Like the mechigai dome, its full section is resting on the column. A great advantage is that the shape of this joint is relatively simple and can therefore be produced without too many production errors. If executing this joint in glass, the finger should most likely be thicker to prevent exceeding tensile stresses and failure.

Ari dome, Housed Dovetail
In this joint, a slot is made of the same height as the height of the beam in the shape of the Dovetail. The beam is then slotted into the column, seen in Figure 4.14(b). The beam can quite easily be hammered into the connection and is thereafter rigid. Less convenient is the fact that the whole load transfer has to happen through a small section of the Dovetail. If this throat fails, the whole joint will fail. The current orientation of the joint is not suitable for laminated glass panels, because of the shape of the Dovetail. If the Dovetail would be rotated 90 degrees, it could provide an interesting joint in glass. In essence, it could be the same as the regular Dovetail (4.6), but then under an angle.

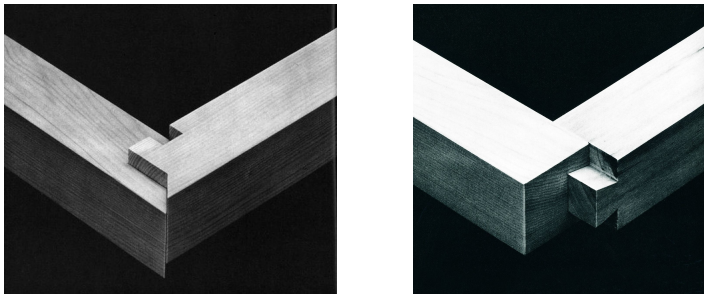

(a) (b)

Figure 4.14: Hako dome (a) and Ari dome (b), (Seike, 1977)

4.3. CONCLUSIONS AND DISCUSSION

The traditional Sashimono joints provide multiple fascinating examples. These are suitable for transferring shear, normal forces and sometimes even bending moments. However, without using any adhesives, quite a small number of the joints could be executed as a rigid joint. Additionally, the shape of float glass also limits quite some possibilities. The Gooseneck and Kanawa joints are able to take up shear forces and a bending moment. They can also be executed in glass without causing very impractical or vulnerable sections. These joints will be modelled in further detail in the following chapters.

In this chapter, the strength of certain joints was compared. However, no documentation about the number of experiments or strength class of the timber used is available. It is therefore not certain that this data is accurate. Unfortunately, no similar data is available and it will therefore not be used as input for further research. It does provide relevant data on the strength of the joins discussed, compared to each other. This shows

for example that the scarf joints are the strongest category discussed.

In the literature available, the majority of the joints is shown with the same type of wood. However, some are shown with different types, to cater for specific properties that enhance the strength of the joint. This principle would be very interesting to apply to a glass joint, because it might strengthen them where the material itself lacks in tensile strength.

II

Design

5

ANALYTICAL MODELLING

In previous chapters, relevant input was generated in order to create clear starting points for a rigid glass Sashimono joint. This will now be used to create the optimal shape of this joint. The approach described will be used to answer the following research question

What is the influence of shape on force transfer and how can this interaction be optimized in a glass Sashimono connection design?

To gain a better understanding of this interaction, some of the wooden Sashimono joints discussed in chapter 4 will be analyzed and optimized. This will be done using a combination of analogue and numerical modelling, eventually resulting in the final designs of this joint.

Both physical models and hand sketches will be used to gain an improved understanding of the behaviour of the selected joints. These are also necessary as a basis for hand calculations, which serve as a validation of the later numerical modelling.

5.1. PHYSICAL MODELS

First, the physical models will be made using foamboard (see Figure 5.1), on which moment forces are applied. The deformation of the models gives good insight in the force transfer of the joint type.

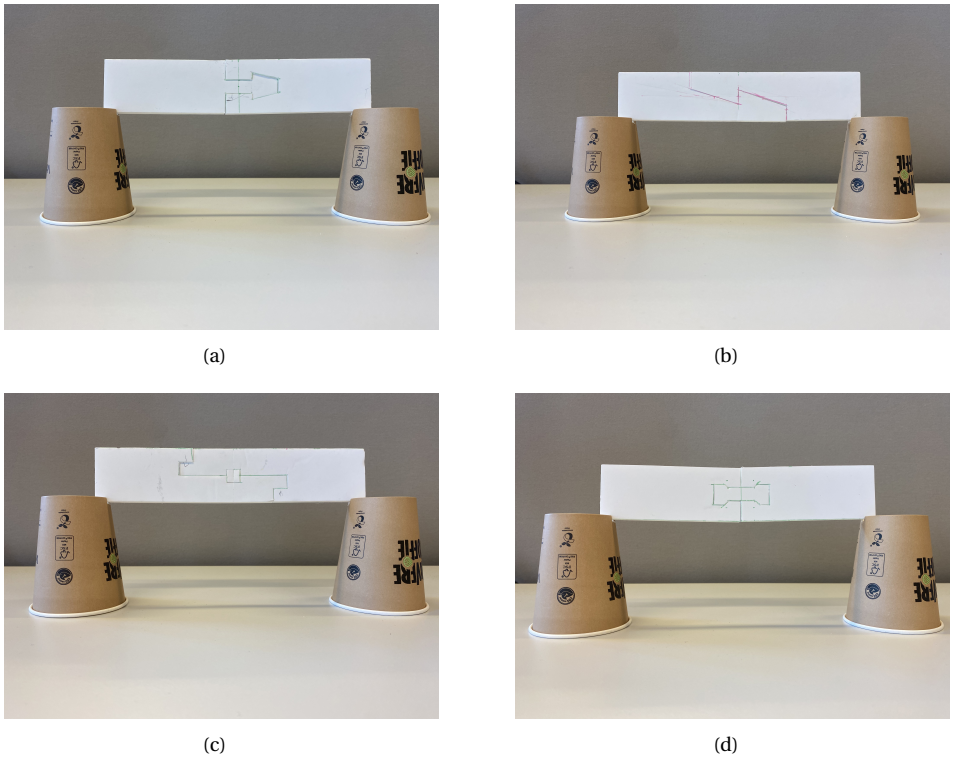

(a) (b)

(c) (d)

Figure 5.1: Gooseneck (a), Okkake (b), Kanawa (c) and Spline (d) models

When applying a moment, the Gooseneck (5.2(a)) turns out to be a surprisingly moment-resistant joint, with limited deformation. This is due to the lever arm between the top of the beam (compression) and the head of the Gooseneck (tension).
The *Okkake* (5.2(b)) joint has trouble taking up the tension forces on the bottom side. It is kept together in compression at the top and in tension in the middle of the beam. Unfortunately, this results in quite a low lever arm and therefore small moment capacity. Additionally, due to the opening up of the joint at the bottom, displacements are large, which can create very undesirable situations.
The third model in Figure 5.2(c) of the *Kanawa* joint is very rigid, and almost behaves as a continuous beam. The main explanation for this could be that the lever arm of the connection is taken at the corners horizontally, instead of the height of the beam. A larger lever arm means the joint can take up a larger moment.
The spline joint (5.2(d)) has a limited deformation, with a lever arm similar to the Gooseneck (5.2(a)). The spline element can have many different shapes, which will influence the rigidity of the joint. Additionally, it would be interesting to test this type of joint with a different material for the spline, either stiffer or more flexible.

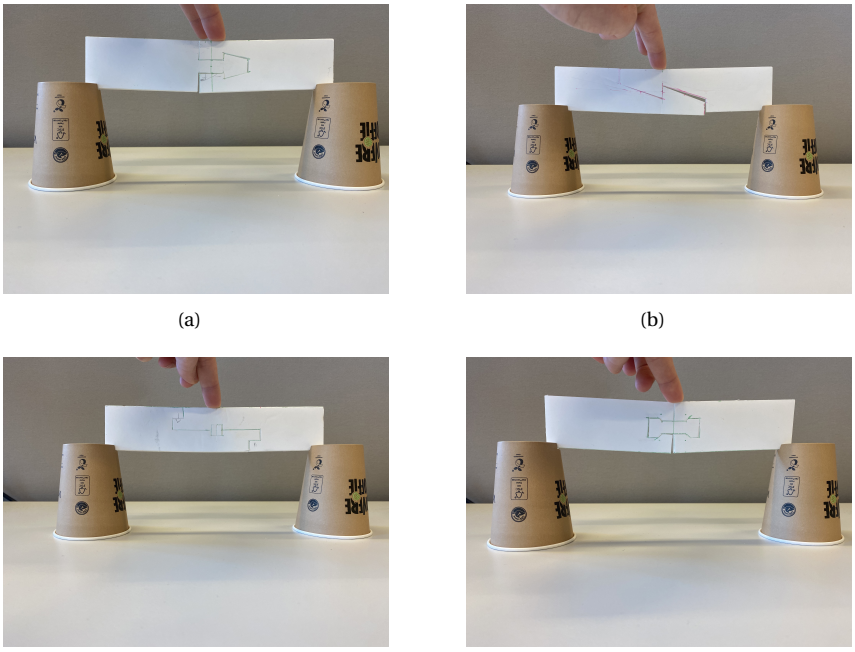

(a) (b)

(c) (d)

Figure 5.2: Gooseneck (a), Okkake (b), Kanawa (c) and Spline (d) models under a moment force

5.2. SKETCHES

5.2.1. GOOSENECK UNDER TENSION

Male element

The models above are then schematized, so an approximation of the forces can be calculated. Take the tension force as F, the tensile stress in zone 1 (L_1 in Figure 5.3) will be

$$\sigma = \frac{F}{A1} \tag{5.1}$$

In the neck in zone 2 (L_2 in Figure 5.3), the force will remain the same, but the height and therefore the area will reduce. This means that the stresses in zone 2 will be higher.

$$\sigma = \frac{F}{A2} \tag{5.2}$$

The tensile force on the left has to be balanced on a global scale. Since the contact area is divided over two surfaces, and the joint is symmetrical in z-direction, each contact area will take up of half of the force F. This means a shear surface will come into being in the head, shown in Figure 5.3. Because the force line of the neck has an eccentricity compared to the force line of the contact surface, two internal moments will develop in the head.

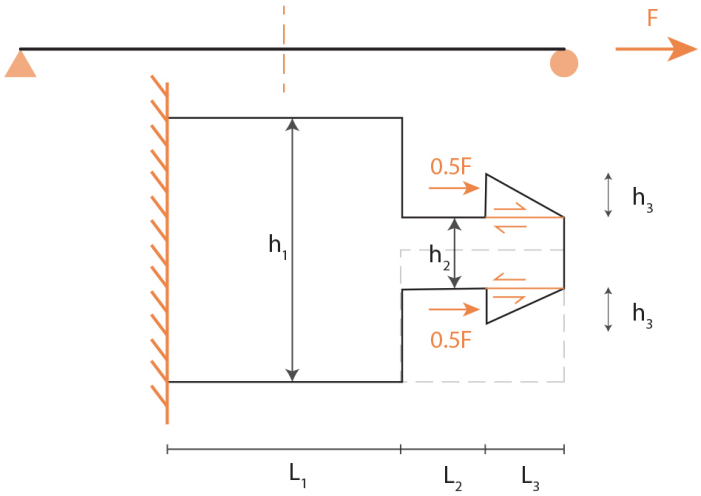

Figure 5.3: Mechanical scheme Gooseneck under tension, male element

Local stresses at the contact area at zone 3 should also be checked. This is done by looking into the bottom part of the head in more detail. This part can be schematized as a clamped beam as seen in Figure 5.4. This beam can be separated into three parts: I, II and III. Each part is subjected to a variation of normal forces, shear forces and a bending moment .

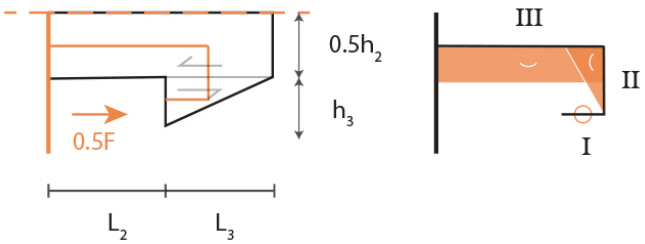

Figure 5.4: Mechanical scheme and moment line Gooseneck under tension, detail male element



Figure 5.5: Resulting normal and shear forces of Gooseneck under tension, detail male element

Stresses due to the normal force can be determined using the following formula:

$$\sigma = \frac{N}{A} \tag{5.3}$$

Stresses due to the shear force can be determined using the following formula:

$$\tau = \frac{V}{bh} \tag{5.4}$$

Stresses due to the bending moment can be calculated with formulas 5.5 and 5.6:

$$\sigma = \frac{M}{W} \tag{5.5}$$

$$W = \frac{1}{6} \cdot b \cdot h^2 \tag{5.6}$$

Female element

The same procedure was followed for the female element. The total tensile force on the right has to be balanced by the joint. The area of contact is at the 'chin' of the Gooseneck. Each part takes up half of the total force, resulting in a shear surface.

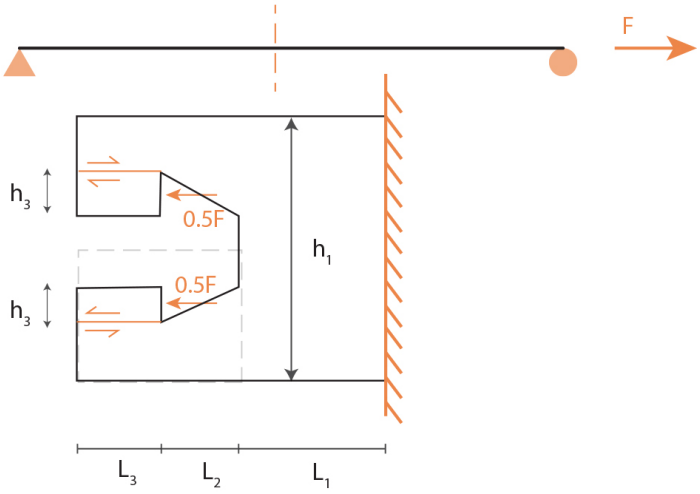

Figure 5.6: Mechanical scheme Gooseneck under tension, female element

To gain a better understanding of the stresses occurring in this joint, a detail is further examined in Figure 5.7. This shows the schematization and bending moments of the joint. Note that the centerline in L_2 would actually run differently, but the objective of this schematization is to determine the forces and stresses in the critical section. In this case, this is the transition between L_3 and L_2. For this section, it is irrelevant whether the

remaining beam is straight or at an angle. Similar to the male element seen in Figure 5.4, this part of the joint can be modelled as a clamped beam. The most important difference is that in the case of the female element, the height and therefore the area of the beam varies across section III. This is relevant for A in Formula 5.3 as well as h in Formula 5.6.

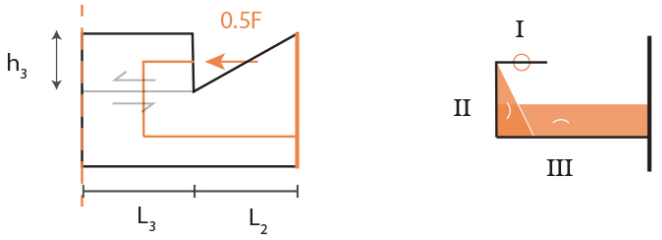

Figure 5.7: Mechanical scheme and moment line Gooseneck under tension, detail female element



Figure 5.8: Normal and shear forces Gooseneck under tension, detail female element

5.2.2. GOOSENECK UNDER BENDING

Male element

Under a positive bending moment, the total height will take up the forces in zone 1. In zone 2 and 3 the bottom chin of the male part will take up the tension in the joint. The compression will be taken up at the top of the total height. This is the maximum lever arm possible in this zone.

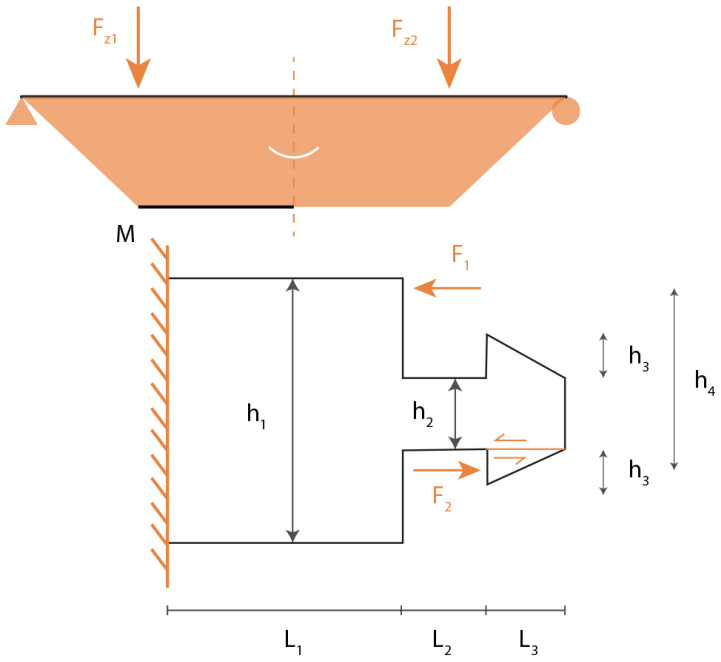

Figure 5.9: Mechanical scheme Gooseneck under a bending moment, male element

Because the element is no longer loaded in pure tension, it is more complicated to determine the forces present. An option is to use a strut and tie model, with varying heights. If we take h_1 as the total height in zone 1 and h_4 as the height of the lever arm in zone 2 and 3, we can use the following formulas. Because there should be a horizontal balance, it is assumed that $F_1 = F_2$. For zone 1 one can use Formulas 5.5 and 5.6 directly, without having to calculate the resultant force first. However, it becomes clear that due to the reduced height in zone 2 and 3, the resulting force will be larger.

$$F_1 = F_2 = \frac{M}{h_4} \tag{5.7}$$

Looking closely at the part in tension, it becomes clear that it is very similar to the detailed schematization in Figure 5.4. The only difference is the magnitude of the force. Therefore the same formulas can be used to determine the stresses in this element.

Female element
As with the male element, zone 1 and 2 have a reduced height for the bending moment, increasing the resulting forces. Zone 3 has the total height available. The schematization is the same as in pure tension, seen in Figure 5.7, as are the formulas used.

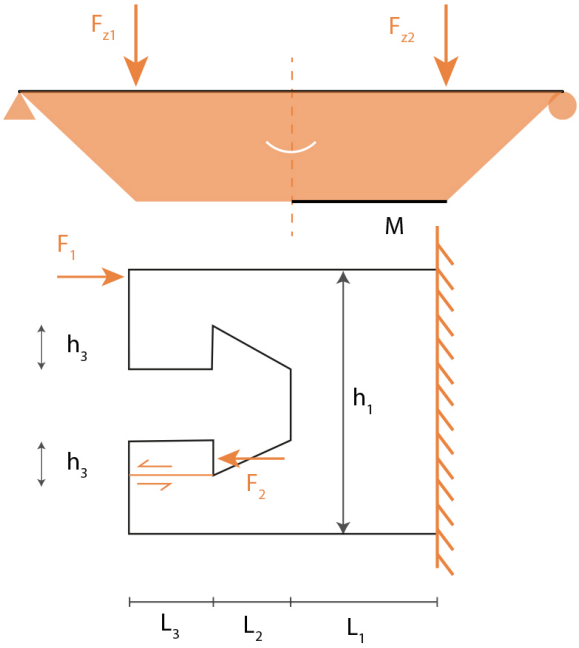

Figure 5.10: Mechanical scheme Gooseneck under a bending moment, female element

5.2.3. KANAWA UNDER TENSION

The sketch in Figure 5.11 shows how all forces are transferred on a small surface, where the dowel is connected to the element. This results in a shear surface in zone 4. Zone 1, 2 and 3 have only normal stresses, with varying height and therefore area. In progression, the height decreases, meaning an increase in normal stresses. The dowel prevents the 2 large elements to separate, by taking up all the tension. Because both elements press onto the dowel from 2 sides, it results in a shear surface. Because the dowel is not balanced due to the eccentricity of the reaction forces, there will also be a small vertical reaction force on the larger elements of the joint.
The other element is identical to Figure 5.11 so will not be discussed separately.

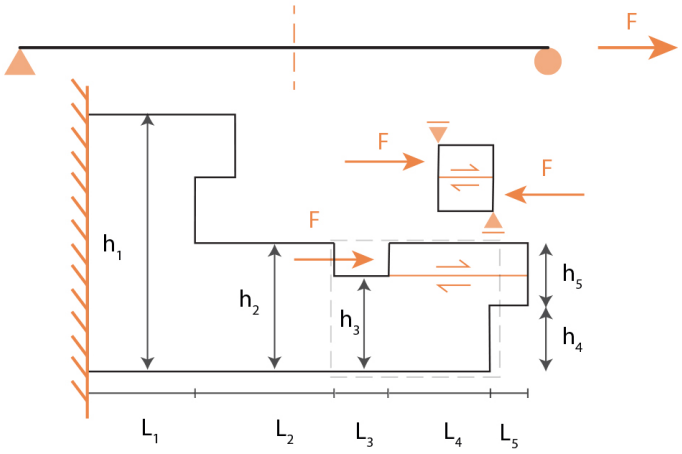

Figure 5.11: Mechanical scheme Kanawa under tension, male element

Considering the schematization of the Kanawa element in tension in Figure 5.12, it is again similar to the other schematized elements. A relevant difference is that the height of section III is much bigger in the Kanawa than in the Gooseneck elements. It is therefore unlikely this area will be critical in the calculations.

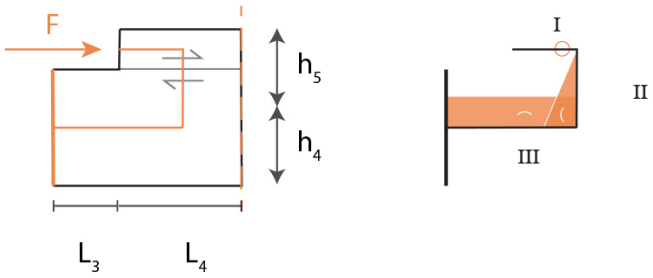

Figure 5.12: Schematization and moment line Kanawa element under tension

5.2.4. KANAWA UNDER BENDING

When applying a bending moment on the Kanawa joint by placing two vertical forces of the beam, this will result in the reaction forces F_1, F_2, F_3 and F_5 shown in Figure 5.13. The mechanism seen in the Kanawa joint under tension is still present, but now has a second system added. This lever arm works horizontally and consists of F_2 and F_5. The exact ratio of the contribution of each of these lever arms is hard to determine with analytical methods.

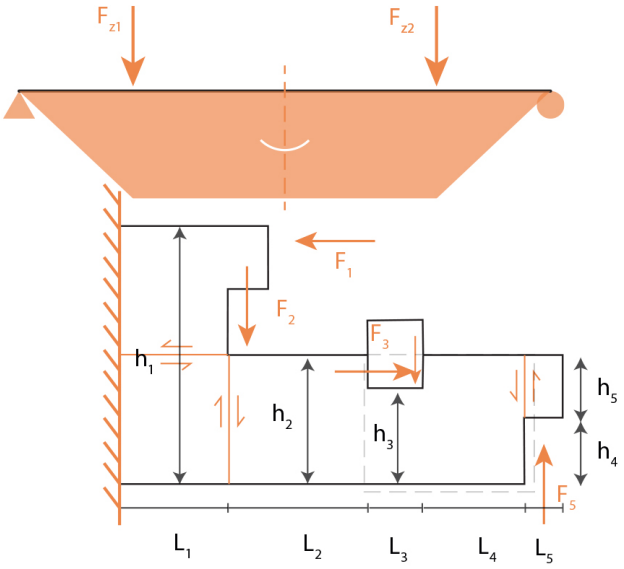

Figure 5.13: Mechanical scheme Kanawa under a bending moment, bottom element

Because this ratio between F_3 and F_5 is hard to establish, the moment line of the schematized element is split into two separate figures, seen in Figure 5.14. Because the horizontal lever arm is much larger, it is expected that the resulting moments from F_5 will be of much larger influence. For practical reasons, in the calculations, F_3 is assumed to be 0.

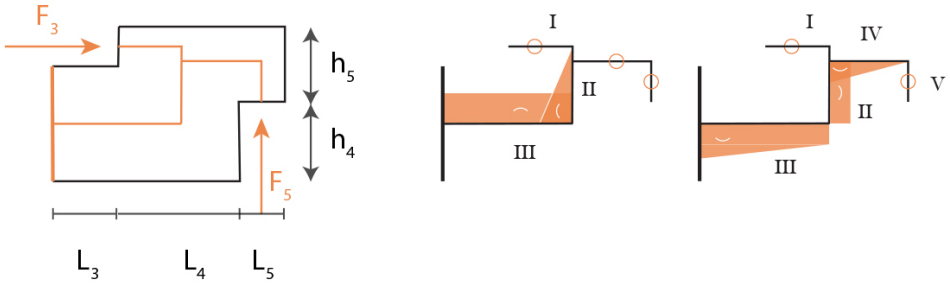

Figure 5.14: Mechanical scheme Kanawa under a bending moment, detail bottom element

Under a bending moment, the top element behaves differently than the bottom element. The schematization is shown in Figure 5.15. The reaction forces resulting in the horizontal and vertical lever arms are the same.

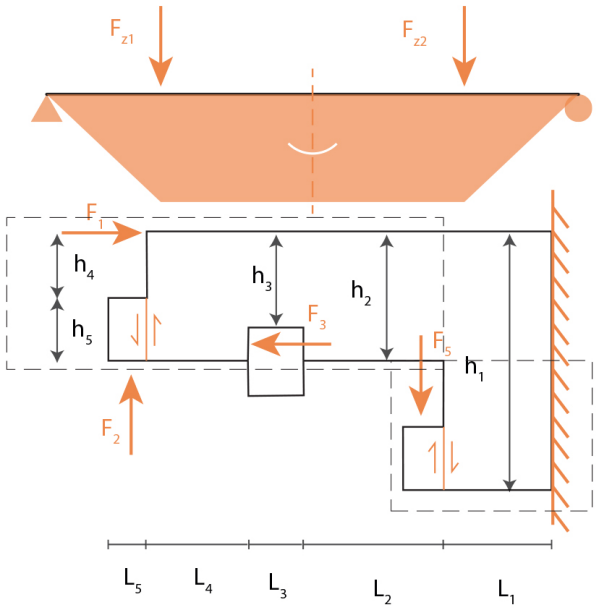

Figure 5.15: Mechanical scheme Kanawa under a bending moment, top element

The resulting bending moments due to the reaction forces do look different than in the top element and are shown in Figure 5.16 and Figure 5.17. As can be seen in Figure 5.16 the resulting moment is large due to the long lever arm to F_5. At the bottom, a second mechanism works with the same magnitude of force, shown in Figure 5.17. However, this lever arm is smaller and therefore also the resulting bending moment.

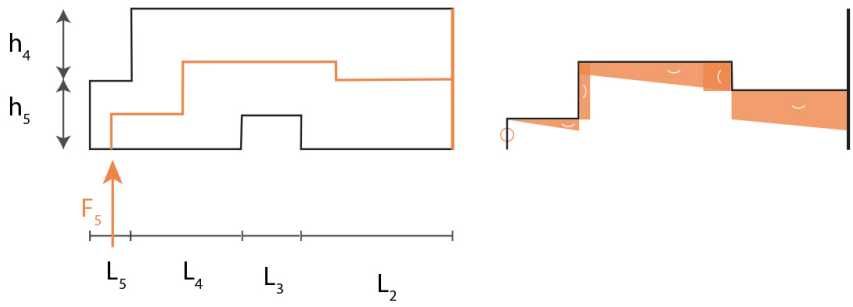

Figure 5.16: Mechanical scheme Kanawa under a bending moment, top element detail

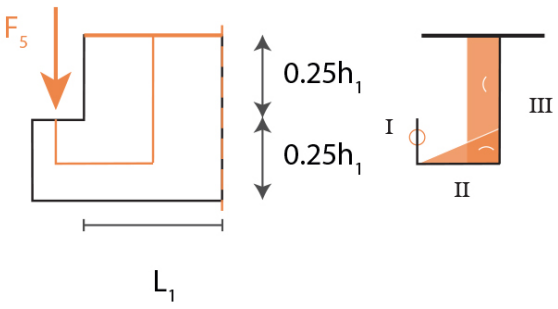

Figure 5.17: Mechanical scheme Kanawa under a bending moment, top element detail 2

5.3. HAND CALCULATION

Each of the schematizations described above will now be used to calculate the expected stresses of each of the designs. The thickness of the glass plates is always 10 mm.

5.3.1. GOOSENECK UNDER TENSION

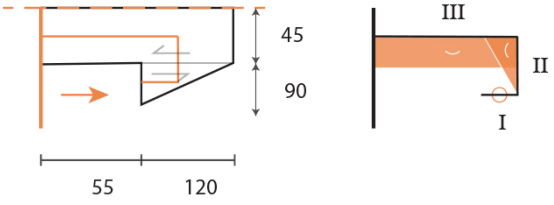

Figure 5.18: Mechanical scheme and resulting moment line Gooseneck under tension, male element

Male element
Section I
2 kN, means 1 kN on each half. The minimum height of the element is approximately 45 mm. This results in.

$$A = 10 \cdot 45 = 450 \text{ mm}^2 \tag{5.8}$$

$$\sigma = \frac{N}{A} = \frac{1000}{450} = -2.2 \text{ N/mm}^2 \tag{5.9}$$

Section II

$$\tau = \frac{V}{bh} = \frac{1000}{10 \cdot 120} = 0.83 \text{ N/mm}^2 \tag{5.10}$$

Bending moment is

$$M = F \cdot L = 1000 \cdot 67.5 = 67500 \text{ Nmm} \tag{5.11}$$

$$W = \frac{1}{6} \cdot b \cdot h^2 = \frac{1}{6} \cdot 10 \cdot 120^2 = 24000 \text{ mm}^3 \tag{5.12}$$

$$\sigma = \frac{M}{W} = \frac{67500}{24000} = 2.8 \text{ N/mm}^2 \tag{5.13}$$

Section III

$$A = 10 \cdot 45 = 450 \text{ mm}^2 \tag{5.14}$$

$$\sigma = \frac{1000}{450} = 2.2 \text{ N/mm}^2 \tag{5.15}$$

Bending moment

$$W = \frac{1}{6} \cdot 10 \cdot 45^2 = 3375 \text{ mm}^3 \tag{5.16}$$

$$\sigma = \frac{67500}{3375} = 20 \text{ N/mm}^2 \tag{5.17}$$

$$\sigma_{total} = 2.2 + 20 = 22 \text{ N/mm}^2 \tag{5.18}$$

The hand calculations of the remaining joints can be found in Appendix A.1.

5.4. CONCLUSIONS

Several of the Sashimono joints discussed in Chapter 4 were modelled to gain a better understanding of their force transfer. First foamboard models were cut in the shape of the joints, and a force was applied to compare deformation under a bending moment. The stiffer joints, namely the Gooseneck and Kanawa joints were further schematized under tension force and a bending moment. This creates more insight into the influence of parameters on the magnitude of stresses in the material, which is critical for the strength of the Sashimono joint. All hand calculations can be found in Appendix A.1.

It is important to note that these are just approximations of the expected stresses. The joints are heavily simplified, therefore these calculated stresses cannot be directly used for the prediction of the numerical models or experiments. They mainly serve from a qualitative point of view to compare the different joints. For example, the calculations do not take into account varying section heights. The joints are modelled as a continuous beam, by taking the centerline of the geometry. A varying section will influence the

way the stresses are distributed over the length of such a schematized beam. This also results in uncertainty about which height to use for the calculations. Another limitation is that stress concentration factors are not taken into account. Especially around sharp corners, this factor will be significant. Lastly, in the calculations shown, all connections are assumed rigid. In reality however, these might behave more like a semi-rigid connection. This will influence the bending moments and therefore also the stress distributions in the glass.

6

NUMERICAL MODELLING

In the previous chapter, some of the Sashimono joints were examined. The Kanawa and Gooseneck designs were further schematized, making it possible to estimate the stresses for the chosen designs. In this chapter, these designs will be examined further using numerical tools. Both the designs will be tested in pure tension, the Kanawa design will also be tested under a bending moment. A description of the Grasshopper, DIANA FEA and Abaqus models will be given. Several parameters will be varied and their influences analyzed. Finally the stresses from the finite element model are given as well as a corresponding sensitivity analysis.

6.1. GENERAL MODEL DESCRIPTION

6.1.1. GRASSHOPPER SETUP

An estimate of the dimensions of the joint can be derived from the analogue modelling. By setting the model up parametrically, these dimensions, as well as the angles can easily be adapted in the following steps.

GOOSENECK MODEL

All relevant parameters can be seen in Figure 6.1(b), which result in the model in Rhino seen in Figure 6.1(a). These are the same parameters used for the schematization in the analytical modelling. On the resulting lines, nurbs were placed, of which the degree could then be varied. Changing the curve degree, changes the curvature of the lines. This results in the rounded shape seen within the boxy original shape.
The length of the neck (L_2) was varied, which had limited effect when keeping it above a length of 40 mm. There was a similar effect for the length (L_3) and width (h_4) of the head. As long as they were above approximately 100 and 200 mm respectively, the curvature of the gooseneck remained large enough, preventing sharp corners. The parameter having the most influence was the width of the chin (L_2). This was because it has an influence

on the area of force transfer and on the width of the section of the female glass panel. To show this, extremes were modelled in DIANA FEA, shown in Figure 6.7.
A detailed description of the Grasshopper and Rhino models of the Gooseneck and Kanawa design can be found in Appendix B.1.

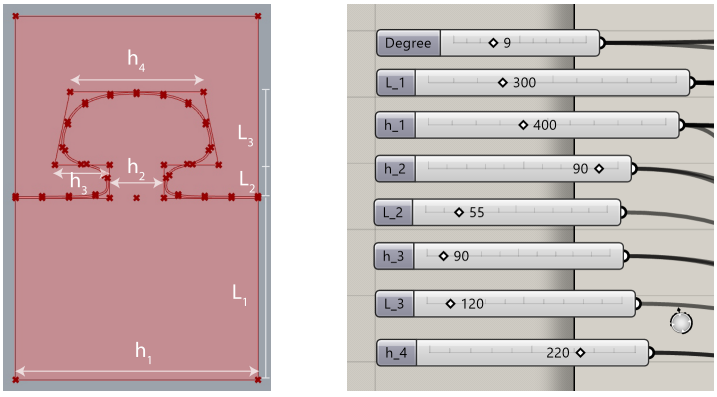

(a) (b)

Figure 6.1: Setup Gooseneck model in Rhino (a) with an overview of parameters in mm in Grasshopper (b)

6.1.2. FINITE ELEMENT MODEL

The solid from Rhino, including the nodes for the mesh, are then exported as a DWG file. Around critical areas, where the contact will take place, more nodes were placed and therefore the mesh could also be finer. Where data would be less relevant at the outer edges, fewer nodes were placed to increase the calculation speed of the models.

GOOSENECK MODEL

The geometry was imported in DIANA FEA as three different 2D parts, as can be seen in Figure 6.2(a). One for the bottom glass panel, one for the interface material and one for the top glass panel. At both the bottom and top edges, the panel is supported in (x) and (y). The top edge has been given a displacement of 3 mm. At the top, a tie is placed, making it easier to export data. A tie means the support and displacement only have to be applied at one node, and the tie will apply the displacement on the entire edge. Because of the way the geometry was exported from Grasshopper, it was easiest to model the whole joint. Calculation time was limited, so decreasing the size of the model was not necessary.
Between the interface material (seen in orange in Figure 6.2), and each of the glass panel interface elements are placed to connect all three geometries. The interfaces are modelled nonlinear as no-tension with shear stiffness reduction, to ensure the interface material will not take up any tension, but simply separate from the glass. All material properties that were used as input are shown in Table 6.1 below. At this stage, it was assumed

Surlyn would be used as an interface material.

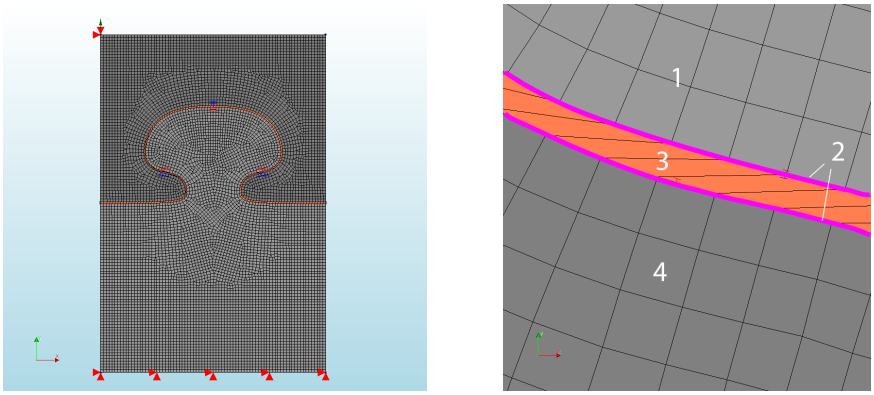

(a) (b)

Figure 6.2: Setup FEM Gooseneck in DIANA FEA, global model showing supports and displacement (a) and detail of the interface material showing the top glass panel (1), the interfaces (2), interlayer material (3) and bottom glass panel (4) (b)

Analysis	Structural
Dimension	Two dimensional
Default mesher type	Hexa/Quad
Default mesh order	Quadratic
Mid-side node location	On shape

-	Unit	Surlyn	Glass
Young's modulus	MPa	100	70000
Poisson's ratio	-	0.449	0.23
Mass density	kg/m^3	950	2500

-	Unit	Interface
Type	-	2D line interface
Normal stiffness modulus	N/m^3	1e+15
Shear stiffness modulus	N/m^3	1e+06
Nonlinearity	-	No-tension with shear stiffness reduction

Table 6.1: All relevant data for the Gooseneck DIANA FEA model

A structural nonlinear analysis was then performed on several alterations of the Gooseneck design, which will be discussed in detail in Section 6.2. The model was set to 50 load steps.

KANAWA MODEL

Due to the geometry of the Kanawa joint, it turned out extremely complex to model the interfaces in DIANA FEA. It was therefore decided to switch to modelling in Abaqus instead. In this software, the geometry was imported as DWG, STEP, SAT and IGS file. It turned out that the IGS file type imported the geometry most accurately, meaning, with minimal penetration of the interface material and glass. Also, the lines were smooth instead of angular.
The geometry was imported as four separate parts: the top glass pane, the bottom glass pane, the dowel glass pane and the interface material as one solid element, see Figure 6.3.

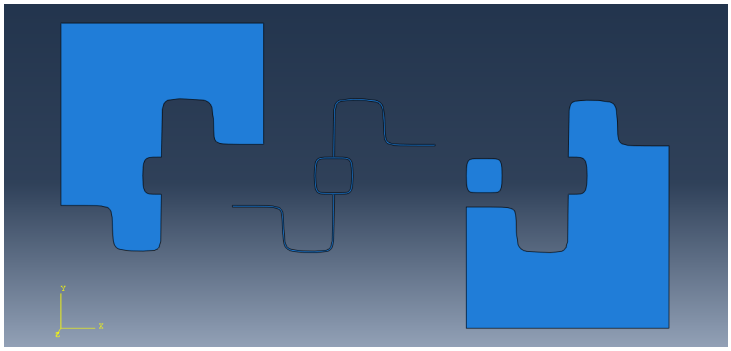

Figure 6.3: Imported Kanawa parts for Abaqus model

The separate parts were then connected using interaction elements as seen in Figure 6.4. The interactions were modelled using finite sliding and surface to surface discretization method. The friction coefficient is set to 0.5. As described in Chapter 3 the friction coefficient between polymers and steel is between 0.2 and 0.6 (Zeus, 2005). Because the edges of the glass are expected to be rougher than the surface of steel, an estimate of 0.5 is chosen. Material properties are set up the same as with the Gooseneck joint, seen in Figure 6.1.

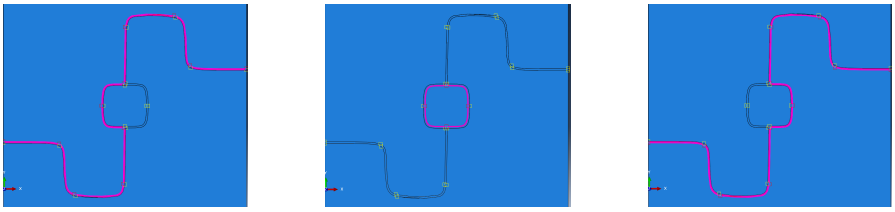

(a) (b) (c)

Figure 6.4: Setup left (a), middle (b) and right (c) interfaces Kanawa model in Abaqus

At the bottom, the glass panel is constrained in x and y directions, at the top only in the x direction, seen in Figure 6.5(a). In the center around the interfaces, the mesh has to be fine enough to do calculations in the interface material. To achieve this, local seeds were applied to the edges in the middle, seen in purple in Figure 6.5(b). The calculation was started with a larger mesh but failed to converge. The mesh was refined every time in an attempt to reach convergence. The mesh discussed was the first mesh that achieved this. Wider seeding is applied at the outer edges of the total panel. The combination of these seedings results in the irregular mesh seen in the same figure. Unfortunately, due to the irregular geometry, this still resulted in some non-square meshing as can be seen in Figure 6.5(c).

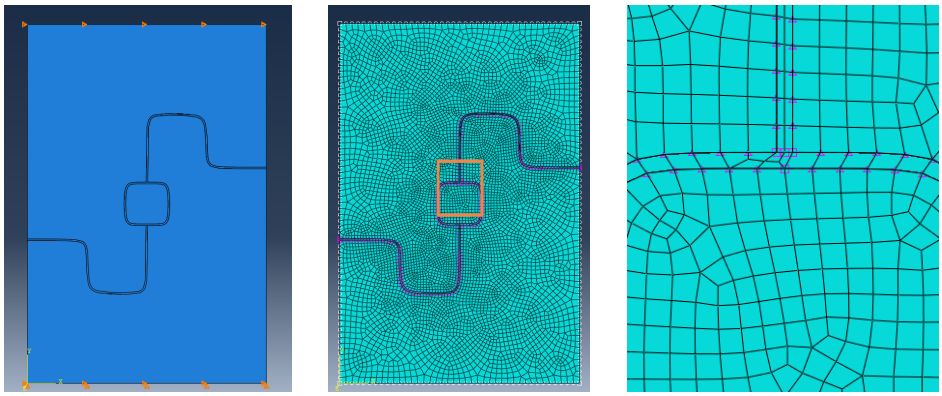

(a) (b) (c)

Figure 6.5: Supports (a), mesh (b) and detail of the mesh (c) of the Abaqus model

GOOSENECK 2.0

To better compare the FEM of the Kanawa with the Gooseneck model, the latter was also modelled in Abaqus. The geometry shown in Figure 6.6(a) was imported using the same procedure as for the Kanawa geometry. One part for the bottom glass panel, one part for the interlayer geometry (shown in pink in Figure 6.6(b)) and one part for the top glass pane. The parts were connected using interaction elements, shown in orange in Figure 6.6(b). The mesh was set up using edge seedings, to ensure the mesh over the interlayer is rectangular. All other parameters were set up the same as the Kanawa model.

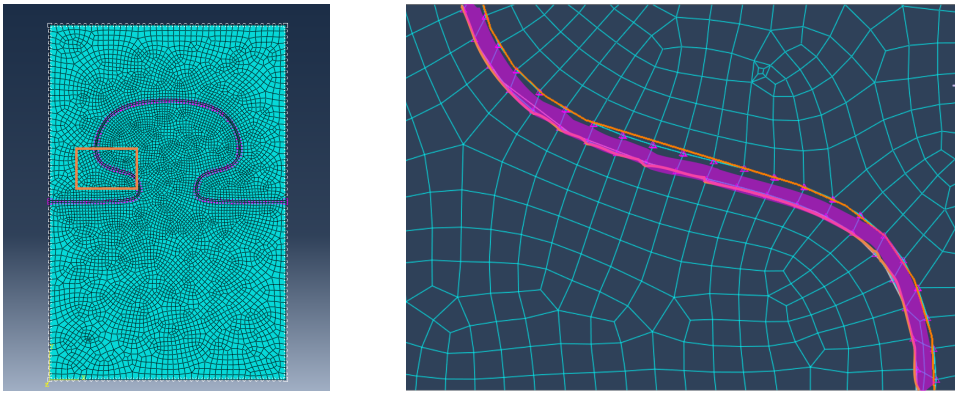

(a) (b)

Figure 6.6: Setup FEM Gooseneck in Abaqus showing the total model (a) and a detail of the interlayer in pink (b)

6.2. DESIGN CHOICES

Based on the analytical modelling the optimal dimensions for both designs were estimated. To check these designs, two extremes were also considered. This contributed to an additional understanding of the influence of shape on force transfer.

GOOSENECK DESIGN

Almost every parameter could be varied in the design due to the Grasshopper model. But since force is transferred at the 'chin' of the Gooseneck, the dimensions of this area are expected to be most influential on force transfer and therefore stress distributions.
In Figure 6.7(a) the width is set up with minimal dimensions. The advantage is that peak stresses due to eccentricity are limited as can be seen in Section 5. However, this design also has a relatively small surface where forces can be transferred. According to formula 5.3 this results in higher normal stresses. Due to the smooth geometry, the concentration is also expected to be low. According to the DIANA FEA model, this design has peak stresses of 93 N/mm^2. Han calculations give an estimate of 21.5 N/mm^2.
Figure 6.7(b) shows the expected optimal dimensions. The width of the chin is increased compared to Figure 6.7(a) and therefore has a larger lever arm, and increased stresses due to the eccentricity of force transfer. But the increased area of force transfer also decreases normal stresses. The resultant peak stresses according to the model are 85 N/mm^2.
The extreme minimal width results in 9.4% higher peak stresses than the designed optimum. Hand calculations give the same peak stresses as the design in Figure 6.7(a).
Lastly, in Figure 6.7(c) the chin is made extremely wide. This results in much larger stresses due to eccentricity, and an even further decrease of normal stresses. Normal stresses also increase at the smallest section of the female part. Because the chin gets wider, this section automatically becomes more narrow. The influence of the eccentric-

ity seems to be most influential, because the peak stresses are 140 N/mm^2. Due to the geometry though, factor K has most likely also increased significantly, playing an important role in the resulting peak stresses. This design causes a stress increase of 67% compared to the aimed design. Hand calculations give an estimate of 141 N/mm^2.

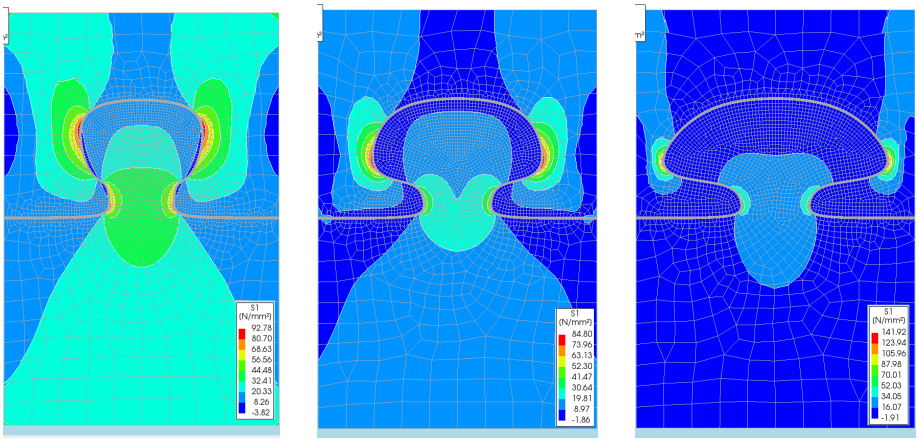

(a) (b) (c)

Figure 6.7: Three variants of the Gooseneck design and its FEA at a displacement of 1 mm, resulting in stresses of 93 N/mm^2 for a chin width of 30 mm (a), 85 N/mm^2 for a chin width of 90 mm (b) and 140 N/mm^2 for a chin width of 150 mm (c)

KANAWA DESIGN

The same procedure was followed with the Kanawa design. This was first modelled in pure tension and later also in bending. In pure tension, all the force is transferred by the dowel. Therefore only the size of the dowel was varied. When the dowel is small as in Figure 6.8(a), the surface over which the stresses can be transferred is very small. This will therefore increase local normal stresses. A great advantage is that the width of the critical section remains maximal and the eccentricity minimal.
In Figure 6.8(b) the estimated dimensions are shown. There is a balance between the area of force transfer, minimal eccentricity and maximal width of the critical section.
When maximizing the size of the dowel, intuitively large forces can be transferred. Unfortunately, there remains only a tiny section between the corner of the dowel and the remaining geometry. This is also where large stresses will accumulate due to the eccentricity of the line of force. Therefore the design in Figure 6.8(c) will likely fail under small forces already and is not a suitable design.

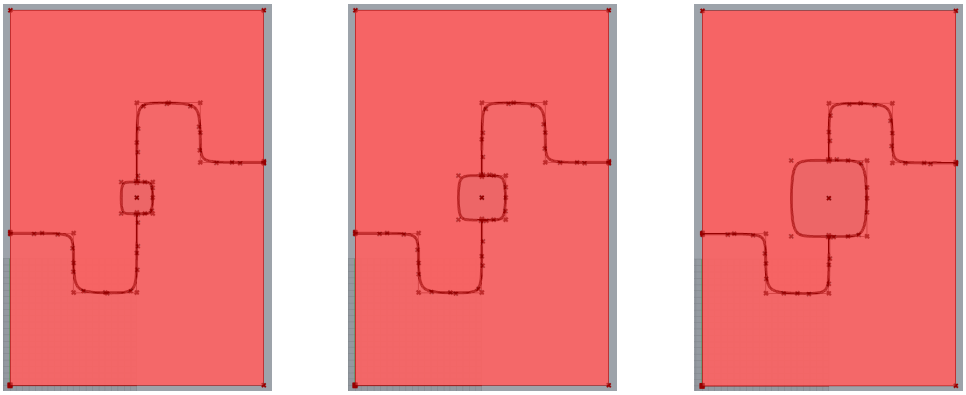

(a) (b) (c)

Figure 6.8: Three variants of the Kanawa design in Grasshopper, dowel width of 50 mm, 12 N/mm^2 peak stress (a), 75 mm, 16 N/mm^2 peak stress (b) and 120 mm, 90 N/mm^2 peak stress (c)

6.3. RESULTS

To better compare the designs the Gooseneck design was later also modelled using Abaqus with the same input data seen in Table 6.1. The final models at 2 mm displacement are shown in Figure 6.10. The Gooseneck model (Figure 6.10(a)) has peak stresses of approximately 300 N/mm^2 with a reaction force of 5.6 kN. For the Kanawa model (Figure 6.10(b)) this is approximately 60 N/mm^2 for a reaction force of 1.3 kN. The beam model (Figure 6.10(c)) gives an estimate of stresses around 70 N/mm^2 with a reaction force of 1.1 kN.

According to hand calculations, the peak stresses at this same location would be 35 N/mm^2 for the Gooseneck model at a force of 5.6 kN. For the Kanawa under pure tension, this would be 16 N/mm^2 for 1.3 kN. For the Kanawa beam, this would come down to 26 N/mm^2 for 1.1 kN. This corresponds with a bending moment of 0.61 kNm. This means the stress intensification factor is probably around 3-4.

In Figure 6.11 the contact pressure of the three designs is shown at a displacement of 2 mm. For the Gooseneck joint, the maximum pressure is 57 N/mm^2, for the Kanawa joint it is maximum 42 N/mm^2 and for the Kanawa joint under bending it is maximum 14 N/mm^2. This is relevant input to estimate the required strength of the interlayer.

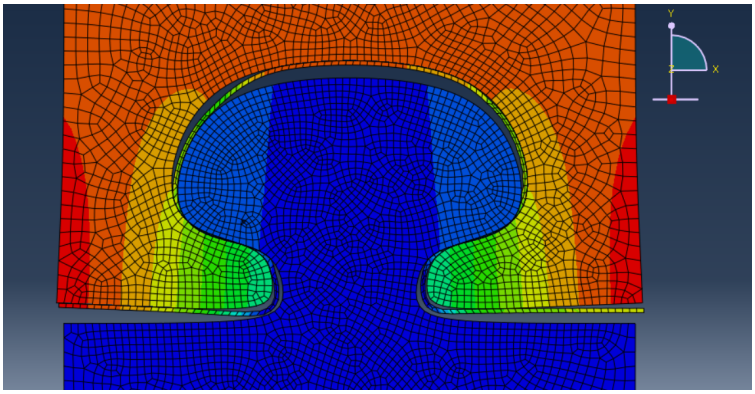

(a)

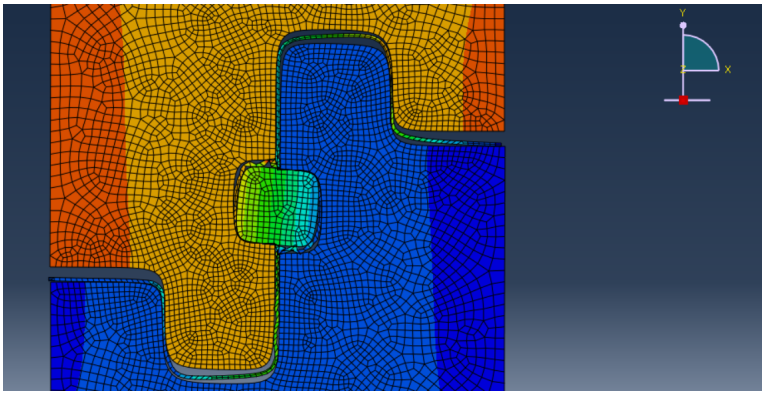

(b)

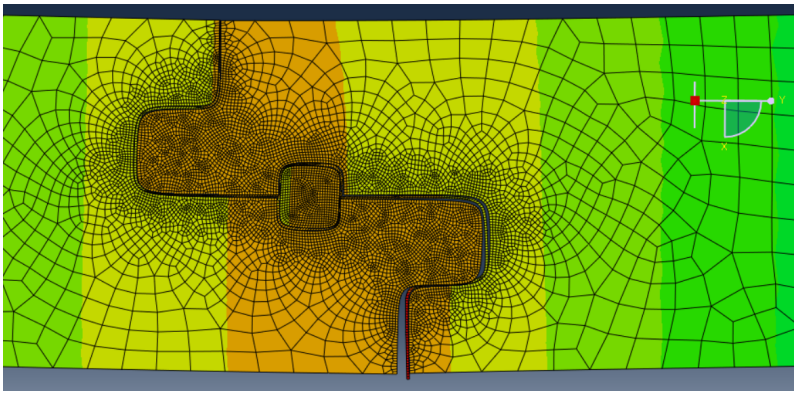

(c)

Figure 6.9: Deformation behaviour with a scale factor of 5 of Gooseneck (a), Kanawa (b) and Kanawa in bending (c), at 2 mm displacement

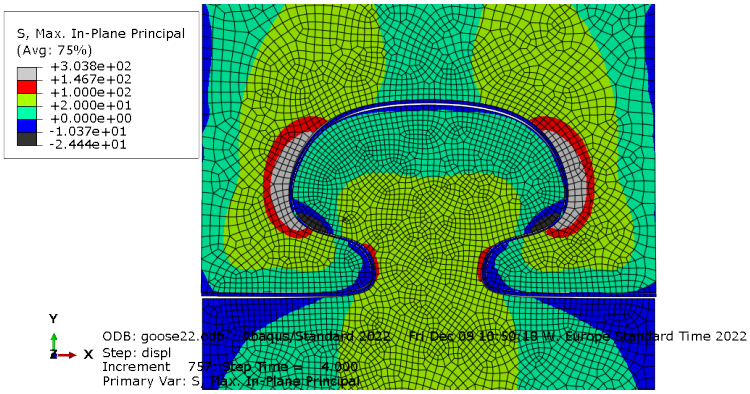

(a)

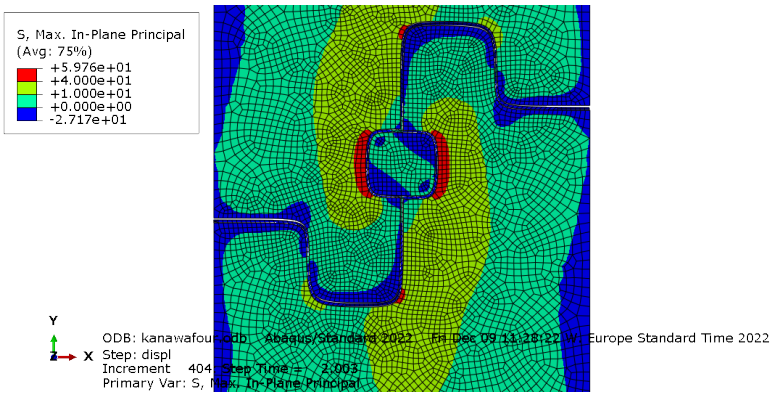

(b)

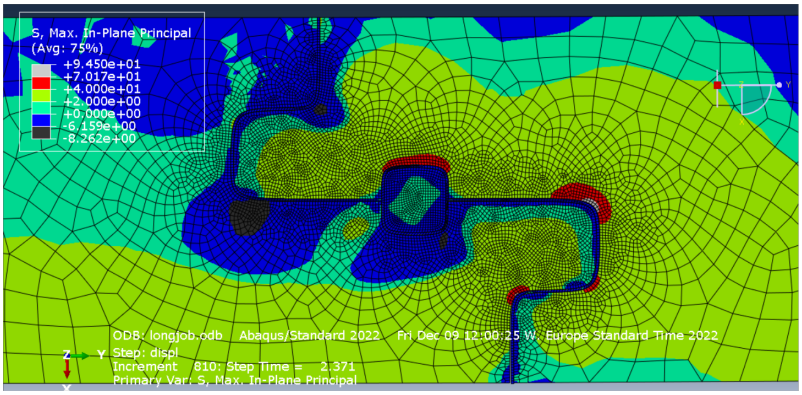

(c)

Figure 6.10: Final models of Gooseneck (a), Kanawa (b) and Kanawa in bending (c), showing principal stresses at 2 mm displacement

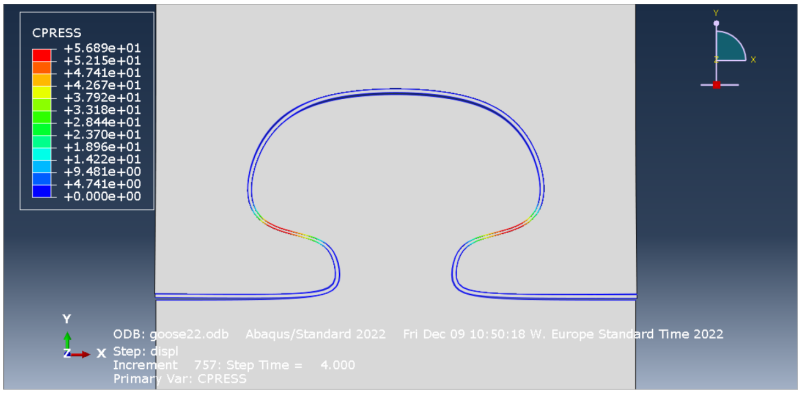

(a)

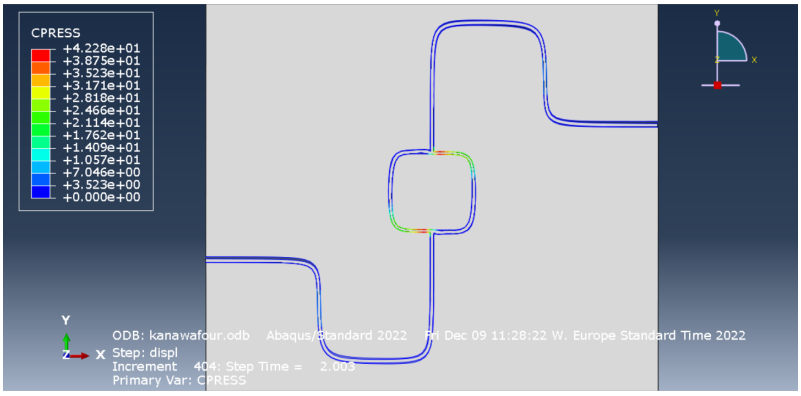

(b)

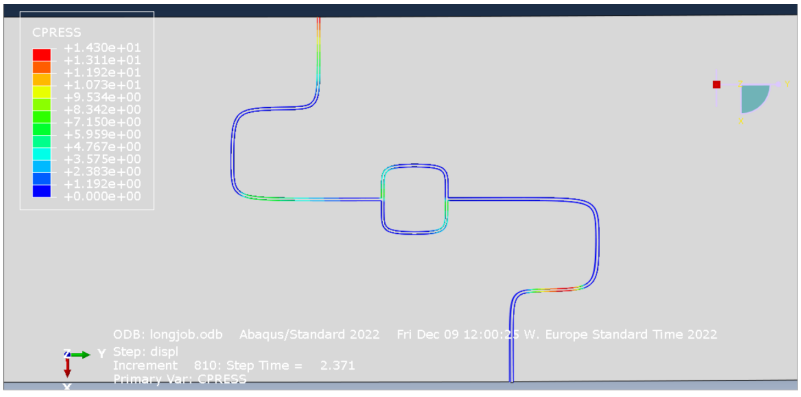

(c)

Figure 6.11: Final models of Gooseneck (a), Kanawa (b) and Kanawa in bending (c), showing contact pressure at 2 mm displacement

6.4. SENSITIVITY ANALYSIS

To acquire more certainty about whether these models are functioning well, several sensitivity analyses were performed. The friction coefficient between the glass and interlayer, and the stiffness of the interface material were varied to different extreme values. If one of these extremes would give unexpected values, then the whole model is uncertain.

6.4.1. FRICTION COEFFICIENT

First, the friction coefficient between the glass and interlayer was varied. In the used model a coefficient of 0.5 is used. The maximum value used is 1 and the minimum value 0.001. When the lower boundary was set to 0, this caused the models to be very unstable and the calculations would be aborted. In Figure 6.12 it can be seen that increasing the friction has a limited effect on the behaviour of the model. The total stiffness of the used model is 2.8 N/m, that of the model with maximum friction is 2.9 N/m. Practically removing friction results in, as expected, less stiff behaviour. The stiffness becomes 2.0 N/m. This is a decreased stiffness of 29%. So far no reason to suspect the model is unreliable.

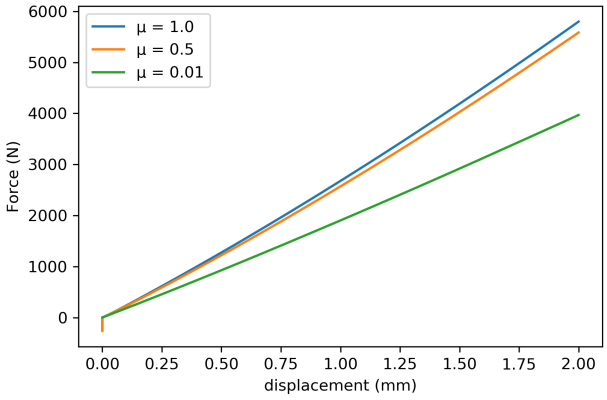

Figure 6.12: Plot showing the stiffness of the Gooseneck model with different friction coefficients

The results of applying the same friction coefficient variation on the Kanawa model, can be observed in Figure 6.13. Increasing the friction does have quite an influence on the stiffness of the model. Additionally, due to its geometry, the whole model already fails before reaching 4 mm displacement. When the displacement gets too large, the whole interface material is pulled out of the geometry. All three models show similar parabolic behaviour. At 3.5 mm displacement, the used model has a stiffness of 0.99 N/m. The maximum friction results in 1.3 N/m, and minimal friction in 0.44 N/m. This is a 35%

increase and a 55% decrease.

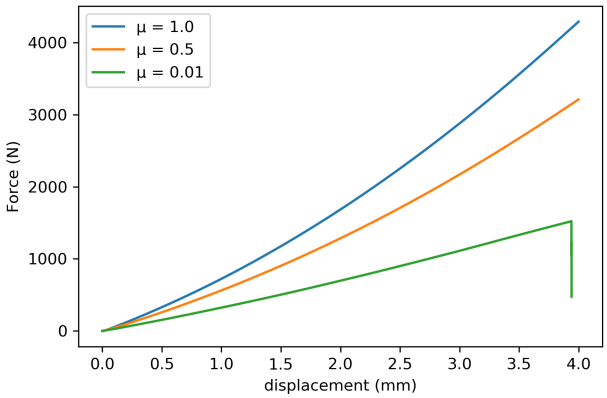

Figure 6.13: Plot showing the stiffness of the Kanawa model with different friction coefficients

The Kanawa model when imposing a bending moment on it behaves quite similar to that of the Gooseneck seen in 6.12: limited influence of a high friction coefficient, quite some influence when removing it. With maximum friction, the stiffness is 0.63 N/m. With no friction, so free slipping it is 0.38 N/m. The model used has a stiffness of 0.55 N/m. The model therefore seems within reliable boundaries.

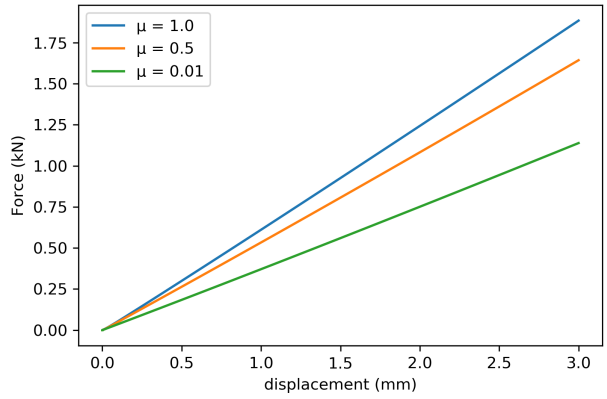

Figure 6.14: Plot showing the stiffness of the Kanawa beam model with different friction coefficients

Material NLE

In the used model the interlayer material behaves linear elasticcally. In reality, the ma-

terial will behave nonlinear elasticcally. To check the influence, the material properties of the interface were altered, by adding a *fail strain* suboption. The properties can be found in Table 6.2.

Tension strain fiber direction	0.0004
Compression strain fiber direction	0.4
Tension strain transverse direction	0.0004
Compression strain transverse direction	0.4
Shear strain	0.0001

Table 6.2: Input for the fail strain material properties of the interlayer material

When plotting the F-δ graph of this model with altered material properties, there turns out to be no difference in the results of the behaviour of the overall model. This can be explained by the fact that in the model the maximum stresses in the interlayer material is approximately 23 MPa, so it does not exceed the set limit of 40 MPa.

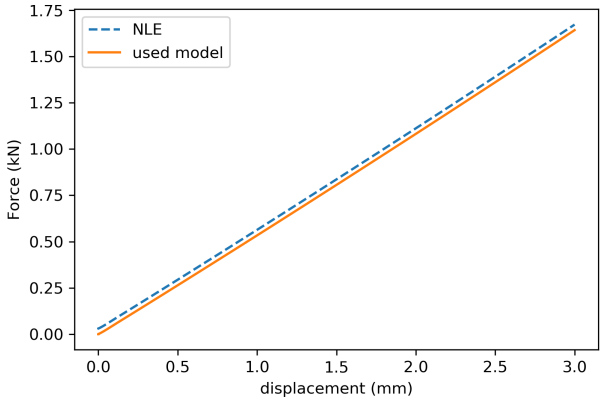

Figure 6.15: Plot showing the stiffness of the Kanawa beam model using a material nonlinear elastic model, NLE line slightly moved upward for clarity. In reality, the lines overlap.

6.4.2. STIFFNESS INTERLAYER MATERIAL

To check the sensitivity regarding the stiffness of the interlayer material, this was also checked in Abaqus. In the used model, the Young's modulus was 100 MPa, based on the material properties of Surlyn. The maximum stiffness was set to 200 MPa and the minimum to 10 MPa. In the Gooseneck model, increasing the stiffness had no surprising effect, as can be seen in Figure 6.16. The decrease however had a huge impact, since it drops the overall stiffness to a constant near zero. This can be explained, because the thickness of the material is 3 mm and the plot only shows displacements until 2 mm. If the stiffness is so low, it makes sense that first the interlayer will be compressed fully.

Hardly any force is required to do this. Stresses in the glass will therefore also be near zero.

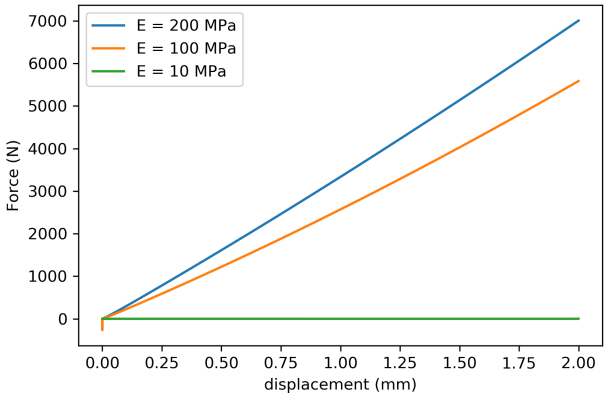

Figure 6.16: Plot showing the stiffness of the Gooseneck model for varying interlayer stiffness

For the Kanawa joint, the influence of the stiffness is as expected, seen in Figure 6.17. All models behave parabolic. Just as with the Gooseneck model in Figure 6.16, decreasing the stiffness results in a near zero stiffness. However, in this case, the model is shown for 4 mm displacement, which means the interlayer is already fully compressed. Therefore, even the lowest stiffness will eventually start building up some force in the joint. Because the material is fully compressed, large displacements will take place, causing large local stresses in the joint.

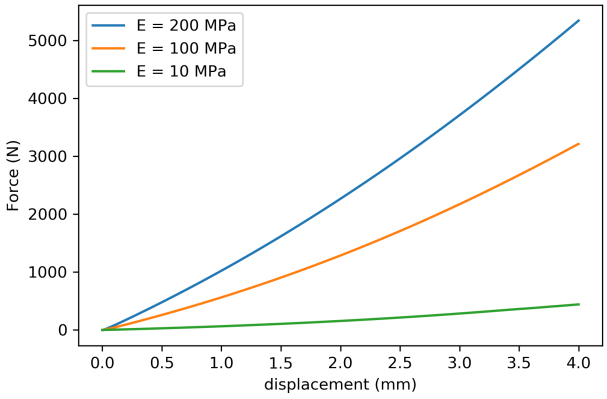

Figure 6.17: Plot showing the stiffness of the Kanawa model for varying interlayer stiffness

The Kanawa model under bending, for varying stiffness, can be seen in Figure 6.18. Interestingly, the exact same model already behaves much stiffer than the model in pure tension as seen in Figure 6.17. This means the geometry itself is stiffer under this mechanism. Increasing the stiffness increases the stiffness as a whole. When decreasing the stiffness, something striking happens. The model is still relatively stiff compared to the tension tests. Also, the plot seems to become slightly parabolic. This causes the shape of the plot to resemble the joint in tension a bit.

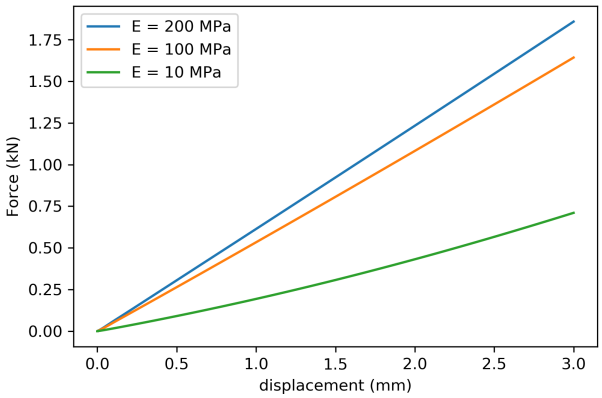

Figure 6.18: Plot showing the stiffness of the Kanawa beam model for varying interlayer stiffness

6.5. CONCLUSIONS AND DISCUSSION

The force transfer of the Gooseneck and Kanawa joints was optimized using hand calculations, Grasshopper and finite element models. The Grasshopper model allowed for easy variation of several parameters, which appeared influential from hand calculations. These considered for example dimensions and curvature of angles in the designs. The most dominant parameters for the Gooseneck design are the curvature of the angles and the width of the chin. To check the influence of these parameters, some of these variations were modelled using finite element analysis. The purpose of these models was to compare the variations to each other from a qualitative point of view, not to present any predictions.

The Gooseneck model was set up in DIANA FEA, and the Kanawa models in Abaqus. In a later stage, the Gooseneck model was also built in Abaqus. Because all of the designs are reliant on proper interface behaviour, it is strongly recommended to use Abaqus for future research. The main problem encountered in DIANA FEA was that the software was unable to connect one element to multiple interfaces, which was necessary for the Kanawa geometry. Additionally, DIANA FEA only allows the geometry to be imported as DWG files, giving a lot of additional nodes on the edges of the geometry. Lastly, Abaqus allows for the easy modelling of friction, an option DIANA FEA does not have. The dis-

advantage of Abaqus is that this software is less suitable for potentially writing a python script that would automate the generation of new models after making variations in the grasshopper model.

Proper meshing is crucial. Because of the complex geometry, it is quite challenging to create a hexagonal grid. However, the stability of the model heavily depends on it. By creating local seedings at the contact edges, the meshing can be done as accurately as possible.

For the design of glass, make sure all edges are filleted to decrease the stress concentration factor, since this has a large influence on peak stresses. Also ensure sections do not end up getting too narrow, strongly increasing normal stresses.

The Gooseneck model already results in extremely high peak stresses at 2 mm displacement, the Kanawa tension and beam model seem to be less stiff. These two models are expected to be able to move more than 2 mm.

The model responds well to all sensitivity analyses, and therefore there is no reason to believe the model of the chosen designs is unreliable. Sufficient stiffness of the interlayer material is necessary for the joint to work. The friction coefficient between glass and the interlayer was taken from an estimate made in section 3.2.3. It becomes clear from the sensitivity analyses that this value is of quite some influence on the stiffness of the joints when modelling them. It is therefore recommended to acquire experimental data on a representative coefficient of friction between each of the interlayers and glass.

In the models described, crack propagation and time-dependent effects due to creep were not modelled. The failure of the joints does not originate from an inherent strength, but from a statistical value based on existing cracks. The models are therefore only used to gain more insight into the stress distributions and not for the point of failure. Additionally, polymers will exhibit time dependent behaviour such as creep. The objective of these models was to gain a better understanding of the force transfer during the experiments. It is recommended to also model this creep in future behaviour, to check the behaviour of the joint in the long term.

One way to model the fracture behaviour of glass is described by Verleg, 2019. Existing flaws are modelled in the glass using finite elements with different strengths. The strength of each of these finite elements is drawn from a Weibull distribution. Because of the varying orientation and size of the flaws, multiple different Weibull distributions will have to be used to accurately model the glass. Applying this same procedure to the Sashimono models will give a prediction of the breaking points in the joints.

III

EXPERIMENTAL RESEARCH

7

EXPERIMENTAL RESEARCH

The following chapter will elaborate on the experiments of this research, describing the used methods and the results. The objective of these experiments is twofold. Firstly, to validate earlier modelling by hand as well as the finite element analysis. And secondly, to gain insight into the failure behaviour of the designed joints. This will contribute to answering the final two research questions.

- What is the influence of shape on force transfer and how can this interaction be optimized in a glass Sashimono connection design?
- What is the failure behaviour of the designed Sashimono connection?

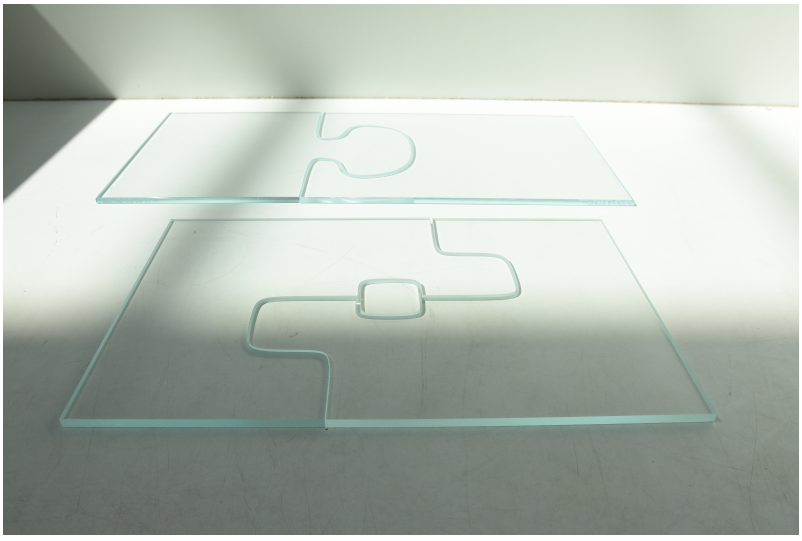

Figure 7.1: Picture of final designs

Two designs were tested, namely an optimized variant of the *Kama Tsugi* and the *Kanawa Tsugi* which were also modelled in Chapter 5 and 6. Respectively these designs will be referred to as the Gooseneck joint and the Kanawa joint. The experimental testing consists of two rounds: one smaller setup performing tensile tests and a larger setup testing the joint in bending. Before conducting the experiments, a small study was done to find a suitable interlayer.

7.1. INTERLAYER

The materials discussed in section 3.2 were ordered and modified to try and fit them between in the glass joint. The materials in question were: PVC, PA6, POM and PU85.

7.1.1. CUTTING

All of the materials were brought to the DEMO lab at the faculty of Electrical Engineering, Mathematics and Computer Science. Here PVC and PA6 were cut into 12mm wide strips using a panel saw. This width was chosen to simplify the demounting of the interlayer during the trial and error for a suitable material. The POM however was too hard to cut using this machine, so a regular bandsaw had to be used. This machine was a lot less accurate and therefore the width over the length of the strip was not perfect everywhere. As can be seen in Figure 7.2 the POM had a very irregular and even sharp edge after the sawing. This had to be sanded off afterwards by hand. Because of the flexibility of the PU85, it could not be sawed for safety reasons. Therefore a steel cutter was used. This did damage the edges of the PU85 strips.

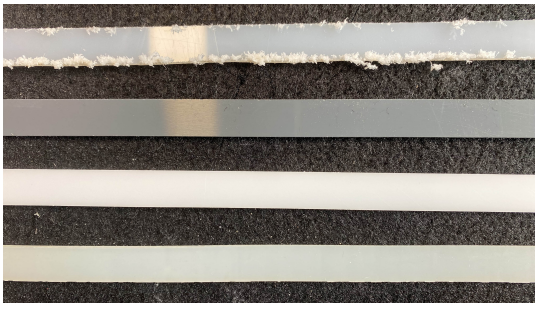

Figure 7.2: Selected interlayers from top to bottom: POM, PVC, PA6 and PU85

After cutting the materials to size, it was attempted to assemble each of the materials in between the geometry of the glass panes.

7.1.2. DIRECT ASSEMBLY

First, it was attempted to assemble materials between the geometry directly. It immediately became clear that only the PU85 was flexible enough to fit around the geometry

of the Kanawa joint, as can be seen in Figure 7.3. None of the other materials fit between the panels directly. Especially the PA6 was very hard to bend. PVC and POM were bendable, but not nearly sufficient. For the Gooseneck joint, not even the PU85 fit between the panels, because the geometry was too tight. In an attempt to solve this, the PU was frozen overnight in order for the material to shrink and then squeezed between the Gooseneck joint. This was still not successful, unfortunately.

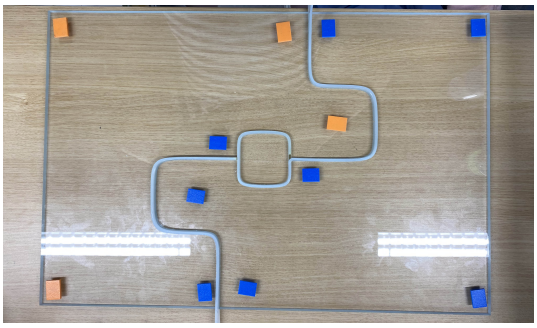

Figure 7.3: PU85 fitted between the Kanawa geometry

7.1.3. ASSEMBLY AFTER HEATING

In an attempt to make the other materials more flexible, they were slowly heated in a Thermo Scientific Heraeus Function Line Heating and Drying Oven. For all materials their service temperature (ST) was checked which are listed in Table 7.1, along with the head deflection temperature (HDT) and short term maximum temperature (T_{max}). Data is extracted from technical data sheets in Appendix C.2.

Material	ST (C^o)	HDT (C^o)	$T_{max}(C^o)$
PVC	0-60	74	70
PA6	-40-85	75	160
POM	-50-100	110	140
PU85	-40-70	-	-

Table 7.1: Long term service temperature (ST), heat deflection temperature (HDT) & short term max temperature (T_{max})

Each of the materials was then heated using steps of 10 C^o, added to room temperature. The materials were left in the oven for 10 minutes to ensure they were fully heated. It was expected that the materials would be satisfactorily formed at HDT.

PVC

For PVC the HDT is above ST and even above the maximum temperature. Initially, this posed an undesired situation. The material did not become any more bendable than at room temperature, up to a temperature of 50 C^o. When bending it at this temperature,

the material yielded in a very unfavourable way. It resulted in sharp angles when bending the material, seen in Figure 7.4. The use of this material was therefore discarded.



(a) (b)

Figure 7.4: Deformation of the PVC when bending the material at 50 C^o

PA6

PA6 appears very suitable, because the HDT is even below ST. Already at 70 C°, the material was very bendable. It almost fitted in the curvature of the Gooseneck joint, seen in Figure 7.5(a). The material was heated further up to a 100 C°, after which the material fit almost completely as can be seen in Figure 7.5(b). It appeared the material was not going to fit fully, even after a further increase in temperature. After this, the experimentation with PA6 was aborted.

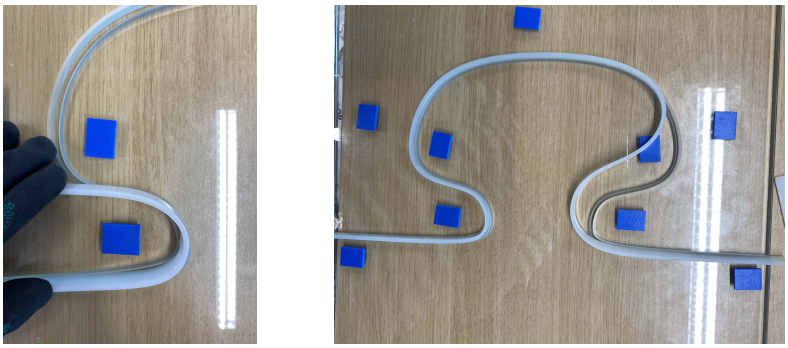

(a) (b)

Figure 7.5: Fittin PA6 between the Gooseneck design at 70 C° (a) and at 100 C° (b)

POM

POM showed very similar behaviour to the PA6, with a good ability to bend the material at 85 C°. Because of its sharp edges however, it was much harder to handle and fit between the geometry. Since the PA6 was already unable to fit between the panels, it was decided to no longer heat up the material to higher temperatures.

7.1.4. ALTERNATIVE ASSEMBLY

Only the PU85 appeared to be able to make the full curvature for the geometry and did not have to be heated to do so. It fitted directly between the Kanawa design, but unfortunately, it still could not fit in the Gooseneck design. As an alternative solution, the edges of the glass were filed with the help of the glass manufacturer. Unfortunately, this caused some damage and worse edge quality. With the help of some silicone spray and a soft wooden hammer, the PU could eventually be squeezed in between.

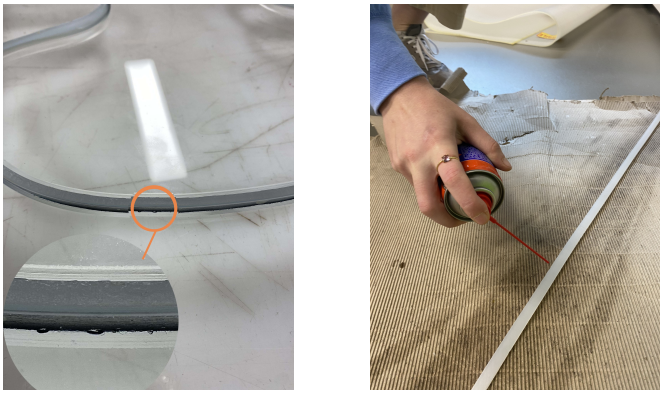

(a) (b)

Figure 7.6: Damage from additional polishing (a) and silicone spray (b)

The edge before and after the polishing were compared under the microscope. In Figure 7.7(a) the lines from the machined polisher are visible, with very limited surface flaws. In Figure 7.7(b) the pattern is very irregular and the depth of the flaws is much deeper.

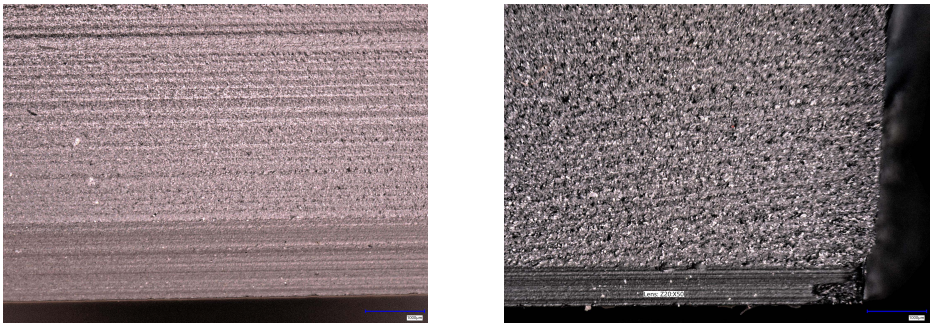

(a) (b)

Figure 7.7: Detail of the original polished edge (a) and the manually polished edge (b) 50x zoom

7.2. TENSILE TESTS

The two designs were tested at the material science lab at the faculty of 3mE of TU Delft, to assess their performance in pure tension. Due to minimum sizing of the glass required for the CNC, it was decided to test the samples on 1:1 scale.

7.2.1. DESCRIPTION SETUP

The glass samples are assembled and attached to a Zwick100 with the use of aluminium and steel plates. The aluminium plates were glued to the glass, to which the steel plates were bolted. These were in turn bolted to the top and bottom of the machine. In 7.8(a) an impression can be seen of the bottom of the setup and in 7.8(b) the total setup is mounted into the machine. This way the glass could be attached to the machine without causing peak stresses in the glass around the connections. The setup creates a double hinge, which prevents any unwanted internal moments in the glass. The samples were assembled beforehand, and then placed into the machine, to minimize the risk of any misalignment.

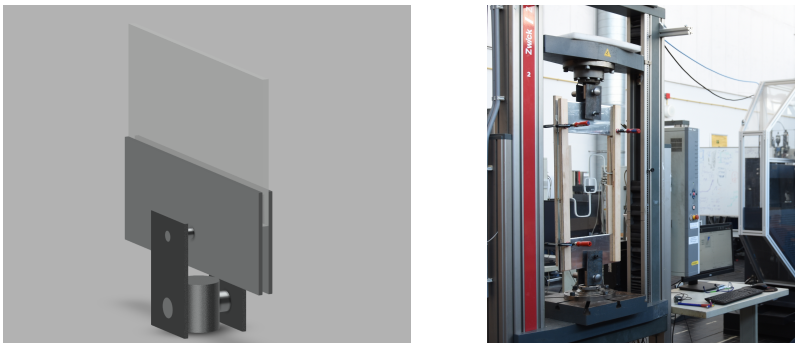

(a) (b)

Figure 7.8: Setup tensile tests showing the glass between the two aluminium plates in light grey, attached to the steel plates in darker grey (a) and the setup containing the Kanawa sample at the Faculty of 3mE (b)

PRODUCTION GLASS

The Gooseneck joint was cut using a CNC milling machine and then polished, since this option was sponsored by industry partner *Van Dijken glas bv.* Like with a jigsaw, the blade has a thickness. This had 2 implications in the case of milling the Gooseneck samples. Firstly, the blade could not make a sharp turn, because it might have caused the glass to break. Therefore the milling blade entered the glass pane from one side, stopped at the tip of the head and then did the same from the other side. Secondly, the blade was thicker than the 3 mm gap left for the interface material. Therefore, the male and female part of the joint had to be cut from two separate glass panes. After milling the samples, the edge quality was quite bad. This made the samples more susceptible to fatal damage and is also more dangerous to handle. Therefore, the edges were polished. When polish-

ing glass, the edges of the glass get an additional angle, preventing peak stresses at the corners. These edges are visible in Figure 7.9(b).

Due to its geometry, however, this was not an option for the Kanawa joint. It was therefore decided to transport the sponsored glass to another company which had the possibility to waterjet the glass panels into the right geometry. The edges of the waterjet samples were not polished, as can be seen in Figure 7.9(a). The two designs were susceptible to differences in both tolerances and edge quality.

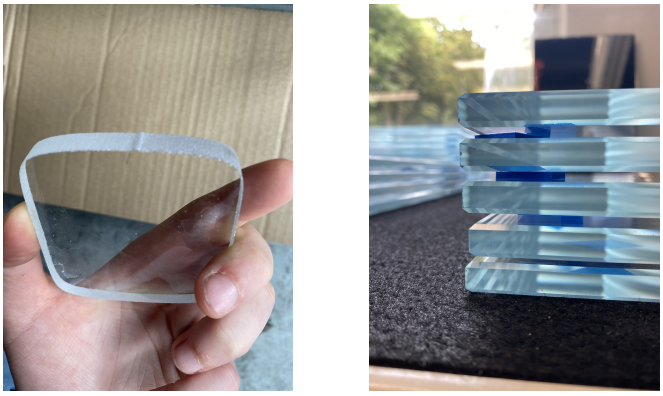

(a) (b)

Figure 7.9: Edge quality waterjet Kanawa sample (a) and polished Gooseneck sample (b)

When preparing the samples, it turned out that indeed, the tolerances of the milled samples were much tighter, which could be noticed because the interface material was much harder to fit into than with the waterjet samples. Also, the edges of the milled and polished samples were much smoother than those of the waterjet, resulting in better edge quality. When examining the samples, there were even large visible surface flaws on the edges, as can be seen in Figure 7.9(a). These edges had to be manually polished, in order to fit into the final geometry. Since the company waterjetting the glass was quite inexperienced with cutting glass, the machine was most likely not properly calibrated for glass. It was visible that some of the panes were not straight, but had a kerf angle.

PREPARATION ALUMINIUM AND STEEL PLATES

The aluminium plates were delivered in the right dimensions, and had the same width as the glass panels. Before gluing them, they had to be drilled, in order to place the bolt during the experiment. Everything was properly cleaned and then glued (see Figure 7.10(a)) using Araldite 2014-2, which has an average lap strength of 17 N/mm^2 when used with aluminium (see C.2.5). To ensure the aluminium plates were properly aligned and the bolt would fit, the bolt was already in place during the curing time of the glue, seen in Figure 7.10(b). The glue needed a minimum of 5 hours to cure, but it was cured

for over 60 hours before the samples were tested.
Since steel is much harder to process with the tools available for this research, the bolt holes were already cut with the waterjet (Figure 7.10(c)). This minimized the chance of any misalignment. Unfortunately, the waterjet caused the steel to corrode lightly. This caused the bolts to no longer fit, so the holes had to be filed. The calculations for the dimensions of the steel and aluminium elements can be found in Appendix A.2.



(a) (b) (c)

Figure 7.10: Gluing drilled aluminium plates with Araldite (a), aligning boltholes (b), waterjet steel plates (c)

CREATING TIMBER FRAMES

The prepared samples had to be properly aligned, transported and mounted easily, and stay in plane for safety. Therefore timber frames were built to support the samples, seen in Figure 7.11(a). By gluing the frames with timber of proper thickness, the panels were supported both on the glass and on the aluminium. Additionally, when the panels failed during testing, they could safely be lifted and removed by holding the timber sides instead of the glass.

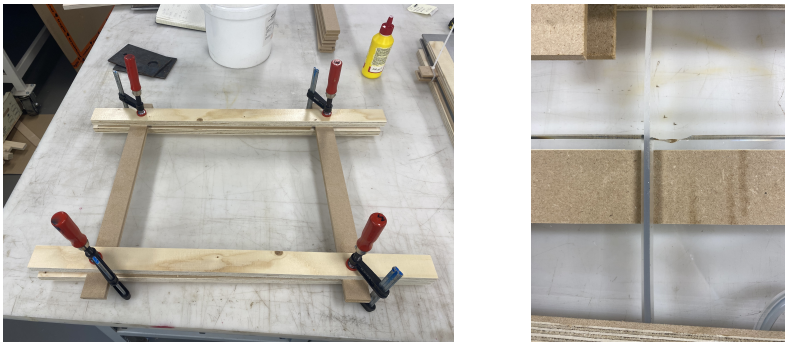

(a) (b)

Figure 7.11: Creating timber frames (a) and checking for visible damage (b)

CHECKING SAMPLES

Before mounting the samples, all were visually inspected for any scratches and misalignment of the interface material, like the chipped edge in Figure 7.11(b). Both damages and misalignment could have an effect on the location of failure and on the maximum capacity of the joint. The thickness of all Gooseneck samples was measured and confirmed to be 10 mm and the Kanawa samples were 9.8 mm thick.

POLARIZING FILTERS

In the setup seen in Figure 7.12(a), a double polarizing filter was used: one that could be observed with the naked eye and one that could be recorded with the camera for higher quality images. Behind the setup, a transparent perspex safety screen was placed with a white protection foil on it. On the inside, the first polarizing filter was placed at the right location to be aligned with the area of interest of the sample. In front of the setup, another perspex safety screen was placed, this time without the white foil. On the left half of the screen another polarizing filter was placed, making the photo-elastic effect visible to the naked eye. This is visualized in Figure 7.12(b). On the right, a camera with a polarizing filter on the lens was placed on a tripod, documenting the other half of the sample. In this case, the filter on the camera replaced the first polaroid filter in front of the camera.
For proper polarization, diffuse light from one direction is desired. A flat circular LED lamp was placed behind the safety screen. The white foil ensured a more diffuse distribution of the light on the sample, seen in the back of Figure 7.12(b).

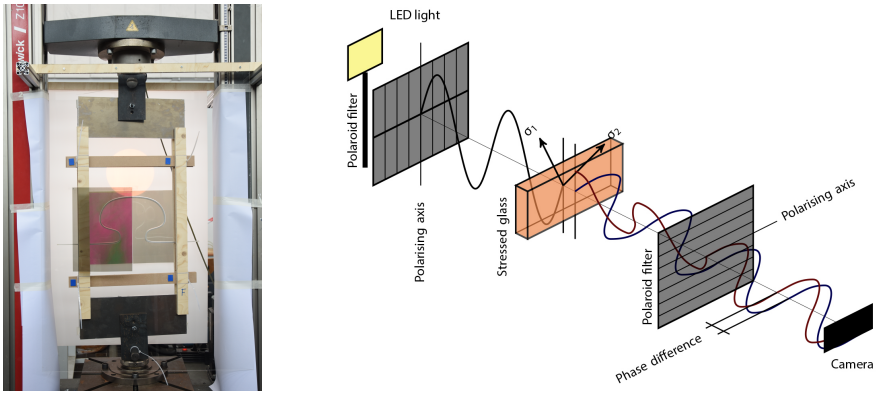

(a) (b)

Figure 7.12: Picture of front view polarizing filters (a) and schematization of polarization setup (b), adapted from Aurik, 2017

On another occasion, the Gooseneck samples were assembled into the Zwick. However, it turned out a misalignment had occurred during the drying process of the Araldite, because shorter bolts were used in this setup. There is a slight tapering of these bolts at the

end, right at the intersection with the aluminium plates. This created some space for the aluminium plates to slide. This process resulted in the fact that some of the bolts did not fit. This caused one of the samples to fail during the mounting. This was solved using M10 bolts instead of M12 bolts. Is it important to note however, that this solution caused a minor eccentricity and therefore an internal moment. This causes other stresses to develop than pure tensile stresses.

7.2.2. RESULTS

DUMMY SAMPLES

Since it was yet uncertain what would exactly happen during the experiment and if the expected displacement and forces from the FEA were indeed correct, two samples were tested as dummies. Only the force and displacement were measured as seen in 7.13(a). In these experiments, the force at failure was 3.4 kN and 3.2 kN with a displacement of 3.7 mm and 3.1 mm. As can be seen in 7.13(b) single clean crack was observed at the smallest section of the panel.

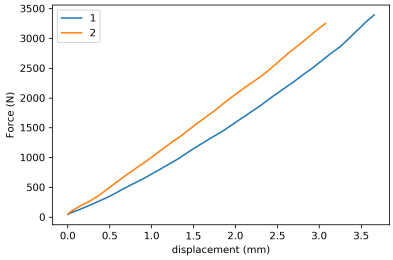

(a)



(b)

Figure 7.13: Plot of dummy 1 and 2 (a) and crack pattern of dummy sample 1 (b)

GOOSENECK SAMPLES

The samples were loaded similarly to the dummy samples, with a speed of 0.5 mm per minute. Quickly, it appeared that these samples were much stiffer and therefore a much higher resulting force was developing (7.14(a)). This caused the samples to fail with more energy and more explosive fractures. The tests turned out to be riskier due to small glass shards (7.14(b)).
Although the sample was symmetrically loaded, the female part failed first on the right side. It was decided to further load the sample until the left side would fail as well, displayed as A2 in 7.14(a). This time with a simple safety screen to prevent large flying glass shards.

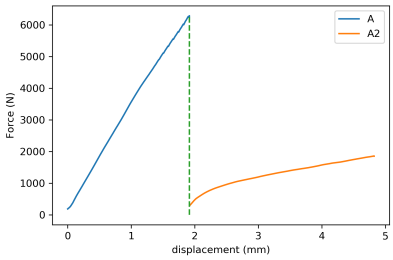

(a)



(b)

Figure 7.14: Plot of Gooseneck sample A (a) and image of corresponding sample after first failure (b)

After installing proper safety shields, the remaining 6 samples were tested until failure in a similar way. One of the objectives of the experiment was to validate the FEA model using the polarizing filter. In order to document the stress trajectories at a set force and displacement, it was then decided to hold the experiment every 0.5 mm. In 7.15 this can be observed in plots B, C, E and F by the small decrease in force at those intervals. Instead of simply holding the force and displacement, the force clearly drops when holding the displacement.
All input, relevant data and results from the tensile experiments are gathered in Table 7.2, including the standard deviation (SD) and variation coefficient. The failure in the Gooseneck samples was either on the right (R) or left (L) side from the observer's point of view. The stiffness is computed at 1.90 mm displacement, by taking δF between 1.85 mm and 1.90 mm displacement. This was divided by δd between those same values. It was purposely not done at 2 mm, since in the plots of the experiments that were executed with a hold, there is a distortion in the stiffness.

Label	Date	Hold	F (kN)	Displ. (mm)	$K_{1.90}$ (N/m)
A	12-09	No hold	6.29 (R)	1.96	3.28
B	16-09	Hold	5.99 (R)	1.95	2.60
C	16-09	Hold	6.58 (L+R)	2.21	3.18
D	12-09	-	-	-	-
E	16-09	Hold	6.13 (R)	2.00	2.95
F	16-09	Hold	6.35 (R)	2.11	2.75
G	12-09	No hold	5.11 (L)	2.14	2.93
H	16-09	No hold	5.51 (R)	1.81	3.13
Average	-	-	5.99	2.03	2.97
SD	-	-	0.477	0.126	0.225
Variation	-	-	7.96%	6.21%	7.58%

Table 7.2: Table with all input and results of Gooseneck samples

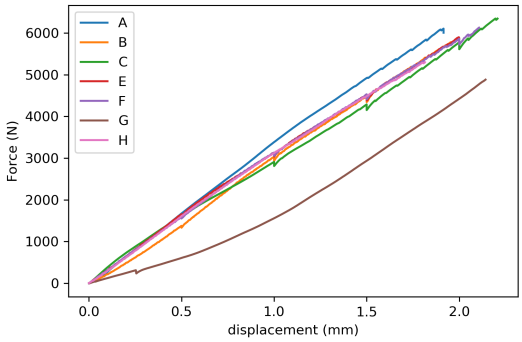

Figure 7.15: Plot of all Gooseneck samples

In the FEM the peak stresses were symmetrical for the Gooseneck model, so one would expect the sample to fail on both sides simultaneously. In reality, 6 out of the 7 samples tested, failed on only one side. Because the other side was still intact, there was still some post-failure capacity. To measure this capacity, the experiments were continued until also the other end failed. This continuation of the experiment can clearly be seen in Figure 7.14(a). After the first side fails, the force drops to zero. Then the geometry looks for a new point of contact. When it is steady, the force steadily builds up again until failure. The relevant data for these measurements after the first failure are collected in table 7.3

Label	Date	Hold	F (kN)	Displ. (mm)	Stiffness (N/m)
A2	12-09	No hold	1.86	5.31	0.64
C2	16-09	Hold	2.24	4.58	0.85
E2	16-09	Hold	1.78	5.21	0.55
F2	16-09	Hold	1.62	4.51	0.68
G2	12-09	No hold	1.93	6.75	0.42
H2	16-09	No hold	2.03	4.33	0.81
Average	-	-	1.91	5.12	0.66
SD	-	-	0.195	0.815	0.147
Variation	-	-	10.2%	15.9%	22.3%

Table 7.3: Table with all input and results of Gooseneck sample after first failure

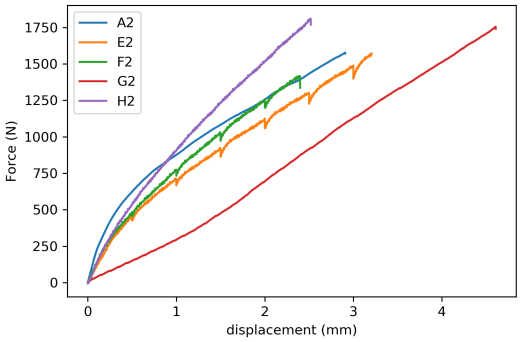

Figure 7.16: Plot of all Gooseneck samples after failure

In Figure 7.15 the plots of all experiments is shown. Striking is the similarity of the stiffness of the samples, except for sample G. They all seem to have a linear stiffness of around 3 N/m, while sample G does not behave linearly and also has a lower stiffness. Excluding outlier G from the sample set, gives an average failure strength of 6.14 kN instead of 5.99 kN. This results in a standard deviation of 0.337 and a variation coefficient of 5.49%.

In Figure 7.16 the plots of the data after failure are shown. Except for their somewhat parabolic shape, there seems to be very little relationship between the data. Once again sample G proves to be an exception. It is almost linear instead of parabolic, and is able to withstand a much larger displacement.

A summary of the two plots shown above is given in Figure 7.17. For the sake of clarity, all graphs showing post-fracture behaviour start at 2 mm displacement. In reality, these start at the displacement which caused the sample to fail initially.

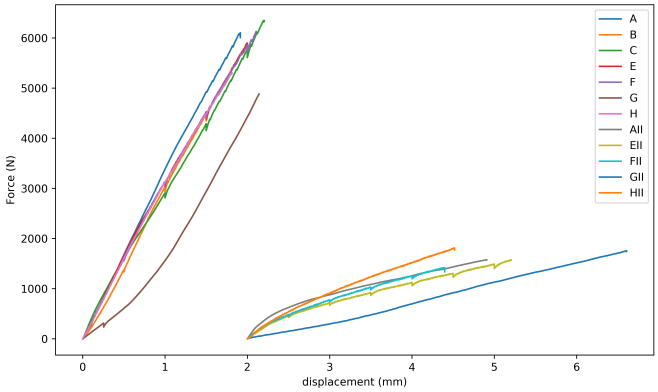

Figure 7.17: Plot of all Gooseneck samples before and after failure

KANAWA SAMPLES

Since the displacement from the Kanawa dummy samples was almost twice as large as the Gooseneck samples, it was decided to apply the displacement for the remaining Kanawa samples twice as fast. This means a displacement of 1 mm per minute. The hold was applied every 0.5 mm, resulting in a similar pattern in plot 7.18. All relevant data is collected in Table 7.4. As with the dummies, the samples failed at the smallest section. Because of the location of the failure, the joint could not take up any remaining strength in tension. No post-fracture behaviour was therefore recorded.

Label	Date	Hold	F (kN)	Displ. (mm)	$K_{1.90}$ (N/m)
Dum1	25-08	No hold	3.39 (R)	3.66	0.93
Dum2	25-08	No hold	3.25 (R)	3.08	1.1
1	16-09	Hold	4.20 (L)	3.50	1.2
2	16-09	Hold	4.09 (L)	3.76	1.1
3	16-09	Hold	4.35 (L)	4.00	1.1
4	16-09	Hold	4.54 (R)	4.24	1.1
5	16-09	Hold	4.16 (L)	3.99	1.0
7	16-09	Hold	4.61 (R)	3.87	1.2
8	16-09	Hold	4.40 (R)	4.00	1.1
Average	-	-	4.11	3.79	1.1
SD	-	-	0.453	0.324	0.0805
Variation	-	-	11.0%	8.55%	7.39%

Table 7.4: All relevant data for the Kanawa samples

Different from the Gooseneck samples, the plots from the samples in Figure 7.18 are not

linear.

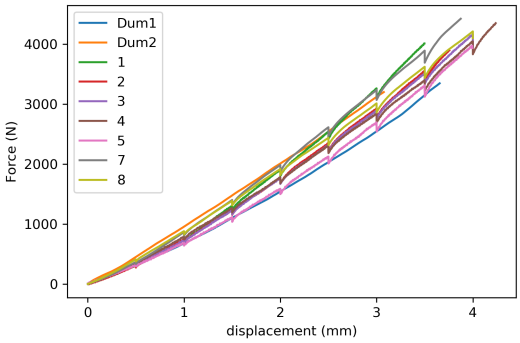

Figure 7.18: Plot of all Kanawa samples

7.2.3. COMPARISON FINITE ELEMENT ANALYSIS

GOOSENECK SAMPLES

One of the objectives of these experiments was to validate the finite element model. If we compare the results from the 7 experiments to the FEM, we can see that the stiffness of the experiments is comparable to the model, seen in Figure 7.19. That of the model is approximately 2.8 N/m. Of the experiments approximately 3.0 N/m. The model is therefore only 5.7% less stiff than the experiments show. If we consider sample G as an outlier, the average stiffness becomes 3.1 N/m. The model would then be 8.5% less stiff compared to the experiments.

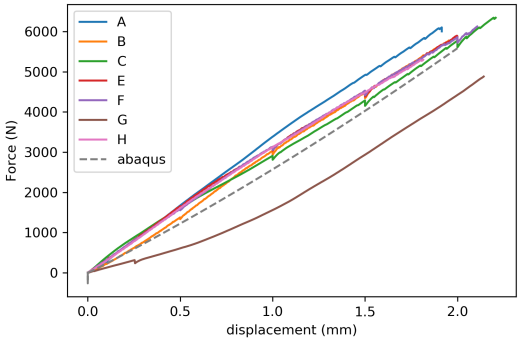

Figure 7.19: Plot of all Gooseneck samples and the FEM

If we compare the FEM with the experiments at a displacement (D) of 1 mm in Table 7.5,

we see quite similar stress trajectories. Peak stresses occur in the neck of the male part and at the point of contact in the female part. Interestingly, the stresses in the experiments seem to be concentrated at a lower point, instead of in the middle of the 'head' as can be seen in the model in Table 7.5. Additionally, more peak stresses seem to occur in the model at the neck, than in the model. Most striking is though, that the model predicts an in-plane principal stress of 150 N/mm^2. Statistically, such a value would most definitely cause the joint to fail, which is clearly not the case with the experiment. Annealed glass only has a design strength of around 45 N/mm^2.

If we look at the comparison of the FEM and experiment in Table 7.5 at 2 mm, the trajectories become even more comparable. Stresses move a bit more downward, and expand in a similar pattern. Peak stresses develop at the top of the neck in both the sample and the model. Also, the stress field expands upward in both images. An interesting difference is though, that in the experiment stresses develop at the edge of the panel, near the timber frame on the left. This cannot be seen in the FEM. The numerical values are even further from the design strength, stresses of over 300 N/mm^2 without failure of the glass are statistically quite unrealistic.

D	Experiment	Model	Comments
0.5		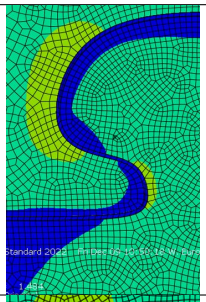	• Stiffness = 3.3 N/m • Peak stress = 73 N/mm^2 • F = 1.3 kN
1		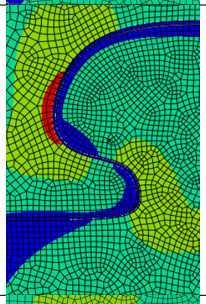	• Stiffness = 3.1 N/m • Peak stress = 150 N/mm^2 • F = 2.7 kN
1.5		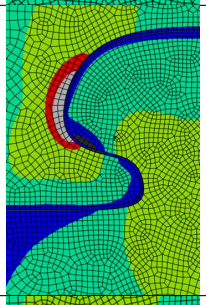	• Stiffness = 2.6 N/m • Peak stress = 220 N/mm^2 • F = 4.1 kN
2		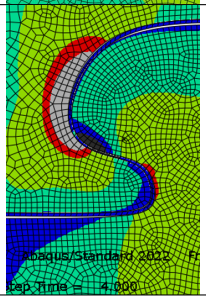	• Stiffness = 2.8 N/m • Peak stress = 300 N/mm^2 • F = 5.6 kN

Table 7.5: Comparison sample F to Abaqus model at multiple displacements

KANAWA SAMPLES

If we compare the stiffness of the 9 samples with the Abaqus model in Figure 7.20, we see that the sample is quite a bit stiffer than the model. The model has a stiffness of 0.73 N/m and the experiments of 1.1 N/m. This means that the model is 33% less stiff than the experiments. Another point of interest is the fact that the stiffness of both the model

and the samples is not linear.

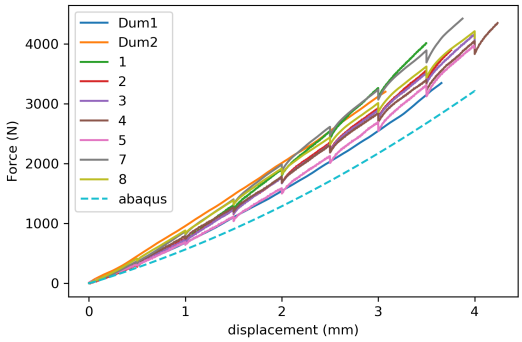

Figure 7.20: Plot of all Kanawa samples and the FEM

In Table 7.6 the comparison of the FEM and the model can be seen at 2 mm, which is halfway the total displacement of the model and sample. Especially in the square dowel in the middle, we see very similar patterns emerging due to the compression. Although in the sample the distributions are more similar to a diamond shape, while in the model they are more strongly oriented in one diagonal direction. An important difference can be noted between the peak stresses caused by the dowel. In the model, they are along the whole height, while in the sample they are concentrated in the top right corner. Unfortunately due to the size of the polarizing filters, the peak stresses at the top of the model cannot be validated.
Peak stresses at 2 mm displacement are around 60 N/mm^2, which is above design strength.

The Kanawa samples failed at around 4 mm displacement, hence it is compared to the model at this value in Table 7.6. One can observe that the peak stresses in the sample have expanded in a circular shape, similar to the model. In the samples there a peak stresses on the bottom right, like with the 2 mm displacement, but now additional peak stresses have developed at the bottom right.
The model gives an estimate of stresses of almost 150 N/mm^2, which would be far above the design strength for annealed glass.

D	Experiment	Model	Comments
1		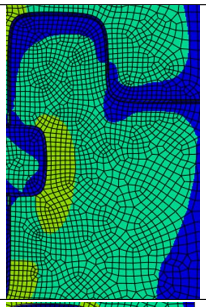	• Stiffness = 0.90 N/m • Peak stress = 27 N/mm^2 • F = 0.57 kN
2		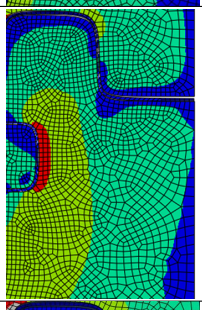	• Stiffness = 1.0 N/m • Peak stress = 60 N/mm^2 • F = 1.3 kN
3		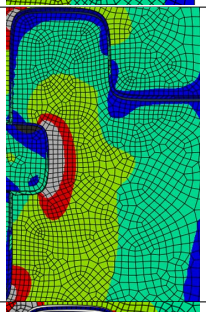	• Stiffness = 1.1 N/m • Peak stress = 100 N/mm^2 • F = 2.2 kN
4		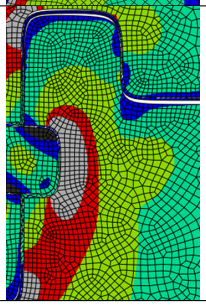	• Stiffness = 1.4 N/m • Peak stress = 150 N/mm^2 • F = 3.2 kN

Table 7.6: Comparison sample 8 to Abaqus model at multiple displacements

In Figure 7.21 the stiffness of both samples are compared, and it can be observed that the Gooseneck samples are almost 3 times as stiff.

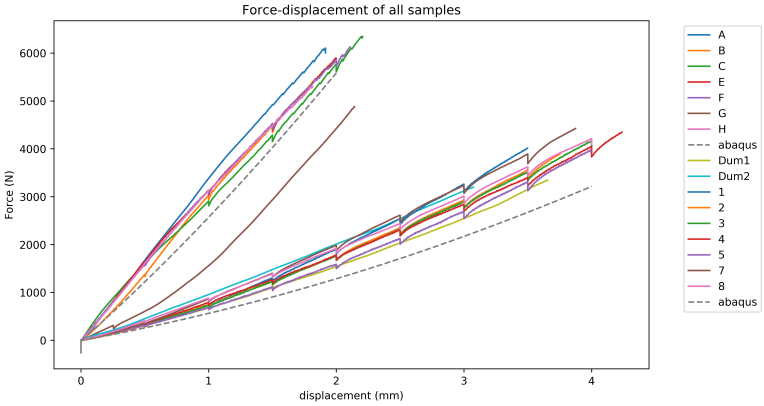

Figure 7.21: Plot of all Kanawa and Gooseneck samples

7.2.4. FAILURE MECHANISM

GOOSENECK SAMPLES

The shape of the failure was very similar in every sample. At the narrowest section in the female part, a small crack would occur at the point of contact with the interface material (the orange dot in Figure 7.22). This crack would then branch out into 3 to 5 additional cracks, depending on the amount of force and therefore energy stored in the sample. As can also be seen in Figure 7.22, often the energy was large enough to dislocate the glass shards.



Figure 7.22: Crack pattern Gooseneck samples with origin in orange

To find the critical flaw, some samples were further examined under the microscope. This was done on pieces which were located at the orange dot in Figure 7.22. The result can be seen in Figure 7.23. A clear distinction between the stable part of the fracture

(left corner of Figure 7.23(a)) and the unstable part of the fracture. In Figure 7.23(b) the typical mirror, mist and hackle can clearly be seen.

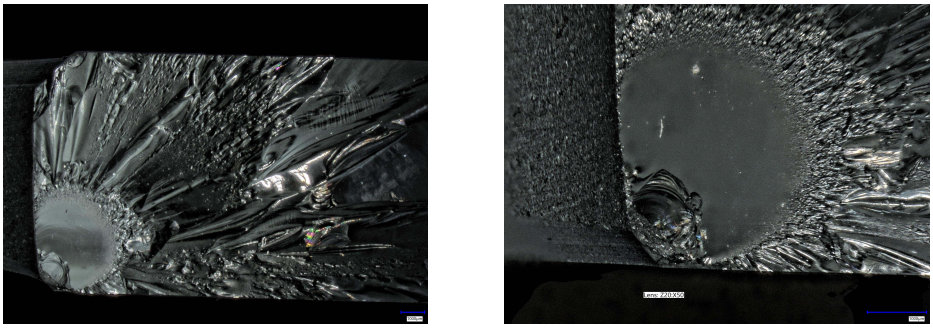

(a) (b)

Figure 7.23: Detail of critical failure from Gooseneck under microscope 20x zoom (a) and 50x zoom (b)

KANAWA SAMPLES

In tension, this joint fails brittle, since after failure, there is no force at all that can be taken up anymore.
The breaking pattern can be seen in Figure 7.24. Always a single crack originating from the corner marked with the orange dot. This was the narrowest section of the joint.

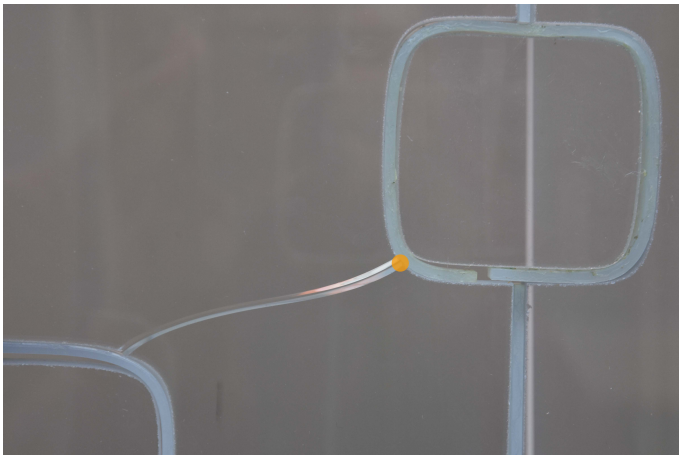

Figure 7.24: Crack pattern Kanawa samples with origin in orange

The Kanawa samples were also further examined under the microscope at the orange dot shown in Figure 7.24. As can be seen in the results in Figure 7.25, the typical mirror, mist and hackle are not visible. However, there was a flaw visible at the edge at 200x

zoom, shown in Figure 7.25(a). When zooming out, Wallner lines became visible, as seen in Figure 7.25(b).

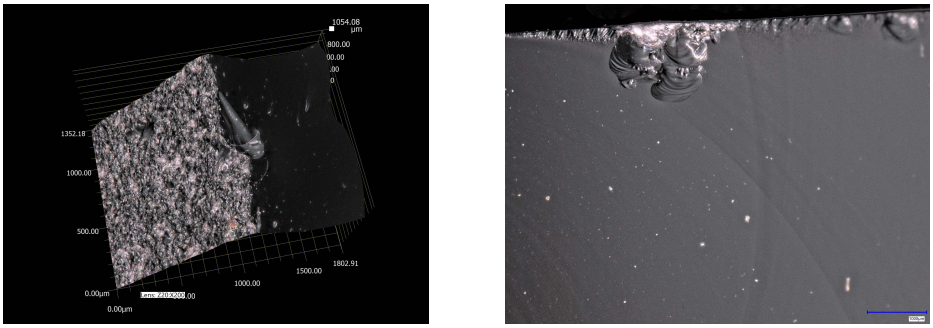

(a) (b)

Figure 7.25: Detail of critical failure from Gooseneck under microscope 200x zoom (a) and Wallner lines 50x zoom (b)

7.2.5. CONCLUSIONS AND RECOMMENDATIONS

Sample cutting

Depending on the goal and geometry of the samples, both waterjetting and milling can be suitable options for cutting the desired designs. Milling and polishing is the preferred option, since this will always be more accurate and the edge quality will be much better. However, instead of cutting the samples exactly to the thickness of the interface material (which is also more sensitive to variable thickness), it would be advisable to cut the gap approximately 0.25 mm to 0.5 mm wider. This will slightly decrease the stiffness of the joint, but prevent the necessity of any additional polishing and hammering. Both these options can cause damage to the glass which is of large influence on the strength of the glass panels. Also, the disadvantage of needing multiple panels will be less of a problem in reality. The joint will most likely be situated at the end of a glass element and therefore only a small piece of glass will be wasted. This piece could then be recycled.

In case the geometry requires waterjetting, it is highly advisable to find a company with extensive knowledge and experience in cutting glass. This will ensure the edges are straight (so with limited kerf angle), the tolerances are accurate and the edge quality is as high as possible. Because of the rough edges, the interface material will be even harder to slide in place, in case of accurate production. Therefore it is recommended to make the gap even wider than when milling the sample, so approximately 0.5 mm. This is also dependent on the surface of the interface material that will be applied.

Because the edges of the Gooseneck samples were polished, this meant the contact area was less than the full edge. Only the highest part of the edge was in contact with the other edge. This flat part of the edge was only 7 mm thick. This will have an influence on the stress distributions in the glass. It is recommended to incorporate this in the geometry

of the FEM for future research.

There were a lot of problems exporting the geometry in a suitable data file to be cut by the CNC machines. This was because the CNC software interpreted the closed polylines as separate lines. To prevent this, the DXF file had to be exported using the so called CAM Imperial scheme.

Interlayer application
Considerations and recommendations for interlayer choice can be found in Section 3.2, in this section only the used PU85 will be discussed.
The big advantage of PU85 is its flexibility, making it extremely easy to form it into any desired geometry. In the case of the Gooseneck sample, the material was squeezed in between the glass plates, after assembly. With the Kanawa sample, the interface material was put in place and then the glass plates were slid into place. The latter has a strong preference, since squeezing in between is an extremely fiddly job and poses a lot of risk of damaging the glass. For future research it is recommended to apply a material with sufficient sliding properties like PA6 or POM, otherwise the glass panels will still have to be forced and are equally at risk of damage. Also ensure the material is already in place before assembling the joint, instead of placing it after assembly.

Another point causing difficulty was ensuring the interface material was properly aligned with the glass panes. Because of the way the glass panes were glued to the aluminium, there was a height difference, causing the PU to 'fall through' the gap. A possible solution would be to first glue the interface material with light glue, and then join the pieces together. This would ensure the interlayer stays properly aligned and does not fall through, while still remaining a demountable system.

Preparation samples
The timber frames are crucial to the easy movement of the samples and an important safety measure after breakage. Additionally, they ensure the glass panes are properly aligned before placing them into the machine. It is strongly recommended to use similar frames for smaller samples during future research.
Using the waterjet to cut the steel plates was a quick solution to ensure the holes were cut at the right locations. However, it was quite an expensive solution. Additionally, the waterjet caused the cut surfaces to erode, making the holes too small for the bolts to fit through. A simple steel cutter, present at the Materials lab of the Faculty of 3mE should be sufficient. Then the steel plates can simply be ordered at the appropriate size, but will require some precise cutting.
gluing the aluminium panes to the glass with Araldite was a good solution and proved to never be the critical failure. A sufficiently long bolt is strongly recommended, to prevent any sliding during the curing process and keep the bolt holes aligned. Additionally, it is preferable to glue the samples before joining them together, since this makes the glass elements much easier to handle.
The Gooseneck sample was cut from larger panes, which seemed irrelevant. However, the Zwick has a maximum available height and the complete glass pane did not fit in

with the original design. This was solved by drilling the bolt holes closer to the edges of the aluminium and letting them overlap for a larger distance with the glass.

Conducting experiments
The first experiments were conducted using dummies, to simply acquire some first observations of what would happen in terms of failure patterns and order of magnitude of force and displacement. It is highly recommended to organize 1 or 2 additional samples for this purpose. However, these first runs should not be trusted blindly, since in these experiments it turned out that the other designs built up twice as much force as the dummies.
For exactly this reason, it was expected safety screens would not be necessary. However, during further testing, the tests had to be aborted because of dangerous flying glass shards. Therefore installing a safety screen and wearing safety glasses are always recommended.

These safety screens were used to install the polarizing filters, to ensure they were at the relevant location for every experiment. Setting up the polarizing filters properly requires a large amount of trial and error. The filters have to be placed at a 90° angle with respect to each other. Furthermore, the light should be diffuse from only the backside. Preferably, no light should fall onto the filters from other directions. Unfortunately, at the Materials lab at the Faculty of 3mE there are large skylights and windows. As the sun became brighter, the images from the filters became less and less clear. Placing a black tent over the machine could pose a solution.
Related to the polarizing filters, glass proved to be quite a hard material to photograph properly. This was mainly due to its reflective and transparent properties. Practising well with the manual focus of the camera used, solved most issues.

In these experiments, no numerical values were collected. For future research, it would be interesting to apply strain gauges or a DIC system. This way numerical values could also be compared to the FEM.

Results
For the Gooseneck samples, it can be concluded that the force-displacement plot and therefore stiffness is very similar to that of the Abaqus model. The stress trajectories are similar both at 1 mm and 2 mm displacement. However, the numerical values for the stresses seem to be very far off. There is one outlier G, which is significantly less stiff at the beginning of the experiments. One explanation could be that the sample was polished more extensively than the others. This additional space, would require less force to accomplish the small displacements at the start.

For the Kanawa samples, the results from the experiments and the FEM differ quite strongly. Interestingly, both behave slightly parabolic. Nonetheless, the experiments turned out to be far stiffer than the FEM. Additionally, the stress trajectories at 2 mm and 4 mm displacement vary from the model. The main difference is that the samples appear to have more concentrated peak stresses than the model. This could be explained

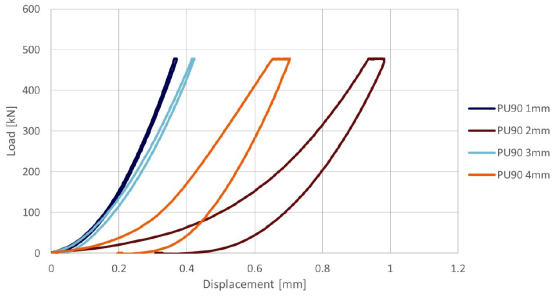

Figure 7.26: Force displacement plot of PU90

by the tolerances in the sample due to the inaccuracy of the waterjet. The rotation of the dowel causes the area of contact to strongly decrease, therefore increasing the stresses.
Numerical values, as with the Gooseneck sample, are quite far off the design strength. None of the samples already failed at this stage. This could be explained by an unreliable model, but also because the design strength is only a statistical value. There is only a small area under such high stresses, so the chance of a critical flaw being present in this area is also not very large.
In order to better explain this numerical difference, on top of the recommendation above, would be to extend the FEM. Currently, no hyperelasticity of the interlayer is modelled, which would definitely be of influence on the models. Also, it would be interesting to model the larger tolerances of the Kanawa model, by making the gap between the panels 0.5-1.0 mm wider, but keeping the thickness of the interlayer as is. This would definitely result in a less stiff geometry, and might even show the increased peak stresses observed during the experiments. This would, however, strongly complicate the model, because not all elements would geometrically touch each other.

When applying a hold during the experiments, meaning the displacement would be held at the exact same point, the resulting force would actually decrease. After reimposing a displacement, the force would not increase linearly. This same phenomenon was observed by Aurik, 2017 and is shown in Figure 7.26.
When comparing the Gooseneck to the Kanawa models and samples, we observe the Gooseneck design is almost 3 times as stiff. Since the stiffness of the models is relatively close to that of the samples, this cannot be fully attributed to execution. For example, that the tolerances of the Kanawa samples were much larger than that of the Gooseneck samples. It also means that the geometry of the Gooseneck joint itself is much stiffer than that of the Kanawa joint. However, these models only look at these designs in tension. It is more relevant how they behave under a bending moment, since this would be its practical use. Due to the geometry of the Kanawa sample, it will behave completely differently under a bending moment as can be seen in Section 5. The experiments to show this are described below.

Failure mechanism
As can be observed in Table 7.2, the majority of the Gooseneck samples fail on the right side. Based on the model, one would expect the model to fail on the right half of the experiments and on the left during the other half. This implies there might have been a slight eccentricity in the samples, causing the stresses to be higher on the right side. One explanation could be that all aluminium plates were drilled with the same setup, which could be off a couple of millimeters. Another option would be that the width of the aluminium plates was not always the same as the glass panels, making it harder to align them perfectly in the middle. This is because the aluminium plates were not neatly sized and some of the glass plates were bigger than the 400 standard sample size.
Interestingly, since the majority only fails on one side, the joint does not fail brittle. A part of the forces can still be taken up by the other half of the joint, preventing full collapse. However, this post-fracture strength is quite limited. It is important to realize that the joint would behave quite differently in practice. The joint would most likely fail at an imposed force due to loading. When the first side fails, the force would still be present, causing the other half to fail very soon after the first failure. The reason this post-fracture strength is present is probably only because the tests were displacement controlled. This means the force dropped to 0 after the first failure. If the experiments would have been force controlled, the other side would have failed almost directly after the first failure.

As can be seen in Table 7.4 the Kanawa samples failed quite equally on the right and left sides. This implies that misalignment was not as much present. One of the explanations could be that due to the geometry, the sample would start rotating at a certain point anyway. The influence of any misalignment would then be much smaller.
The reason these samples have such a clean crack, different from the multiple cracks as seen in Figure 7.22 lies within the embodied energy. Because the Kanawa samples all failed at a much lower force, the energy was therefore also lower. One of the reasons for this was the rotation of the dowel. This caused the forces to no longer be transferred over the entire edge, but only at a much smaller surface, causing higher peak stresses. Therefore failing at a relatively lower force.

The origin of the critical flaw of the Kanawa samples could not be easily determined, because the typical mirror, mist and hackle pattern was not visible. However, Wallner lines were visible. These show the direction of fracture, which is indeed at the orange dot shown in Figure 7.24.

Recommended design alterations
For the Gooseneck it would be interesting to decrease the width of the chin as seen in Figure 6.7(a). Using this design, the section of the female element will increase, minimizing normal stresses. This might move the critical point from the female element, to the neck of the male element.
For the Kanawa design, it might be interesting to make the dowel round instead of square shaped. Also decreasing the dowel size would increase the width of the critical section under pure tension. This would also likely decrease stresses due to the eccentricity and therefore increase the strength of the joint.

7.3. BENDING TESTS

Based on their performance under tension, an estimate can be made of the performance of the Gooseneck sample under a bending moment. Its behaviour under bending would be more similar to its actual application in a construction. However, since the Kanawa joint will behave as a very different mechanism than in tension, such a prediction cannot be made. It was therefore decided to test the Kanawa joint as a full scale beam under bending, analyzing its behaviour and determining the stiffness of the joint.
The most suitable and common way to test this, is by using a four point bending test. With this setup (7.27), bending stresses (which are critical to the failure of glass) will be maximum in between the forces applied. Because of the size of the samples, these tests were performed at the Stevinlab at the Faculty of Civil Engineering and Geosciences.

7.3.1. DESCRIPTION SETUP

A 2.4 meter long, 0.4 meter high and 10 mm thick beam was used and supported by two hinges at a distance of 2.3 meter. In reality, all glass panels were 9.8 mm thick. The supports are 10 x 10 cm and fully hinged. They also support the beam out of plane. The forces were applied at half the distance of the total length, so 1.2 m. This is a standard setup for the four point bending test. To prevent lateral torsional buckling, the beam was additionally supported sideways by two clamps at a distance of 0.8 meters.
There were three main points that required extra attention. Because of the slenderness of the beam (10x400 mm), it was difficult to ensure the beam was loaded properly in plane. Additionally, the whole beam would be too large (2400 mm) and heavy (24 kg) to place into the setup manually. Lastly, the setup had to be assembled and disassembled quickly, to limit the time required to perform the tests.
It was decided to slide the beam into the setup as two separate parts, and then join the elements while in the setup. The process of setting up the samples was as follows.

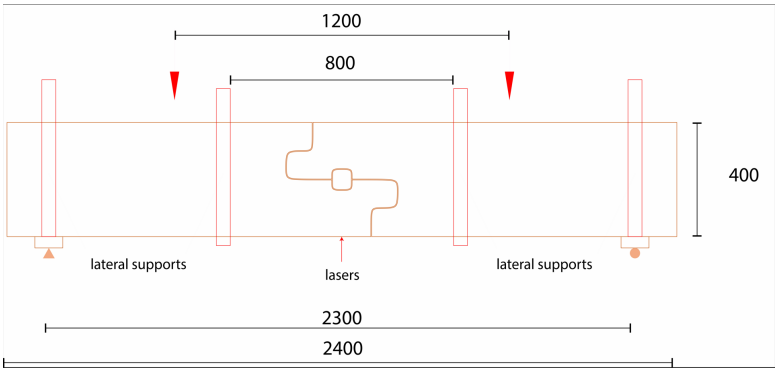

Figure 7.27: Dimensions (mm) setup bending test

ALIGNING MACHINE

The machine used for these experiments was originally built for timber bending tests. These elements are less slender and therefore less sensitive to lateral torsional buckling due to slight misalignment. Therefore extra measures were needed. First of all, the piston applying the force to the beam had to be clamped in the y-direction (7.28(a), since in its original state, could move freely in the x and y direction. A definition of global and sectional definitions can be found in Appendix D.1.
Additionally, when checking whether the piston was actually in the middle of the x-axis, it turned out there was an offset of more than 1 cm. This was checked by drawing a line in the middle of the bottom beam and hanging a weighted chord from the piston. This weight did not land on the line, but clearly next to it (7.28(b). The bottom beam was lifted and relocated until the weight and line aligned.



(a)

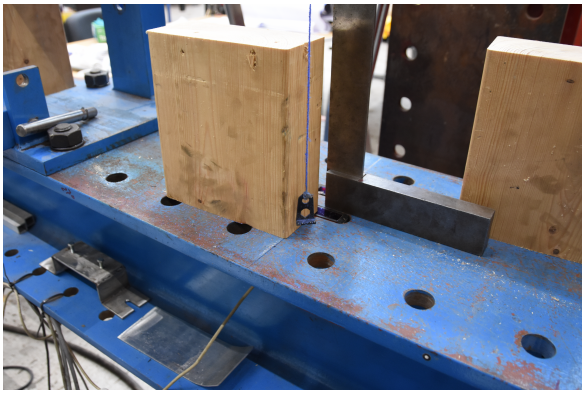

(b)

Figure 7.28: Alignment machine, piston clamped in y-direction (a) and misalignment in x-axis (b)

PREPARATION TIMBER FRAMES

As a solution to the sensitive points mentioned above, it was decided to place the glass beams in timber frames. These were placed perfectly vertically with the use of a level, to ensure all samples would be placed with the proper orientation, simply by sliding them between the frames. The middle part of the joint remained visible, so it could still be analyzed with the polarizing filter.
First, concrete plywood boards were cut the same size as each of the halves of the beam, minus the space necessary to view the middle part of the beam. At the location of the supports and the application of the forces, parts were cut out to ensure the force would be taken up by the glass only and not the timber frames. The plywood boards were then attached to simple timber beams, to ensure the height would be the same as the supports. Through these beams, thread was inserted and secured with nuts. These were later used to tighten the timber frames at the right distance, so the glass would fit. The

timber frames can be seen in 7.29(b). Then 10 mm PA6 was attached to both the supports and the force applications, to prevent peak stresses due to steel-glass contact, see 7.29(a).



(a) (b)

Figure 7.29: PA6 plated on supports (a) and concrete plywood with attached beams (b)

ASSEMBLY GLASS

The glass samples were placed between the plywood and the entire frame was assembled and tightened (7.30(a)). This way it was certain the glass plates would actually fit in between the frames. The glass plates were slid out and the frames were placed in the setup. Using the side supports from the supports and additional clamps, the frames were levelled and placed in the middle of the machine (7.30(b)).



(a) (b)

Figure 7.30: Setting distance glass (a) and levelling the frames with side supports (b)

Once the timber frames were in the right position and angle, they were tightly fastened in the clamps. Using rollers, each of the glass plates could then carefully be slid into the frames as seen in 7.31.



Figure 7.31: Placing the glass panel in the timber frame

With both panels in the middle, the interface material was placed between the glass panels. Previous to this, the interface material was sprayed with silicone spray to ensure easier sliding into place of the joint. Due to their weight and size, the glass panels could not simply be pushed into place. Additionally, there was a fear of forcing the glass under the wrong angle, causing it to break. Therefore, two timber beams were placed on each side, to keep the joint aligned in the middle. Then lashing straps were placed all the way around the beam. By carefully tightening the lashing straps, the joint was slid into its final position. Then to complete the joint and ensure it would stay in place, the final key piece with interface material around it was placed in the designated hole. Because the tolerance was quite big, the dowel could easily be placed after covering the interface material in silicone spray. Extra care was taken to ensure the dowel would be properly aligned with the rest of the beam.



(a) (b)

Figure 7.32: Putting the joint in the right position with lashing straps (a) resulting in the final joint as designed (b)

PLACEMENT CAMERAS

As with the previous tensile tests, a translucent safety screen was placed behind the setup, and a transparent screen was in front of it. In the current setup, the camera could only be placed very close to the joint. Due to the angle, the polarizing filters had to be attached to the beam itself, instead of the safety screens. The camera was placed on a wooden holder seen on the left of Figure 7.33(a). Below the beam, two lasers were mounted into the setup to measure the displacement, seen in Figure 7.33(b). However, the distance between them was too wide for the thickness of the glass beam. Therefore, a wider plastic plate was attached to the bottom of the beam which lasers could measure. This is the circle seen at the bottom of the beam in Figure 7.33(c).



(a) (b) (c)

Figure 7.33: Setup with camera (a), lasers at the bottom measuring displacement (b) and the glued disk attached to the bottom of the beam for the lasers to measure (c)

Three different cameras were used in this setup. The first and most important one was connected to the script of the machine. It can be seen on the left of Figure 7.33(a). Be-

cause a tripod would not fit between the machine and the sample, it was mounted onto the machine itself. The camera was manually focused on the bottom part of the sample, where tensile stresses would occur. It was programmed such that it would take a picture every 10 seconds, which was then linked to the displacement and force of the machine at that time. This way the stress distributions could be compared to the finite element model. Since the first camera could only record part of the joint, a GoPro was placed next to it. This camera was able to capture the whole joint in a time-lapse. The third camera was used to document existing damages, striking points and the failure mechanism of the sample.

The speed of the displacement was set to 0.5 mm per minute, similar to the tensile tests. Stress trajectories, force, displacement of the piston, and displacement at the bottom of the beam were recorded.

7.3.2. RESULTS

Just as with the tensile tests, it was uncertain what would be the final force on the samples at failure. Additionally, the light was very different at the Faculty of Civil Engineering than at 3mE, so setting up the polarizing filters required some trial and error. Two dummy samples were used for this purpose. Both samples followed a very striking pattern in the force-displacement plots, namely with varying stiffness and 2 platforms as can be seen in Figure 7.34(a). They failed at a force of 4.11 kN and 4.65 kN respectively, with a displacement of 2.5 mm and 2.7 mm. They both failed in the same place (see Figure 7.34(b)), where tensile stresses were expected to be highest according to the FEM.

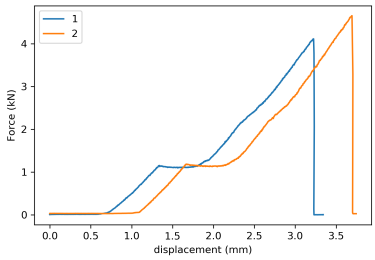

(a)

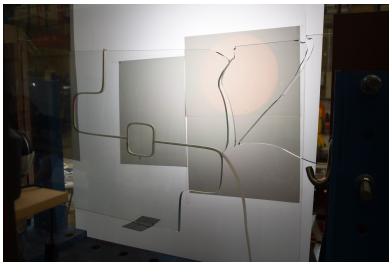

(b)

Figure 7.34: Plot and crack pattern of dummy samples

After testing the first two samples, the polarizing filter could be set up properly and the remaining 6 samples were tested and measured. Unfortunately, during the third experiment, the machine was wrongly activated. Because no safety mechanism is installed, the machine completely crushed the setup, including the timber frames. The measurements were not started automatically, so no data is available from this failure. Important to note is that only 5 full samples were available. Experiments 5-7 were performed using

unbroken elements from previous experiments. The elements used for each experiment are listed in Table 7.7. The force-displacement graphs of the successful experiments are displayed in Figure 7.35. It can clearly be seen that these samples also display similar platforms at approximately 0.7 mm and 1.7 mm.

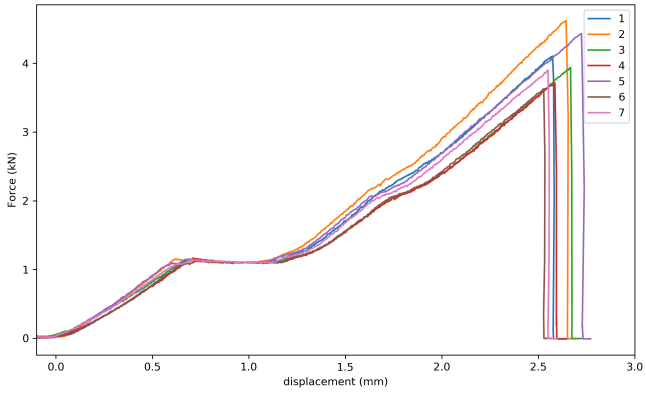

Figure 7.35: Force-displacement graph of all tested beams

Label	Date	El.	Force (kN)	Displ. (mm)	K_{max} (N/m)
1	07-10	1L+1R	4.11 (I)	2.5	2.35
2	07-10	2L+2R	4.65 (I)	2.7	2.62
No	10-10	L+R	-	-	-
3	10-10	3L+3R	3.94 (I)	2.8	2.30
4	10-10	4L+4R	3.74 (II)	2.4	2.41
5	12-10	3L+4R	4.35 (I)	2.8	2.39
6	12-10	3L+2R	3.57 (II)	2.6	2.26
7	12-10	1L+2R	3.87 (I)	2.6	2.47
Average	-	-	4.03	2.63	2.40
SD	-	-	0.343	0.139	0.111
Variation	-	-	8.51%	5.29%	4.63%

Table 7.7: All relevant data for the Kanawa bending tests

In Figure 7.36 the data recorded from the displacement recorder in the actuator is plotted together with the recorded displacement of the lasers below the beam. It appears that the lasers show stiffer behaviour than the actuator.

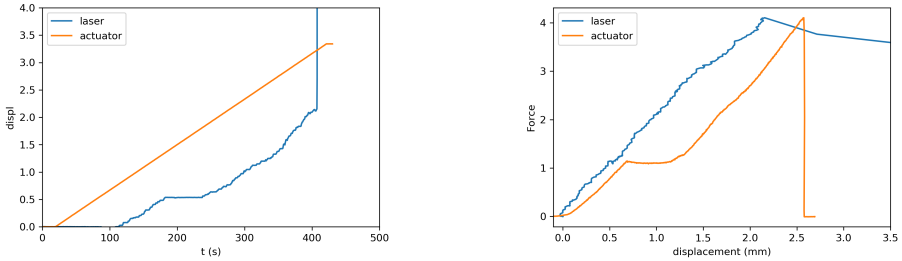

(a) (b)

Figure 7.36: Comparison of the displacement of the piston and the recorded displacement of the lasers over time (a) and force over displacement (b)

7.3.3. COMPARISON FEA

There is no denying that the FEM and the samples behave very differently as can be seen in Figure 7.37. First of all, the stiffness of the model is approximately 0.55 N/m and that of the sample is approximately 2.4 N/m. Secondly, and most striking is the variation of stiffness. Where the model gives a fixed stiffness, while the experiments show platforms where the stiffness is 0.

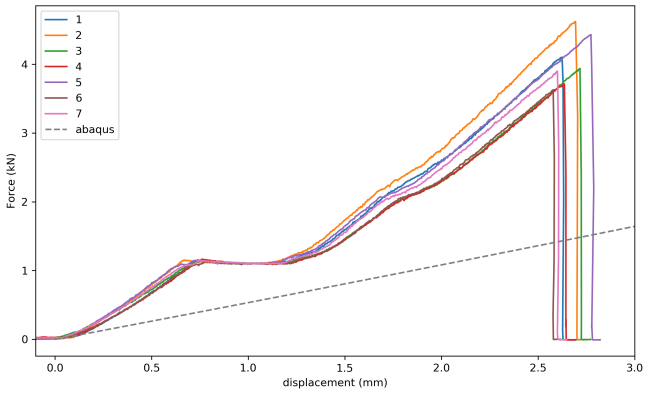

Figure 7.37: Force-displacement graph of all tested beams and Abaqus model

In Figure 7.8 the finite element model and sample 5 are compared at various displacements (D). At 1.5 mm displacement, both the sample and model show the highest peak stresses on the top right of the dowel and the furthest right of the bottom panel. Interestingly, no stresses seem to develop in the dowel during the experiments. Additionally, it seems much higher stresses are developed in the bottom panel during the experi-

ments than was expected from the model. Numerical values seem quite accurate for the stresses, since peak stresses are around 40 N/mm^2. This is a magnitude at which it is statistically not likely the samples will fail, also see Figure 3.7.

The model and sample 5 are compared near failure at 2.7 mm displacement. It is clear that the areas under stress expand in both figures and peak stresses increase as well. Numerically, peak stresses start exceeding 120 N/mm^2, this is far above the design strength of annealed glass. It is statistically more likely that significant cracks are present, causing the glass to fail at lower stresses.
The numerical values considering the forces and displacements are also different between the experiments and the model. At this 2.7 mm displacement, the model predicts a necessary force of 1.5 kN. During experiment 5, this was 4.35 kN instead.

D	Experiment	Model	Comments
0.5	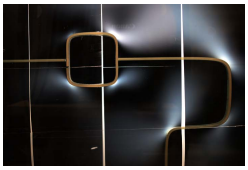	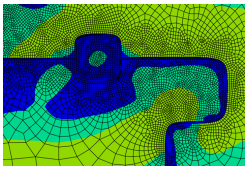	• Stiffness = 2.2 N/m • Peak stress = 24 N/mm^2 • F = 0.27 kN
1	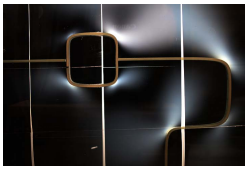	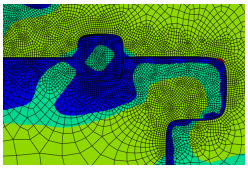	• Stiffness = 0 N/m • Peak stress = 46 N/mm^2 • F = 0.54 kN
1.5	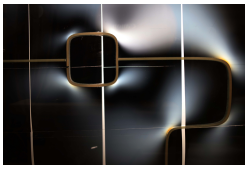	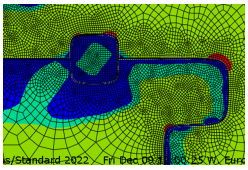	• Stiffness = 2.4 N/m • Peak stress = 69 N/mm^2 • F = 0.81 kN
2	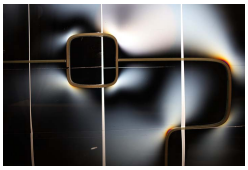	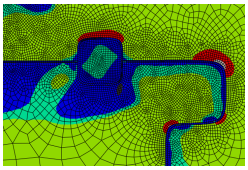	• Stiffness = 2.3 N/m • Peak stress = 95 N/mm^2 • F = 1.1 kN
2.5	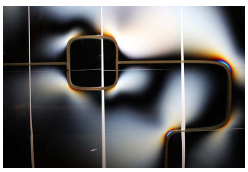	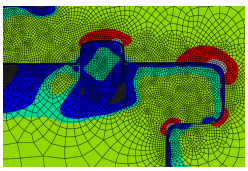	• Stiffness = 2.4 N/m • Peak stress = 120 N/mm^2 • F = 1.4 kN
2.7	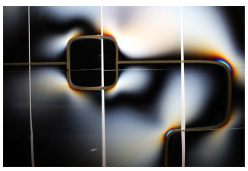	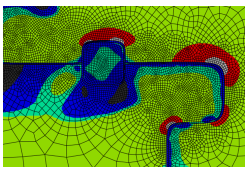	• Stiffness = 2.4 N/m • Peak stress = 130 N/mm^2 • F = 1.5 kN

Table 7.8: Comparison sample 5 to Abaqus model at multiple displacements

7.3.4. FAILURE MECHANISM

As can be seen in Table 7.7, 5 out of 7 experiments failed in mode I, which can be seen in Figure 7.38(a). This was the expected dominant failure mode, since the origin of the crack is also the location with the largest area of peak stresses. The probability that an impurity would be present in this area, leading to the fatal crack, was most likely. Failure

mode II occurred in the lower part of the joint. At this point, peak stresses are also large, with an additional risk due to the relatively small section. Failure mode I is brittle, while mode II has some post breakage capacity. In theory, F_2 and F_5 from Figure 5.15 are lost, and only F_1 and F_3 take up the bending moment. This was examined in one experiment, seen in Figure 7.39. The experiment could not be continued until failure, because the bottom of the glass beam was about to touch the bottom of the machine. It is clear that still a lot of movement is possible without failure, but the capacity force-wise is very limited.



(a) (b)

Figure 7.38: Failure mode I in el. 4R (a) and II in el. 3L (b) with the origin of the crack in orange

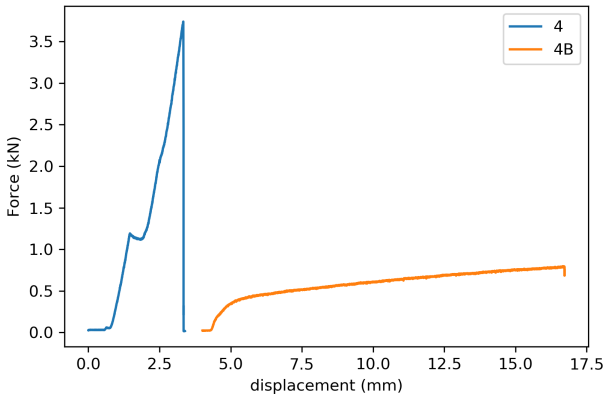

Figure 7.39: Force-displacement graph of sample 4 plus post-failure behaviour

Sample 4R was inspected under the microscope, to find the origin of the cracks at the orange dot in Figure 7.38(a). The results can be seen in Figure 7.40. From these images, it can be seen that there is indeed an impurity present at the edge, which led to the cracking of the element. This can be seen by the typical mirror, mist and hackle pattern. In

Figure 7.40(a) the waterjet edge can also be seen in more detail. It becomes clear how rough this edge actually is. This results in the pattern in Figure 7.38(a), where the crack branches off to 3 to 4 cracks.

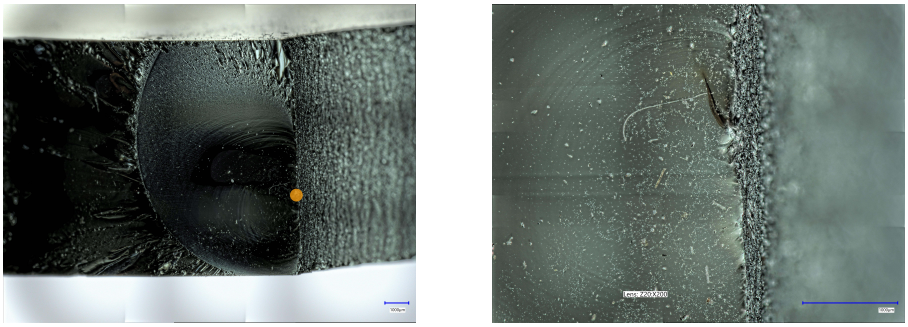

(a) (b)

Figure 7.40: Origin crack el. 4R 50x (a) and 200x (b)

7.3.5. STIFFNESS JOINT

The objective of this research is to design a rigid joint.

$$u_{total} = u_{beam} + u_{spring} \tag{7.1}$$

The average total deflection at the bottom is 1.99 mm at a force of 4.0 kN. This deflection can be described using differential equations, for which the procedure can be found in Appendix D.3. The theoretical deflection of a beam would be:

$$I = \frac{b \cdot h^3}{12} = \frac{10 \cdot 400^3}{12} = 5.3 \cdot 10^7 \text{mm}^4 \tag{7.2}$$

$$-\frac{aFx^2}{2EI} + \frac{aF(a+b)x}{EI} - \frac{a^3F}{6EI} \tag{7.3}$$

In this case, a is the distance from the support to the force, and b the distance from the force to the middle of the beam. In the case of the experiments, the theoretical deflection would be.

$$-\frac{550 \cdot 2050 \cdot 1150^2}{2 \cdot 70000 \cdot 5.3 \cdot 10^7} + \frac{550 \cdot 2050(550+600)1150}{70000 \cdot 5.3 \cdot 10^7} - \frac{550^3 2050}{6 \cdot 70000 \cdot 5.3 \cdot 10^7} = 0.18 \text{ mm} \tag{7.4}$$

This means the additional deflection due to the joint is

$$u_{spring} = 1.99 - 0.18 = 1.8 \text{ mm} \tag{7.5}$$

$$r_{spring} = \frac{M}{\phi} = \frac{1.1}{0.0018} = 611 \text{ kNm/rad} \tag{7.6}$$

$$M = 550 \cdot 2000 = 1.1 \text{ kNm} \tag{7.7}$$

$$\phi = \frac{u}{L} = \frac{1.99}{1.1} = 0.0018 \text{ rad} \tag{7.8}$$

Following the same procedure, a rigid beam would have a stiffness of 6722 kNm/rad, so more than 10 times stiffer. Differently said, the tested joint has 9.1% of the stiffness compared to a solid beam.

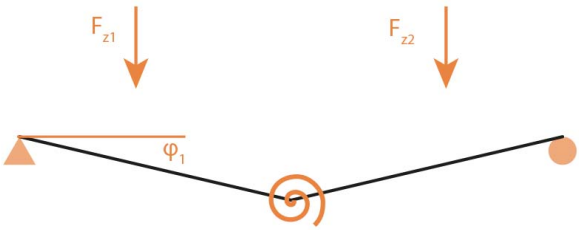

Figure 7.41: Schematization rotational spring joint under four point bending

7.3.6. CONCLUSIONS AND RECOMMENDATIONS

General setup

In the experiments described above, a 2.4 meter long beam was analyzed using a 4-point bending test. Due to its slenderness, it was necessary to clamp it at multiple locations to prevent lateral torsional buckling and ensure it was loaded properly in plane. Timber frames supported the beam at the outer ends of the beam. Unfortunately, as the results from the lasers show in Figure 7.42 the beam still slightly rotated. This implies that lateral torsional buckling of the whole beam occurred, or the joint slid out of place out of plane.

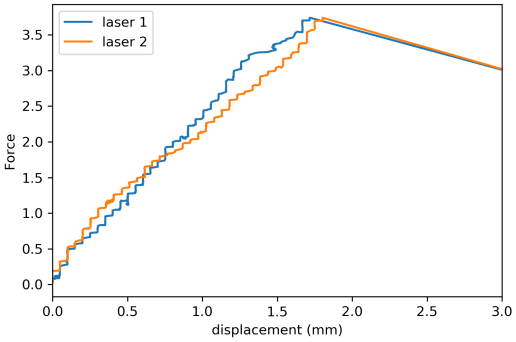

Figure 7.42: Force displacement graph of the lasers from experiment 4

The distance between the supports was required to record the results from the polarizing filter, and can therefore not be minimized. Perhaps a system using transparent perspex screens could provide a solution. These could be placed over the length of the beam that is not covered by the timber frames. This prevents the movement of the joint out of plane. However, this would require extra attention to not distort the polarizing patterns from the glass.

Aligning machine

For these experiments a setup which is usually used for timber was available. This caused quite some misalignment and also the load cell seemed to be too large. Because of this the results turned out to be less accurate. For future research, it would be desired to have a more accurate load cell and alignment of the machine. Additionally, to ensure loading in the proper direction, the clamps had to be aligned manually. This was very labour intensive and resulted in a not so perfect alignment. Using clamps which are already levelled over both the height and length of the beam would be recommended.

Preparation timber frames

It was decided to slide the beam into the setup as two separate parts, and then join the elements while in the setup. This proved to be a good solution, since the weight of half a beam was easy to mount and enabled sufficient assembly speed. The frames were made

of concrete plywood, which was a very good solution due to its excellent sliding properties. Extra care should be taken to sand the surfaces after drilling holes in the plywood for the bolts, which should also be completely be sunken in. Otherwise, the frames will cause scratching on the surface of the glass. Because of the small displacements, chances are the friction between the glass and concrete plywood was significant in the stiffness of the setup.

The PA6 was not properly attached to the supports, causing it to slightly slide off during the experiments. A stronger non-permanent connection should be used.

To easily assemble the beam, the interlayer material was sprayed with silicone spray and the glass was then pushed into place using lashing straps. This was definitely an efficient way to assemble the beam without the risk of damage. However, it should be taken into account that the spray influences the friction between the glass and interface material. This influences the behaviour of the joint as a whole, as can be seen in the sensitivity analysis in Figure 6.14. When placing the dowel, there was a risk of pushing it through the joint, causing it to fall out on the other side. Also, the combination with the PU85 made it a very fidgety process. It might be a good solution to make the dowel and interface material as one solid element. This has less risk of damage during assembly, and makes it easier. An additional advantage could be that even less sliding occurs within the joint, because there is only one sliding surface between the glass and interlayer, instead of 2. This would most likely result in a stiffer joint.

Placement cameras

Due to the buildup of the machine, it was not possible to place a camera at a sufficient distance from the joint and have a proper angle. This meant the camera had to be placed very close to the sample, influencing how the polarizing filters were visible on the joint. The polarizing filters had to be attached to the beam itself, which caused the filters to often damage after the breaking of the beam. It was also a very time-consuming process. It is highly recommended to arrange larger polarizing filters, so they can be attached to the safety screens behind and in front of the sample and not get damaged. A program was written that took a picture of the setup every 10 seconds, which was then linked to the data recorded. This made it very easy to compare data to the stress distributions seen. Unfortunately, this camera could only record half of the beam due to its location.

The lasers at the bottom were set up too wide for the thickness of the beam, therefore a plastic plate was stuck to the bottom of the sample. This worked quite well, and it also enabled the visualisation of LTB. The disadvantage was that the glue prevented deformations locally. Due to the small global deformations, this effect is probably insignificant.

Extra cameras were used to take pictures of the failure patterns and any striking occurrences during the experiments. Additionally, a GoPro camera was used to record the behaviour of the whole joint. This camera is smaller and therefore has a wider angle than the camera linked to the setup. Its quality is also much worse than that of the setup camera. It is therefore recommended to use a similar setup with multiple cameras.

Results

When conducting the experiments, two things went very differently than expected. First of all, the polarizing filters did not work at all with the previously used setup from the tensile tests. This probably had to do with the different lighting in the lab. Only in the third experiment, it was achieved to create a setup in which the polarizing filters would provide relevant information. It is therefore recommended to properly experiment with the filters in the lighting circumstances where the experiments will take place. In the case of the Stevinlab, the foil covering the filters on both sides had to be taken off and the filters rotated 90° relative to each other. This created the typical black image seen in Table 7.8. The light comes through the locations of the stresses.

Secondly, there was a very striking pattern visible in the force-displacement graph. There was no linear stiffness, as was expected based on the model, but a varying stiffness with plateaus of stiffness 0. There are several hypotheses of the cause for this difference. Namely, the slip between the glass and interface material, changing point of contact or tolerances, sliding in the machine, linear elastic modelling, lateral torsional buckling and the yielding of the interface material. All six hypotheses will briefly be discussed below.

1. Slip between glass and interface material
   A certain friction is present between the interface material and the glass edge. In 6 the parameters chosen to model this behaviour are described. This is done with assumptions, but in reality, this friction modulus could be quite different. For example, the edge of the waterjet samples was rougher than expected or the interface material was covered in silicone spray, which strongly decreases friction. In theory, if the friction coefficient was much lower than modelled, this could mean that at certain points the glass would simply slip over the interface material, without really requiring much additional force. However, this hypothesis is not very likely, since this slip occurs at quite exactly the same moment during the experiments. One would expect this slipping phenomenon to occur more randomly. Lastly, the sensitivity analysis in Section 6 shows no such effects when decreasing the friction modulus in the Abaqus models.

2. Changing point of contact
   The displacement will always occur at the point with the least resistance. In the sample, there is a large difference in the stiffness of the interface material and the glass samples. It could therefore be that after a certain deformation (in this case about 0.7 mm) the separate pieces have moved in such a way that a new point of force transfer is established. Perhaps, at this point, the interface material is the only one compressed. Or even a mechanism occurs that requires little to no force to move, simply because the line of force turns into a specific scenario. After further rotation, a new point of contact might be established, where more resistance is present. This would result in the increase of stiffness again, seen so typically in Figure 7.37.

3. Tolerances or sliding in machine
   Since the force-displacement graph is so consistent in its shape, it could also be caused by something in the machine. For example, the supports are hinged, but have quite some resistance. So after approximately 1 kN force has been built up, this would be sufficient to make the supports rotate. This would cause the beam to further displace, without really requiring any additional force. The same pattern could occur in the force application or another moving part of the machine. In this case for example the actuator would simply slide over the beam, instead of compressing it.

4. Linear elastic modelling
   The Abaqus model, specifically the material PU85, was set up using linear elastic material properties. In reality, the interface material does not behave linear elastically, so this could cause the model to be off. However, it was already attempted to add nonlinear elastic properties to the material, giving the same result seen in the sensitivity analysis in Chapter 6, Figure 6.15.

5. Lateral torsional buckling
   The beam was tightly supported in lateral directions, to prevent lateral torsional buckling. Due to the slenderness of the beam, this risk was high. However, in the middle, the beam was not supported to keep the joint visible. Therefore this part was still vulnerable to LTB. The torsion of the beam due to LTB could be measured at the bottom of the beam using the lasers. As can be seen in Figure 7.42, there was indeed some LTB occurring. However, this would only make the beam less stiff than the model, not stiffer. So even though it is an occurring phenomenon, it is not likely to be the cause of the difference between the model and the experiments.

6. Yielding interface material
   In theory, if the yield strength of the interface would be reached, the material would further deform without requiring much to no additional stress and therefore strength. This would also mean the PU85 would be deformed beyond repair. It could be the cause of the first plateau. The Abaqus model showed compressive forces in the interlayer of 23 MPa, below 40 MPa, which would be the yield strength according to data provided by the producer.
   However looking at the PU85 after the experiments in Figure 7.43(a), it is clear plastic deformation has occurred. In the paper by Singh et al., 2019 even higher yield stresses of around 100 MPa are recorded. However, the shape of the stress-strain behaviour in Figure 7.43(b) seems to be quite similar to that of the experiments in Figure 7.37. It is quite likely that the stresses in the interface material are much higher than the model reports, and therefore yielding does occur in the beam.

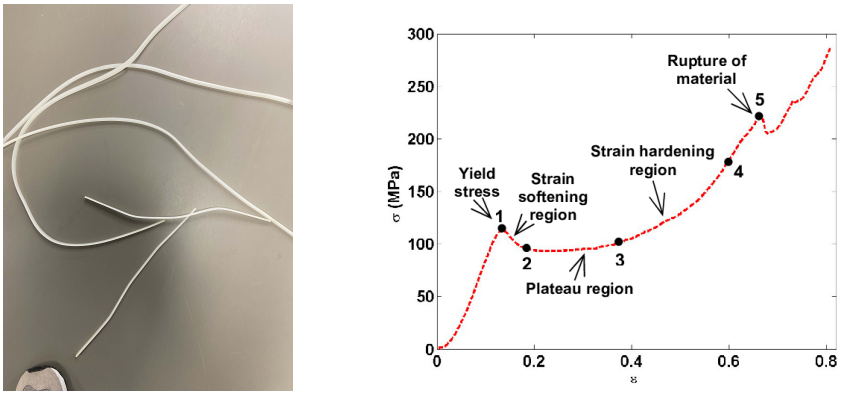

(a) (b)

Figure 7.43: Picture of deformed PU85 after the experiments (a) and stress-strain curve of PU under compression (b), (Singh et al., 2019)

Since the paper from Singh et al., 2019 showed a different stiffness up until yielding strength, it was attempted to calibrate the model up to this point. The results can be seen in Figure 7.44. The E-modulus of the interface material was increased even up to that of glass, but this only made the stiffness insignificantly higher. This means other factors are also involved, resulting in the shape of the force-displacement graph.

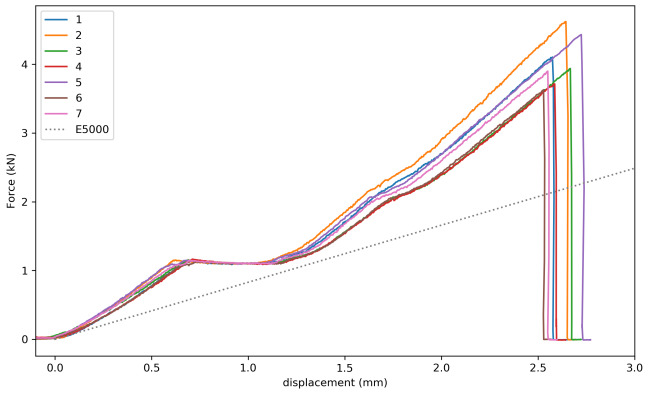

Figure 7.44: All samples 4 point bending including Abaqus model with a interlayer stiffness of 5000 MPa

First of all, there is another factor causing the increased stiffness at the start of the experiment, which simply cannot be calibrated with the model. One of the reasons for this increased stiffness could be the friction occurring between the concrete plywood panels and the glass. This friction is minimal, but due to the relatively small deformations,

could be of large influence.

Additionally, it is quite likely, that next to the yielding of the PU85, some sliding in the machine also occurs. This hypothesis is supported by the laser data seen in Figure 7.45. The lasers show linear behaviour, as expected from the model. In practice, this means that the actuator is moving, but the beam is not. Therefore, the movement must happen somewhere in the actuator.

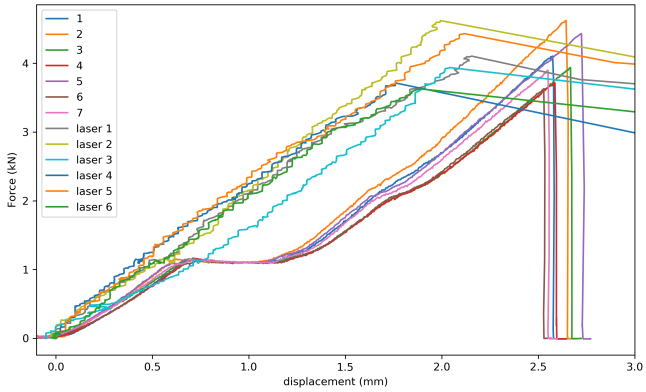

Figure 7.45: All samples 4 point bending including laser data

Another argument for this hypothesis is the comparison between the actuator and laser data over time. In Figure 7.46, it becomes clear that a little before 200 seconds, the actuator moves, but the lasers do not record any displacement.

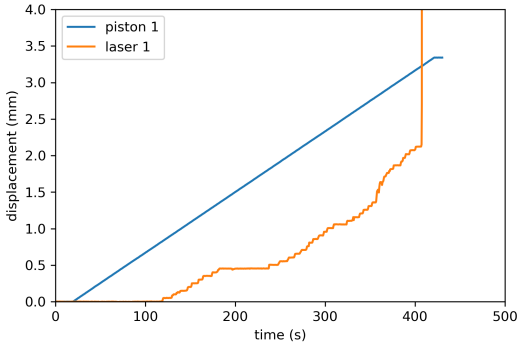

Figure 7.46: Displacement of the actuator and bottom of the beam over time

To test these hypotheses, it is recommended to repeat the experiments using timber dummies. These could be produced from for example MDF plates to have isotropic behaviour. No interface material should be used. The stiffness of these joints can then be compared to that of the glass samples. If it turns out to be a straight line, the geometry itself is not likely to be the cause.

To test whether the difference in initial stiffness indeed originates from the friction between the timber frames and glass, the boundary conditions in the model could be adapted. For example, the simply supported beam could be changed into a beam with a slight rotation stiffness at the supports. It is quite likely that using a combination of stiffer supports and a stiffer interlayer would approach the initial stiffness of the experiments.

The global pattern of the stress trajectories compared to the model is quite similar, especially close to failure. The experiments show very little difference between the displacement at 0.5 and 1.0 mm. This is quite similar to the model. But in the experiments, it is a valid result, because the stiffness between these two points is mostly 0. This means that there is no additional force and also stresses building up in the joint. However, a critical attitude is necessary on whether this comparison can really be made, since the stiffness of the model and the experiments behaves so differently. It would be wise to first calibrate the model to the experiments and then execute such an analysis again.

Failure mode
The samples failed at a force of around 4 kN with a displacement of 2.6 mm. There were 2 failure modes, as expected from the FEM. When examining the samples under the microscope. It seemed quite likely that this critical impurity was a result of the waterjet itself. It would be interesting to repeat the experiments with a better calibrated waterjet to see if this increases the strength of the joint.

The beam failed at an average moment of 1.1 kNm, with a displacement of 2.1 mm. This results in a rotational stiffness of 611 kNm/rad. This means the Kanawa beam joint has a stiffness of 9.1% compared to a solid glass beam under four point bending.

IV

Conclusions and recommendations

8

CONCLUSIONS AND RECOMMENDATIONS

The objective of this research is to show that it is possible to design a glass rigid connection using contact pressure as part of a portal frame, in order to promote the use of demountable connections in structural glass constructions. This will contribute to the knowledge of demountable connections, allowing for more circularity in the building industry, specifically glass.

8.1. SUBQUESTIONS

To help answer the main question, several subquestions were established. These will now be answered briefly below.

1. **What types of rigid glass connections exist and how do they work?**
   To join float glass panels rigidly, currently bolted, embedded and adhesive connections are used. The bolted and embedded joints provide a lot of possibilities for demountability, but are unfavourable because they cause peak stresses and are often not desired from an architectural point of view. Adhesive connections are great for equal stress distributions, but are very sensitive to environmental circumstances, and strongly decrease in strength over time. Currently, no efficient possibility exists to demount such a joint.

2. **What are relevant material properties of glass and suitable interlayers to properly interact with these properties?**
   Due to its structure, glass fails brittle when tensile stresses are applied to an existing micro crack in the material. It is not dependent on its inherent strength, but on

the crack already present on the surface. Therefore statistical methods are used to determine the design strength of 45 N/mm^2 for annealed and 70 N/mm^2 for heat-strengthened glass. Different post-processing methods have an influence on the edge quality and therefore structural performance of the Sashimono joint.
When joining glass panes, an interlayer is required to prevent peak stresses in the glass. This interlayer should have a sufficient thickness and should not be too stiff. Promising interlayers based on earlier research are Surlyn, PVC, PA6, POM and PU. For this research, these interlayers were examined. The selection criteria are: availability in a thickness of 3 mm, the ability to shape the material into the desired geometry, stiffness of 70 GPa or max 120 MPa, compressive strength of 20-25 MPa, sufficient creep resistance and a tear strength of minimum 34 MPa. Additionally, transparency, durability, pricing, availability and manageability are considered. Because the primary purpose of this interlayer is to be able to perform the experiments in this research, the mechanical properties are considered the most important. Due to pricing and availability PVC, PA6, POM and PU85 were ordered and used in section 7.1. These are expected to be suitable interlayers to interact with the material properties of glass.

3. **Which types of relevant Sashimono joints exist and which would be suitable to execute in glass?**
Traditional Sashimono joints are suitable for transferring shear, normal forces and sometimes even bending moments. Two joints that can take up many different forces and are possible to execute in glass are the Gooseneck and Kanawa joints.

4. **What is the influence of shape on force transfer and how can this interaction be optimized in a glass Sashimono connection design?**
Several of the Sashimono joints were modelled by hand to gain a better understanding of their force transfer. The Gooseneck and Kanawa joints were further schematized under tension force and a bending moment. This creates more insight into the influence of parameters on the magnitude of stresses in the material, which is critical for the strength of the Sashimono joint. The hand modelling showed that the Gooseneck joint under tension with a chin width of 90 mm results in peak stresses of 43 N/mm^2 under a force of 5.6 kN. Increasing this chin width to 110 mm results in peak stresses of 71 N/mm^2 under the same force. Increasing this part of the geometry by 22% results in an increase of 65% in tensile stresses in the material.

It is important to note that these are just approximations of the expected stresses. The joints are heavily simplified, therefore these calculated stresses cannot be directly used for the prediction of the numerical models or experiments. They mainly serve from a qualitative point of view to compare the different joints.

The force transfer was optimized using a parametric model in Grasshopper. All dimensions and the curvature of the geometry were varied. The variations in design

were then modelled using FEA software, to compare the expected stresses to the hand calculations. The model showed an increase in the stresses compared to the hand calculations of factor 4. These models also visualized the force transfer and stress trajectories. From this optimization of the Gooseneck joint, it turned out that the width of the chin and the curvature of the geometry were of the largest influence on the stress distribution. For example, increasing the width of the chin by 22% increased the stresses by 67%. For the Kanawa joint under tension, the most influential parameter was the size of the dowel and the curvature of the dowel geometry. For the Kanawa beam model, the length of the contact surface was most influential, along with the curvature of the "arms" of the joint.

Experiments were conducted to validate these analytical and numerical calculations. First, the joints were tested in pure tension, using polarizing filters to visualize the stress trajectories. The Kanawa beam was also tested under a four point bending test. In this setup, the force transfer was very different than under pure tension. From these experiments can be concluded that the practical placement of the interlayer should also be taken into account when optimizing the geometry. This means increasing the curvature everywhere, not only at points critical to glass. Also taking into account easy assembly of the interlayer. Additionally, the experiments showed the geometry should be optimized for out of plane movement and post-fracture behaviour. Looking at the waterjet samples, the edge quality was worst where the curvature of the geometry was smallest. This often coincided with locations of peak stresses. This strongly influenced the failure strength of the samples. Therefore the curvature should locally be optimized based on the production method.

In a nutshell, the shape is of influence on force transfer, because the width of the section influences normal stresses, and the eccentricity of force transfer influences bending stresses. This interaction can be optimized by variation of these parameters using a combination of hand calculations, a parametric model, finite element analysis and experimental testing to validate these approximations.

5. **What is the failure behaviour of the designed Sashimono connection?**
   During the two rounds of experiments, the failure behaviour of the joint was examined using direct visual inspection and microscopy. For the Gooseneck model, the stress trajectories and expected stiffness corresponded well with the models. The samples failed at an average force of 6.0 kN. The model predicted a stiffness of 2.8 N/m, the experiments displayed a stiffness of 3.0 N/m. This means the model therefore turned out to be 5.7% less stiff than the experiments. In tension, the Gooseneck joint failed on one side of the female element, where peak stresses were expected to be highest. It failed on the right side in 71% of the experiments, implicating there was some misalignment in the setup. The joint did not fail brittle, because there was some remaining capacity on the other side of the joint. A microscopy study confirmed that the joint failed in the expected location, showing many branches from the original flaw. This is related to the high energy stored due

to the high forces in the joint.

The stress trajectories coincided less clearly with the model for the Kanawa tension model. The samples failed at an average force of 4.1 kN. The expected stiffness was 0.73 N/m based on the model. The experiments showed a stiffness of 1.1 N/m. The model underestimates the stiffness of the experiments by 33%. The Kanawa joint in tension failed at the smallest section either on the right or left side. In 55% of the experiments it failed on the right side, implying it is less likely any misalignment was present. The samples failed due to the dowel taking up tension forces on a small area. It caused the joint to fail at a relatively low force. Microscopy confirmed the direction from the corner of the dowel to the outer edge of the joint. No post failure capacity was present.

Interestingly, because the tolerances in the Kanawa joint were larger, there was more movement possible in this joint. This influenced the force transfer and therefore resulted in different peak stresses than expected. The Gooseneck model turned out to be almost 3 times as stiff as the Kanawa model. This has two likely reasons. First of all, the geometry of the Kanawa joint is not designed to take up pure tension in the direction that it was tested. Therefore, the geometry itself was a lot less stiff than that of the Gooseneck joint. Secondly, the tolerances were of large influence. Because the Kanawa samples were produced using a waterjet, with quite large tolerances, there was a lot of movement possible in the joint. This meant little force was necessary to displace the joint, resulting in a lower stiffness.

For the Kanawa beam model, locations of peak stresses were similar to the models. The samples failed at an average of 4.0 kN. The force-displacement graph was not linear, but showed varying stiffness with plateaus where the stiffness was around 0. Most likely, this was caused by a combination of the plastic deformation of the interlayer and movement and/or sliding in the machine itself. It was attempted to calibrate the model to the experiments, by increasing the stiffness of the interlayer. This did not result in sufficient stiffness, which implies the stiffness originates from another element in the setup. This could likely be the friction between the concrete plywood frames and the glass. The rotational stiffness was 611 kNm/rad, which is 9.1% of the stiffness compared to a solid beam of the same dimensions.

When testing the Kanawa joint under a bending moment, there were two failure modes, as expected from the FEM. The second failure mode has a limited post-failure capacity, the first one none. When examining the samples under the microscope, it seemed quite likely that this critical impurity was a result of the waterjet itself.

8.2. MAIN RESEARCH QUESTION

The main research question is formulated as follows:

What is a suitable design for a rigid and demountable glass connection using contact pressure?
A suitable design omits adhesives and limits peak stresses in the material, by omitting mechanical connections. The edge quality of such a joint should be as high as possible, preferably using polished edges or a properly calibrated waterjet. In between the glass panels, an interlayer should be placed with a stiffness a little below 70 GPa and which is easily shapeable into the desired geometry. Inspiration can be taken from traditional Japanese joinery called Sashimono, taking into account the possibility to take up a moment force. The Gooseneck and Kanawa joint satisfy this requirement. To ensure optimal force transfer, tensile stresses in the material should be minimized. To achieve this the geometry should be optimized using parametric models, validated with analytical and numerical calculations. A balance should be found between the local section (influencing normal stresses) and the local eccentricity of force transfer (influencing bending stresses). The curvature of the geometry is also of large influence on the stress distribution of the joint. Experiments show that the design of such an optimized joint has a rotational stiffness of 611 kNm/rad, which is 9.1% of the stiffness compared to a solid beam of the same dimensions. A safety mechanism should be designed to prevent complete collapse after the failure of an element of the joint.

This means the designed joint is not fully rigid, but this exploratory study shows there is great potential for such a system. Further optimizing the geometry and the used interlayer could result in a rigid and demountable glass joint, as part of a portal frame.

8.3. RECOMMENDATIONS

The Gooseneck and Kanawa joints were designed, analyzed and tested in this research to develop a rigid and demountable glass joint.

8.3.1. DESIGN GEOMETRY

Due to the time and budget available for this project, only one set of designs was tested. With the lessons learned from the models and experiments, additional iterations of the chosen design should be produced and tested. For example, for the Gooseneck, it would be interesting to decrease the width of the chin as seen in Figure 8.1(a). Using this design, the section of the female element will increase, minimizing normal stresses. In the current design, it appeared that this section was too narrow. For placement of the interface material, it would be wise to increase the curvature around the neck of the design. This makes it easier to fit more suitable materials in between the geometry. In the current design, only the PU85 could be fitted around such a small curvature. Unfortunately, because this material did not have the optimal desired properties, like a very low stiffness.

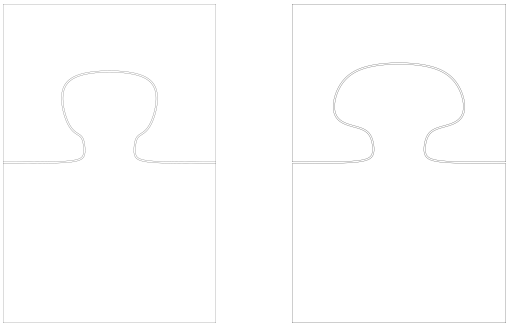

(a) (b)

Figure 8.1: Illustration of possible decreased chin width (a) and increased curvature by increasing the length of the neck (b)

For the Kanawa design, in a new iteration, the dowel should be researched as being round instead of square shaped. An illustration of this option is given in Figure 8.2(a). Decreasing the control points of the joint, creates an even smoother joint, being beneficial for the stress concentration factor. This can be seen in Figure 8.2(b). FEA should prove whether this effect is indeed beneficial. Also decreasing the dowel size, as seen in Figure 8.2(c) would increase the width of the critical section under pure tension. This would also likely decrease stresses due to the eccentricity and therefore increase the strength of the joint. In the current design, the required size of the dowel was likely overestimated.

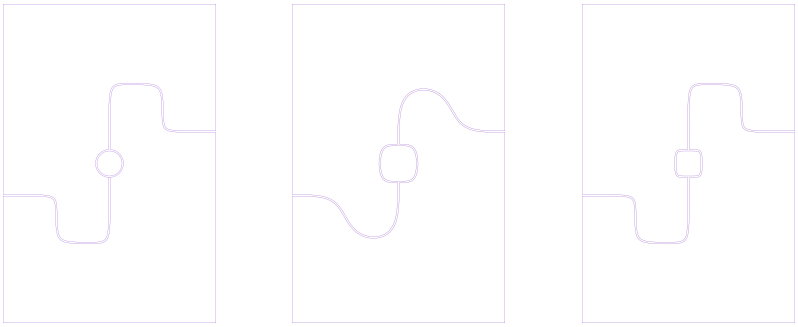

(a) (b) (c)

Figure 8.2: Illustration of possible rounding of the dowel (a) and geometry (b) and decreased size dowel (c)

For both joints, samples with a decreased gap should be produced, to see what the effect of a decreased interlayer thickness would be. Especially if deviations at the glass edge are minimized, an interlayer of 2 mm should be sufficient. This would increase the possibility to shape the interlayer into the desired geometry.

During this project, additional Sashimono joints were discussed, which were not optimized and tested. For example, the spline joint shown in Figure 4.11(b) should be considered in future research.

8.3.2. PRODUCTION

For the best edge quality, polishing the edges is the preferred option. In case the samples will be cut using a waterjet, the curvature of the geometry should be locally optimized for the stress distributions in further research. Looking at the waterjet samples, the edge quality was worst where the curvature of the geometry was smallest. This often coincided with locations of peak stresses. This strongly influenced the failure strength of the samples. Also, ensure the waterjet is properly calibrated to the material properties of glass to ensure a better edge quality.

8.3.3. INTERLAYER

This research focused on the optimal shape of the joint, and less on the properties of the interface material. The behaviour of the joint is however highly dependent on the behaviour of the interface material. It is therefore recommended to dive deeper into existing literature to find additional suitable materials. Also, other shaping options should be explored. For example, harder plastics like POM or PA6 could be cut in the desired geometry using a laser cutter or waterjet, without losing any properties due to heating the materials. 3D printing of some suitable plastics is also an option that should be examined.

For future research, it would be wise to consider more materials for the purpose of an interlayer, so more materials can be tested. This could also help determine a suitable theory for the optimal stiffness of a float glass interlayer. One of the current theories for the optimal interlayer stiffness is determined as being a little lower than that of glass, so 70 GPa.

In another theory, it is defined based on the maximum thickness of occurring impurities. In order to be able to properly apply this theory, the thickness of deviations on the glass edge of float glass should be determined. For cast glass, it is determined to be 0.25 mm. It is unsure however what the maximum deviation of the edge of float glass would be, since it is heavily dependent on post-processing techniques and the resulting edge quality. For glass cut by waterjet, perhaps 0.1 mm might be a more realistic estimate. For polished edges, this might even be as low as 0.05 mm.
Once this is determined, secondary criteria should be researched. These mostly apply to practical use, like the transparency of the material.

It is strongly recommended to find a suitable interlayer that can easily be shaped into the desired geometry. For simplification of assembly, it is recommended to attach this interlayer to one half of the joint and then push them together. This would prevent the interlayer from falling out or maligning with the glass panes.
The Kanawa design was now executed completely from glass, but in future research, the dowel should be produced from the same interlayer material, so it might create fewer peak stresses. Additionally, such a dowel would be easier to assemble than a piece of glass enclosed by the interlayer. In the current design, assembling the dowel was a messy process and resulted in two sliding surfaces instead of one. A disadvantage would be that the interlayer will quite likely be non-transparent, and this could cause an unwanted aesthetic for such a dowel.

8.3.4. GLASS TYPE

The experiments in this research were performed using annealed glass. The experiments should be repeated using heat strengthened or even fully tempered glass. Most likely this will increase the strength of the joint, but it will also change the failure pattern. As shown in Chapter 3 treated glass has a different breaking pattern and therefore even less post-fracture strength. It also has an effect on the safety of the material.

These designs were all executed with single pane glass, to eliminate further complicating factors. In future research, the experiments should be executed using laminated glass. This would most likely increase the strength and the safety of the joint. Since it would cause more problems when trying to join the elements, because laminated glass is never perfectly aligned, a solution has to be researched to fit the interlayer. This laminated design would also allow for mechanisms providing out of plane stability.

8.3.5. OUT OF PLANE BEHAVIOUR

Another aspect that has received limited attention in this research, but is very relevant, is the out of plane stability of the joint. The x and z direction of the joints have been analyzed extensively, but in the current design, the joint could just be pushed through and fall out. For timber this is less of a problem, because the sections are quite wide. When using float glass, the beams will be very slender, even when laminating the glass. This requires research for an additional solution to ensure the glass elements stay in place. A suggestion for the out of plane stability using laminated glass can be seen in Figure 8.3 below. The length of the middle pane is slightly elongated

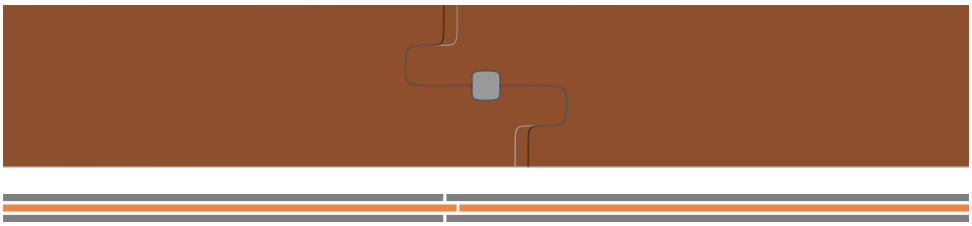

Figure 8.3: Illustration of suggested out of plane restrainment. Seen from the side (upper figure) and from the top (lower figure)

8.3.6. VALIDATION

In future research, the displacement should be measured using strain gauges for local points or a Digital Image Correlation (DIC) system, which would measure the displacement of every single point of the joint. This would also enable the researcher to determine the stresses on a local level and compare them to the FEA. Thus, the numerical values of the model can be validated. Only during the testing of the Kanawa beam under a bending moment, there were lasers measuring the displacement right in the middle. For the other experiments or positions in the samples, only the displacement of the actuator was available. This means no accurate information is available about the actual displacement of the material. Part of the displacement will namely be taken up by movements in the machine or for example the interlayer.

8.3.7. GLOBAL STRUCTURE

The glass Sashimono joint has been discussed extensively in detail, but it is not yet clear how this joint would actually fit in a portal frame global system. It is recommended to determine where exactly in the beam or column the joint would be located and how it can be efficiently mounted and demounted. Also, connections to other elements such as the facade and roof system should be looked into further.

ACKNOWLEDGEMENTS

The finalization of this thesis also marks the end of my time as a student at TU Delft. I would like to express my gratitude towards my graduation committee: Fred Veer, Chris Noteboom, Francesco Messali and Erwin ten Brincke. Thank you for your critical but empathic attitude towards my work and process. I immensely enjoyed working with you, each having a different but valuable approach to the project. Your enthusiasm about the idea and trust in me made this final period a safe and highly rewarding learning experience.

During the period of this research, I had the great opportunity to work as an intern at ABT bv. Thank you to all of the colleagues for their expertise and encouragements. I really appreciate how everyone was eager to make time for me to help me out where needed.

The very valuable experiments would not have been possible without the support from GertJan van Dijken from *Van Dijken Glas Beleving B.V.*. Thank you for all the kindly supplied glass and use of machinery, but mostly for your flexibility to find solutions for any kind of difficulty. It was a great pleasure to work with you, because of your experience and particularly your warm character.

Secondly, I am deeply grateful to *IStructE*: the Institution of Structural Engineers, for granting me the Research Award. This enabled more and bigger scale experiments, resulting in valuable insights for this research.

The experiments could not have been executed without the skills and great ideas of all the employees involved in the workshop at Architecture, the Material lab at 3mE and the Stevinlab at Civil Engineering. Thank you Hans van Ginhoven, Bas Vahl, Kevork Perez Bustos, Sean Scott, Louis den Breejen and Paul Vermeulen for helping me solve all the great puzzles that occurred during the experiments. Luckily, there was always room for laughter, even in times of stress.

Lastly, thank you to everyone who supported me personally. Your trust and humour have been my rocks over the last year.

BIBLIOGRAPHY

Afghani Khoraskani, R. (2015). *Advanced connection systems for architectural glazing*. Springer International Publishing. https://doi.org/10.1007/978-3-319-12997-6

Aiello, S., Campione, G., Minafò, G., & Scibilia, N. (2011). Compressive behaviour of laminated structural glass members. *Engineering Structures - ENG STRUCT*, *33*, 3402–3408. https://doi.org/10.1016/j.engstruct.2011.07.004

Akerboom, R. (2016). Glass columns, exploring the potential of free standing glass columns assembled from stacked cast elements. Retrieved February 17, 2023, from https://repository.tudelft.nl/islandora/object/uuid%3Adf78c330-d40c-491e-a4e9-5b4ac8278e11

Aurik, M. (2017). Structural aspects of an arched glass masonry bridge. Retrieved February 15, 2023, from https://repository.tudelft.nl/islandora/object/uuid%3A312c4015-a08a-41db-b59f-00971597b4b8

Bedon, C., & Santarsiero, M. (2018). Transparency in structural glass systems via mechanical, adhesive, and laminated connections - existing research and developments [_eprint: https://onlinelibrary.wiley.com/doi/pdf/10.1002/adem.201700815]. *Advanced Engineering Materials*, *20*(5), 1700815. https://doi.org/10.1002/adem.201700815

Brittanica, T. E. o. E. (2020, June). *Coefficient of friction | definition, units, & facts | britannica*. Retrieved March 13, 2023, from https://www.britannica.com/science/coefficient-of-friction

Calì, M. (2020). Stress concentration factors in loaded strips and bars [Publisher: Unpublished]. https://doi.org/10.13140/RG.2.2.25957.01764

Christian. (2022, March 22). *Waterjet kerf angle - about kerf & taper in waterjet cutting* [Finepart]. Retrieved February 10, 2023, from https://www.finepart.com/waterjet-cutter/waterjet-kerf-angle/

CIB. (1999, July). *Agenda 21 on sustainable construction* [OCLC: 47649537]. CIB.

Ciullo, P. A., & Hewitt, N. (1999, January 1). PHYSICAL TESTING OF RUBBERthis article was adapted from "RUBBER" by peter a. ciullo and norman hewitt in industrial minerals and their uses, peter a. ciullo (ed.), noyes publications, 1996. In P. A. Ciullo & N. Hewitt (Eds.), *The rubber formulary* (pp. 55–72). William Andrew Publishing. https://doi.org/10.1016/B978-081551434-3.50005-1

Diamut. (n.d.). *Cutting and shaping mills*. Retrieved February 1, 2023, from https://www.diamut.com/ww/glass/milling-cutters/shaped-cnc-milling-cutters/shaped-milling-cutters-cnc

Dimas, M., Oikonomopoulou, F., & Bilow, M. (2022). IN BETWEEN: An interlayer material study for interlocking cast glass blocks. *Challenging Glass Conference Proceedings*, *8*. https://doi.org/10.47982/cgc.8.416

Ebert, J., & Weller, B. (2014). Kunststoffe für den Einsatz als hochbelastbares Klotzungsmaterial [_eprint: https://onlinelibrary.wiley.com/doi/pdf/10.1002/stab.201490056]. *Stahlbau*, *83*, 171–182. https://doi.org/10.1002/stab.201490056

Edge, E. (2000). *Stress concentration fundamentals*. Retrieved January 25, 2023, from https://www.engineersedge.com/material_science/stress_concentration_fundamentals_9902.htm

Haldimann, M., Luible, A., & Overend, M. (2008). Structural use of glass (SED 10) [Publisher: International Association for Bridge and Structural Engineering (IABSE)]. https://app.knovel.com/hotlink/toc/id:kpSUGSED09/structural-use-glass/structural-use-glass

Hartsuijker, C. (2001). *Toegepaste mechanica - Deel 2: Spanningen, vervormingen, verplaatsingen*. Academic Service.

Hoogerwaard, G. (2020). The road to sustainable load bearing glass designs: Possibilities and limitations of current glass design with focus on the connections. Retrieved February 6, 2023, from https://repository.tudelft.nl/islandora/object/uuid%3A7f04302b-a8ce-4424-b8c5-c3faaf8584ad

Johnson, C. P. (2014). *THE USE OF NON-MEMBRANE STRUCTURAL … USE OF NON-MEMBRANE STRUCTURAL GLASS a primer for architects and designers christopher p. johnson, AIA, LEED AP keywords structural glass facades - [PDF document]* [Vdocuments.net]. Retrieved February 6, 2023, from https://vdocuments.net/the-use-of-non-membrane-structural-use-of-non-membrane-structural-glass-a-primer.html

Katsivalis, I., Thomsen, O. T., Feih, S., & Achintha, M. (2018). Strength evaluation and failure prediction of bolted and adhesive glass/steel joints. *Glass Structures & Engineering*, *3*(2), 183–196. https://doi.org/10.1007/s40940-018-0070-0

Louter, C. (2022). Lecture 1.2 - adhesive connections.

Louter, P. C. (2011). Fragile yet ductile: Structural aspects of reinforced glass beams. Retrieved February 1, 2023, from https://repository.tudelft.nl/islandora/object/uuid%3A15375137-d9f6-456d-a4de-df14d167a2d2

Müller-Braun, S., Seel, M., König, M., Hof, P., Schneider, J., & Oechsner, M. (2020). Cut edge of annealed float glass: Crack system and possibilities to increase the edge strength by adjusting the cutting process. *Glass Structures & Engineering*, *5*(1), 3–25. https://doi.org/10.1007/s40940-019-00108-3

Musgraves, J. D., Hu, J., & Calvez, L. (Eds.). (2019). *Springer handbook of glass*. Springer International Publishing. https://doi.org/10.1007/978-3-319-93728-1

Nakahara, Y. (1967). *The complete japanese joinery*. Hartley & Marks.

Narayan, R. L., Tandaiya, P., Narasimhan, R., & Ramamurty, U. (2014). Wallner lines, crack velocity and mechanisms of crack nucleation and growth in a brittle bulk metallic glass. *Acta Materialia*, *80*, 407–420. https://doi.org/10.1016/j.actamat.2014.07.024

Nederland, V. R. (2021). Jaarverslag 2021. https://www.vlakglasrecycling.nl/uploads/jaarverslagen/Jaarverslag_2021_VRN_web.pdf

Oikonomopoulou, F., Bristogianni, T., Barou, L., & Veer, F. A. (2019). Dry interlayers out of cast polyurethane rubber for interlocking cast glass structures: Experimental exploration and validation [Publisher: CRC Press]. *Advances in Engineering Ma-*

terials, Structures and Systems: Innovations, Mechanics and Applications. https://doi.org/10.1201/9780429426506-295

Oikonomopoulou, F., van den Broek, E. A. M., Bristogianni, T., Veer, F. A., & Nijsse, R. (2017). Design and experimental testing of the bundled glass column. *Glass Structures & Engineering*, *2*(2), 183–200. https://doi.org/10.1007/s40940-017-0041-x

Oikonomopoulou, F. (2019). Unveiling the third dimension of glass: Solid cast glass components and assemblies for structural applications [Number: 9]. *A+BE | Architecture and the Built Environment*, (9), 1–352. https://doi.org/10.7480/abe.2019.9.4088

Oikonomopoulou, F., Veer, F., Nijsse, R., & Baardolf, K. (2015). A completely transparent, adhesively bonded soda-lime glass block masonry system. *Journal of Facade Design and Engineering*, *2*, 201–221. https://doi.org/10.3233/FDE-150021

PBL. (2019, July 26). *Circulaire economie* [PBL Planbureau voor de Leefomgeving]. Retrieved February 20, 2023, from https://www.pbl.nl/onderwerpen/circulaire-economie

PWJ. (2015). *Cutting glass with waterjet*. Retrieved February 1, 2023, from https://www.performancewaterjet.com.au/glass-cutting

Quaglini, V., & Dubini, P. (2011). Friction of polymers sliding on smooth surfaces [Publisher: Hindawi]. *Advances in Tribology*, *2011*, e178943. https://doi.org/10.1155/2011/178943

Ravenshorst, G. (2021, September). Lecture 4 - mechanical properties, anisotropy.

Rijksoverheid. (2016, September). Nederland cirulair in 2050. https://open.overheid.nl/documenten/ronl-a6ce8220-07e8-4b64-9f3d-e69bb4ed2f9c/pdf

Sanders, K., Bos, F., ten Brincke, E., & Belis, J. (2021). Edge strength of core drilled and waterjet cut holes in architectural glass. *Glass Structures & Engineering*, *6*(2), 131–145. https://doi.org/10.1007/s40940-021-00146-w

Santarsiero, M., Louter, C., & Nussbaumer, A. (2017). Laminated connections for structural glass components: A full-scale experimental study. *Glass Structures & Engineering*, *2*(1), 79–101. https://doi.org/10.1007/s40940-016-0033-2

Schittich, C. (2007). *Glass construction manual* (2nd, rev. and expanded ed) [Section: 352 p. : illustrations (some color) ; 30 cm]. Birkhäuser ;

Seike, K. (1977). *The art of japanese joinery*. Weatherhill.

Shelby, J. E. (2005). Introduction to glass science and technology (2nd edition) [Publisher: Royal Society of Chemistry (RSC)]. https://app.knovel.com/hotlink/toc/id:kpIGSTE002/introduction-glass-science/introduction-glass-science

Singh, S., Chakraborty, P., & Kitey, R. (2019). Quasi static compression behavior of glass filled epoxy composites. *Procedia Structural Integrity*, *14*, 915–921. https://doi.org/10.1016/j.prostr.2019.07.071

Sumiyoshi, T., & Matsui, G. (1989). *Wood joints in classical japanese architecture*. Kajima Institute Publishing Co., Ltd.

Tuna Kayılı, M., Veer, F., & Çelebi, G. (2016). Assessment of the energy savings and CO2 emissions reduction of glass structures through alternative demolition scenarios. *Glass Structures & Engineering*, *1*(2), 435–449. https://doi.org/10.1007/s40940-016-0024-3

Tuononen, A. J. (2016). Onset of frictional sliding of rubber–glass contact under dry and lubricated conditions [Number: 1 Publisher: Nature Publishing Group]. *Scientific Reports*, *6*(1), 27951. https://doi.org/10.1038/srep27951

Veer, F. (2007). The strength of glass, a nontransparent value. *Heron*, *52*.

Verleg, K. (2019). The structural behaviour of bundled glass columns: Finite element modelling and experimental validation. Retrieved March 22, 2023, from https://repository.tudelft.nl/islandora/object/uuid%3A7737869c-21ad-4257-a12d-6ef43066ecb4

Verschuren, P., & Doorewaard, H. (2010, September 1). *Designing a research project* (2nd). Boom Lemma Uitgevers.

Wurm, J. (2007, December 31). *Glass structures: Design and construction of self-supporting skins*. DE GRUYTER. https://doi.org/10.1007/978-3-7643-8317-6

Yost, J. R., Cregan, M., Bolhassani, M., Akbarzadeh, M., Lu, Y., Chhadeh, P. A., & Schneider, J. (2022). Experimental investigation of a transparent interface material for glass compression members. *Challenging Glass Conference Proceedings*, *8*. https://doi.org/10.47982/cgc.8.395

Zeus. (2005). Friction and wear of polymers. http://www.appstate.edu/~clementsjs/polymerproperties/$p$lastics_$f$riction$5f$w$ear.pdf

V

Appendices

A

CALCULATIONS

A.1. STRESSES SASHIMONO

Each of the forces applied on the geometry correspond with the given force from the Abaqus model at 2 mm displacement.

A.1.1. GOOSENECK

TENSION FEMALE ELEMENT

5.6 kN, means 2.8 kN on each half. The minimum height of the element is approximately 90 mm. This results in.

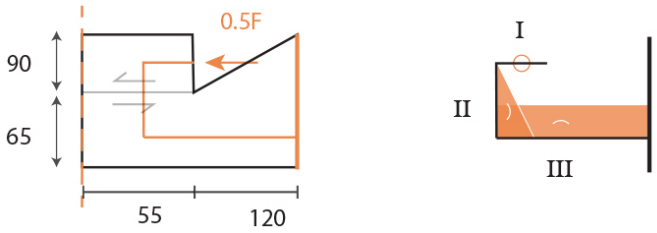

Figure A.1: Dimensions for the Gooseneck model

Section I

$$A = 10 \cdot 90 = 900 mm^2 \tag{A.1}$$

$$\sigma = \frac{N}{A} = \frac{2800}{900} = -3.1 N/mm^2 \tag{A.2}$$

A

Section II

$$\tau = \frac{V}{bh} = \frac{2800}{10 \cdot 55} = 5.1 N/mm^2 \tag{A.3}$$

Bending moment is

$$M = F \cdot L = 2800 \cdot 77.5 = 217000 Nmm \tag{A.4}$$

$$W = \frac{1}{6} \cdot b \cdot h^2 = \frac{1}{6} \cdot 10 \cdot 55^2 = 5040 mm^3 \tag{A.5}$$

$$\sigma = \frac{M}{W} = \frac{217000}{5040} = 43 N/mm^2 \tag{A.6}$$

Section III

$$A = 10 \cdot 65 = 650 mm^2 \tag{A.7}$$

$$\sigma = \frac{2800}{650} = 4.3 N/mm^2 \tag{A.8}$$

Bending moment

$$W = \frac{1}{6} \cdot 10 \cdot 65^2 = 7040 mm^3 \tag{A.9}$$

$$\sigma = \frac{217000}{7040} = 31 N/mm^2 \tag{A.10}$$

$$\sigma_{total} = 4.3 + 31 = 35 N/mm^2 \tag{A.11}$$

MOMENT MALE ELEMENT

$M = 550 \cdot 1100 = 605000$ Nmm. The lever arm is 290 mm from equation 5.7 it then follows that F = 2.1 kN.

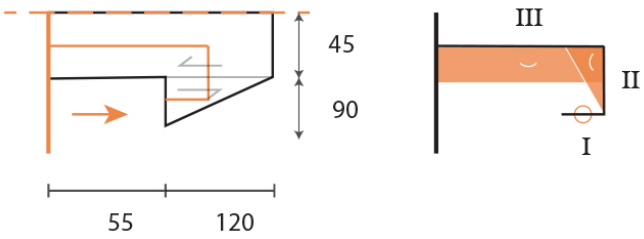

Figure A.2: Dimensions for the Gooseneck model

Section I

$$A = 10 \cdot 45 = 450mm^2 \tag{A.12}$$

$$\sigma = \frac{N}{A} = \frac{2100}{450} = -4.7N/mm^2 \tag{A.13}$$

Section II

$$\tau = \frac{V}{bh} = \frac{2100}{10 \cdot 120} = 1.75N/mm^2 \tag{A.14}$$

Bending moment is

$$M = F \cdot L = 2100 \cdot 67.5 = 141750Nmm \tag{A.15}$$

$$W = \frac{1}{6} \cdot b \cdot h^2 = \frac{1}{6} \cdot 10 \cdot 120^2 = 24000mm^3 \tag{A.16}$$

$$\sigma = \frac{M}{W} = \frac{141750}{24000} = 5.9N/mm^2 \tag{A.17}$$

Section III

$$A = 10 \cdot 45 = 450mm^2 \tag{A.18}$$

$$\sigma = \frac{2100}{450} = 4.7N/mm^2 \tag{A.19}$$

Bending moment

$$W = \frac{1}{6} \cdot 10 \cdot 45^2 = 3375mm^3 \tag{A.20}$$

$$\sigma = \frac{141750}{3375} = 42N/mm^2 \tag{A.21}$$

$$\sigma_{total} = 4.7 + 42 = 47N/mm^2 \tag{A.22}$$

A

MOMENT FEMALE ELEMENT

The bending moment is equal to that of the male element. Dimensions are the same as in Figure A.1.

Section I

$$A = 10 \cdot 90 = 900mm^2 \tag{A.23}$$

$$\sigma = \frac{N}{A} = \frac{2100}{900} = -2.3N/mm^2 \tag{A.24}$$

Section II

$$\tau = \frac{V}{bh} = \frac{2100}{10 \cdot 55} = 3.8N/mm^2 \tag{A.25}$$

Bending moment is

$$M = F \cdot L = 2100 \cdot 77.5 = 162750Nmm \tag{A.26}$$

$$W = \frac{1}{6} \cdot b \cdot h^2 = \frac{1}{6} \cdot 10 \cdot 55^2 = 5040mm^3 \tag{A.27}$$

$$\sigma = \frac{M}{W} = \frac{162750}{5040} = 32N/mm^2 \tag{A.28}$$

Section III

$$A = 10 \cdot 65 = 650mm^2 \tag{A.29}$$

$$\sigma = \frac{2100}{650} = 3.2N/mm^2 \tag{A.30}$$

Bending moment

$$W = \frac{1}{6} \cdot 10 \cdot 65^2 = 7040mm^3 \tag{A.31}$$

$$\sigma = \frac{162750}{7040} = 23N/mm^2 \tag{A.32}$$

$$\sigma_{total} = 3.2 + 23 = 26N/mm^2 \tag{A.33}$$

A.1.2. KANAWA

TENSION ELEMENT

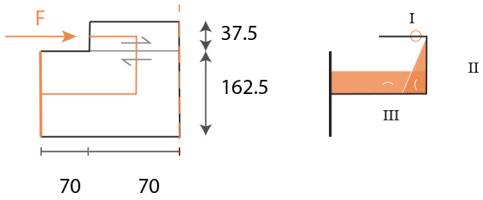

Figure A.3: Dimensions of Kanawa element under tension

Section I

$$A = 10 \cdot 37.5 = 375 mm^2 \tag{A.34}$$

$$\sigma = \frac{N}{A} = \frac{1300}{375} = -3.5 N/mm^2 \tag{A.35}$$

Section II

$$\tau = \frac{V}{bh} = \frac{1300}{10 \cdot 70} = 1.9 N/mm^2 \tag{A.36}$$

Bending moment is

$$M = F \cdot L = 1300 \cdot 100 = 130000 Nmm \tag{A.37}$$

$$W = \frac{1}{6} \cdot b \cdot h^2 = \frac{1}{6} \cdot 10 \cdot 70^2 = 8170 mm^3 \tag{A.38}$$

$$\sigma = \frac{M}{W} = \frac{130000}{8170} = 16 N/mm^2 \tag{A.39}$$

Section III

$$A = 10 \cdot 162.5 = 1625 mm^2 \tag{A.40}$$

$$\sigma = \frac{1300}{1625} = 0.8 N/mm^2 \tag{A.41}$$

Bending moment

$$W = \frac{1}{6} \cdot 10 \cdot 162.5^2 = 44000 mm^3 \tag{A.42}$$

A

$$\sigma = \frac{130000}{44000} = 3.0 N/mm^2 \tag{A.43}$$

$$\sigma_{total} = 0.8 + 3.0 = 3.8 N/mm^2 \tag{A.44}$$

MOMENT BOTTOM ELEMENT

For a bending moment of 0.61 kNm, the resultant force F_5 for the long lever arm would be 1.98 kN.

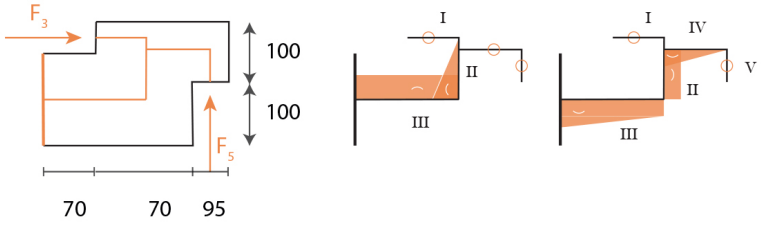

Figure A.4: Dimensions for Kanawa element under a bending moment

Section II

$$A = 10 \cdot 70 = 700 mm^2 \tag{A.45}$$

$$\sigma = \frac{N}{A} = \frac{1980}{700} = 2.8 N/mm^2 \tag{A.46}$$

Bending moment is

$$M = F \cdot L = 1980 \cdot 82.5 = 163000 Nmm \tag{A.47}$$

$$W = \frac{1}{6} \cdot b \cdot h^2 = \frac{1}{6} \cdot 10 \cdot 70^2 = 8170 mm^3 \tag{A.48}$$

$$\sigma = \frac{M}{W} = \frac{163000}{8170} = 20 N/mm^2 \tag{A.49}$$

$$\sigma_{total} = 2.8 + 20 = 23 N/mm^2 \tag{A.50}$$

Section III
Bending moment

$$M = F \cdot L = 1980 \cdot 187.5 = 371000 Nmm \tag{A.51}$$

$$W = \frac{1}{6} \cdot 10 \cdot 162.5^2 = 44000mm^3 \tag{A.52}$$

$$\sigma = \frac{371000}{44000} = 8.4N/mm^2 \tag{A.53}$$

Section IV

$$\tau = \frac{V}{bh} = \frac{1980}{10 \cdot 100} = 2.0N/mm^2 \tag{A.54}$$

Bending moment

$$M = F \cdot L = 1980 \cdot 82.5 = 163000Nmm \tag{A.55}$$

$$W = \frac{1}{6} \cdot 10 \cdot 100^2 = 16700mm^3 \tag{A.56}$$

$$\sigma = \frac{163000}{16700} = 9.8N/mm^2 \tag{A.57}$$

Section V

$$A = 10 \cdot 95 = 950mm^2 \tag{A.58}$$

$$\sigma = \frac{N}{A} = \frac{1980}{950} = 2.1N/mm^2 \tag{A.59}$$

MOMENT TOP ELEMENT

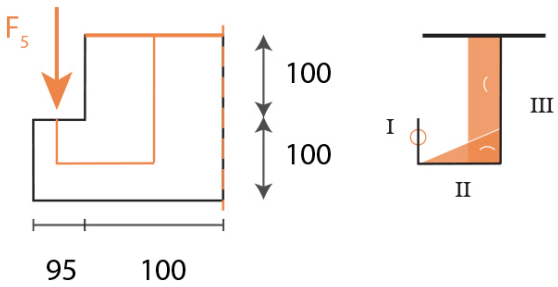

Figure A.5: Dimensions top element Kanawa under a bending moment

Section I

A

$$A = 10 \cdot 95 = 950 mm^2 \tag{A.60}$$

$$\sigma = \frac{N}{A} = \frac{1980}{950} = -2.1 N/mm^2 \tag{A.61}$$

Section II

$$\tau = \frac{V}{bh} = \frac{1980}{10 \cdot 100} = 1.98 N/mm^2 \tag{A.62}$$

Bending moment is

$$M = F \cdot L = 1980 \cdot 100 = 198000 Nmm \tag{A.63}$$

$$W = \frac{1}{6} \cdot b \cdot h^2 = \frac{1}{6} \cdot 10 \cdot 100^2 = 16700 mm^3 \tag{A.64}$$

$$\sigma = \frac{M}{W} = \frac{198000}{16700} = 12 N/mm^2 \tag{A.65}$$

Section III

$$A = 10 \cdot 100 = 1000 mm^2 \tag{A.66}$$

$$\sigma = \frac{1980}{1000} = 2.0 N/mm^2 \tag{A.67}$$

Bending moment

$$W = \frac{1}{6} \cdot 10 \cdot 100^2 = 16700 mm^3 \tag{A.68}$$

$$\sigma = \frac{198000}{16700} = 12 N/mm^2 \tag{A.69}$$

$$\sigma_{total} = 2.0 + 12 = 14 N/mm^2 \tag{A.70}$$

MOMENT TOP ELEMENT II

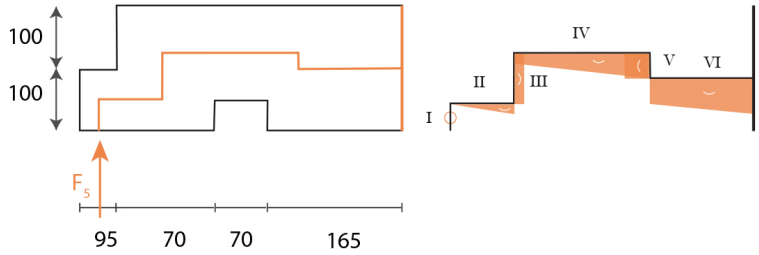

Figure A.6: Dimensions bottom element Kanawa II

Section I

$$A = 10 \cdot 95 = 950mm^2 \tag{A.71}$$

$$\sigma = \frac{N}{A} = \frac{1980}{950} = -2.1N/mm^2 \tag{A.72}$$

Section II

$$\tau = \frac{V}{bh} = \frac{1980}{10 \cdot 100} = 2.0N/mm^2 \tag{A.73}$$

Bending moment is

$$M = F \cdot L = 1980 \cdot 82.5 = 163000Nmm \tag{A.74}$$

$$W = \frac{1}{6} \cdot b \cdot h^2 = \frac{1}{6} \cdot 10 \cdot 100^2 = 66700mm^3 \tag{A.75}$$

$$\sigma = \frac{M}{W} = \frac{163000}{66700} = 2.45N/mm^2 \tag{A.76}$$

Section III

$$A = 10 \cdot 70 = 700mm^2 \tag{A.77}$$

$$\sigma = \frac{N}{A} = \frac{1980}{700} = -2.8N/mm^2 \tag{A.78}$$

Bending moment

$$M = F \cdot L = 1980 \cdot 82.5 = 163000Nmm \tag{A.79}$$

A

$$W = \frac{1}{6} \cdot 10 \cdot 70^2 = 8170 mm^3 \tag{A.80}$$

$$\sigma = \frac{163000}{8170} = 20 N/mm^2 \tag{A.81}$$

$$\sigma_{total} = -2.8 + 20 = 17 N/mm^2 \tag{A.82}$$

Section IV

$$\tau = \frac{V}{bh} = \frac{1980}{10 \cdot 162.5} = 1.2 N/mm^2 \tag{A.83}$$

Bending moment

$$M = F \cdot L = 1980 \cdot 187.5 = 371000 Nmm \tag{A.84}$$

$$W = \frac{1}{6} \cdot 10 \cdot 162.5^2 = 44000 mm^3 \tag{A.85}$$

$$\sigma = \frac{371000}{44000} = 8.4 N/mm^2 \tag{A.86}$$

Section VI
Bending moment

$$M = F \cdot L = 1980 \cdot 400 = 792000 Nmm \tag{A.87}$$

$$W = \frac{1}{6} \cdot 10 \cdot 200^2 = 66700 mm^3 \tag{A.88}$$

$$\sigma = \frac{792000}{66700} = 12 N/mm^2 \tag{A.89}$$

Combining the stresses from the critical sections III from the first calculations and from section VI from the second, this results in a total stress of:

$$\sigma_{total} = 14 + 12 = 26 N/mm^2 \tag{A.90}$$

A

A.2. DIMENSIONS TENSILE TESTS

For the experiments, the aluminium plates glued to the glass had to be designed, in order to ensure they would not fail before the glass failed. For this reason the shear strength of the bolts, the bearing resistance of the plate, the tensile resistance of the plates and the yield strength were calculated.

The bolts used were M12, class 12.9. The shear face does not go through the thread of the bolt. The dimension of the alumnium plates is 150 mm x400 mm, see Figure A.7. Grade EN AW-1050A.

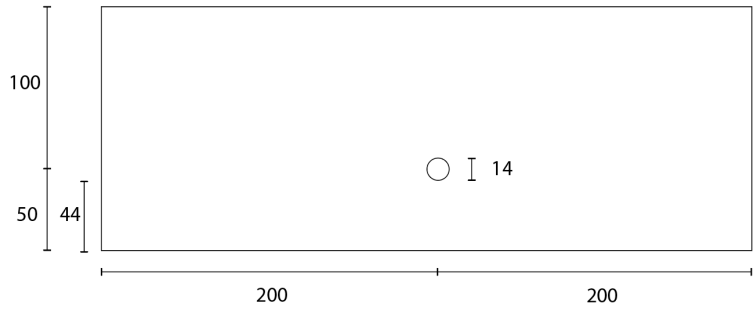

Figure A.7: Dimensions aluminium plates

A.2.1. SHEAR STRENGTH BOLTS

The formula to determine the shear strength of bolts is as follows:

$$F_{v,Rd} = \frac{\alpha_v f_{ub} A_s}{\gamma_{M2}} = \frac{0.6 \cdot 1200 \cdot 12^2 \cdot \pi/4}{1.25} = 65kN \tag{A.91}$$

Because two aluminium plates will take up the load, the maximum force that can be applied during the experiments is 130 kN in order to prevent shear failure of the bolts.

A.2.2. BEARING RESISTANCE PLATE

$$k_1 = 2.8\frac{e_2}{d_0} = 2.8\frac{194}{14} = 39 \rightarrow 2.5 \tag{A.92}$$

$$\alpha_b = \frac{e_1}{3d_0} = \frac{44}{3 \cdot 14} = 1.0 \tag{A.93}$$

$$F_{b,Rd} = \frac{k_1 \alpha_b f_u d t}{\gamma_{M2}} = \frac{2.5 \cdot 1 \cdot 65 \cdot 12 \cdot 6 \cdot 10^{-3}}{1.25} = 9.4kN \tag{A.94}$$

Again there are 2 aluminium plates, so this means the sample can take up 19 kN before the aluminium plate would fail in bearing resistance.

A

A.2.3. TENSILE RESISTANCE PLATES

$$A = b \cdot t = 400 \cdot 6 = 2400 mm^2 \tag{A.95}$$

$$A_{net} = (b - d_0)\, t = (400 - 14)6 = 2316 mm^2 \tag{A.96}$$

$$N_{t,Rd} = \frac{0.9 A_{net} f_u}{\gamma_{M2}} = \frac{0.9 \cdot 2316 \cdot 65}{1.25} = 108 kN \tag{A.97}$$

Two plates results in a tensile resistance of 216 kN.

A.2.4. YIELDING RESISTANCE PLATES

$$N_{pl,Rd} = \frac{A \cdot f_y}{\gamma_{M0}} = \frac{2400 \cdot 20}{1} = 48 kN \tag{A.98}$$

This results in a total yielding resistance of 96 kN.

The critical value is the bearing resistance of the plates. During the experiments, a maximum of 19 kN can be applied before the aluminium plates become critical.

B

NUMERICAL MODELS

B.1. GRASSHOPPER MODELS

B.1.1. GOOSENECK MODEL

CONSTRUCTION BASE SQUARE

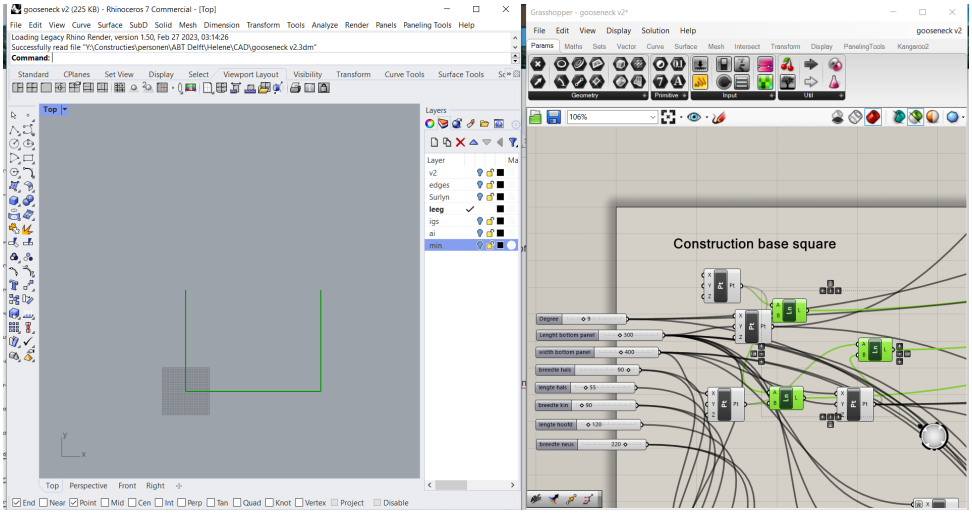

B

CONSTRUCTION CONTROL POINTS

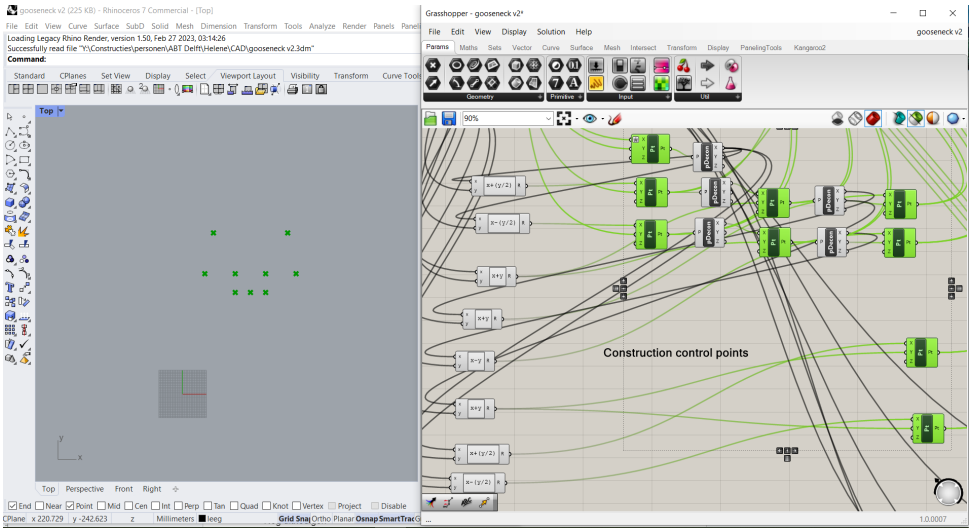

BOUNDARY FROM CONTROL POINTS

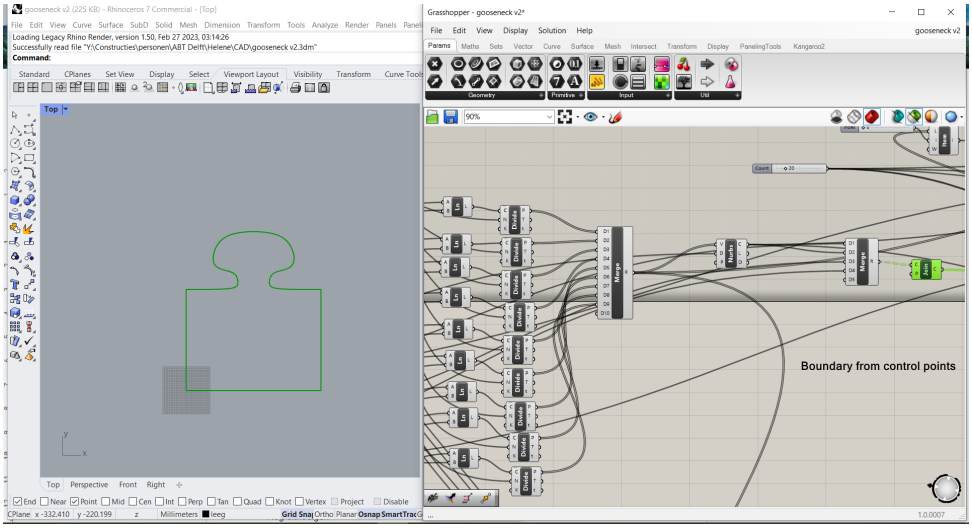

CREATE TOP PANEL WITH OFFSET IN MM

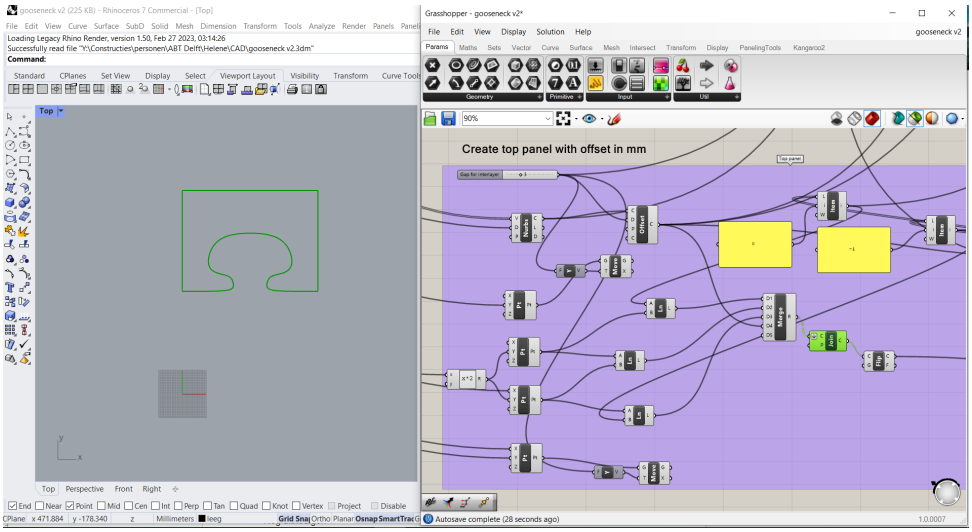

CREATE SURFACE FROM EDGES

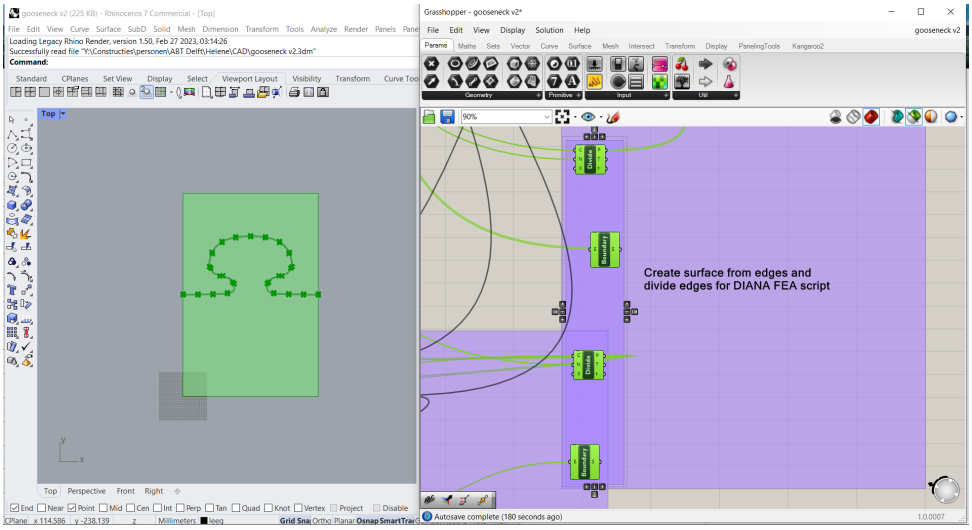

CREATE SURFACE INTERLAYER

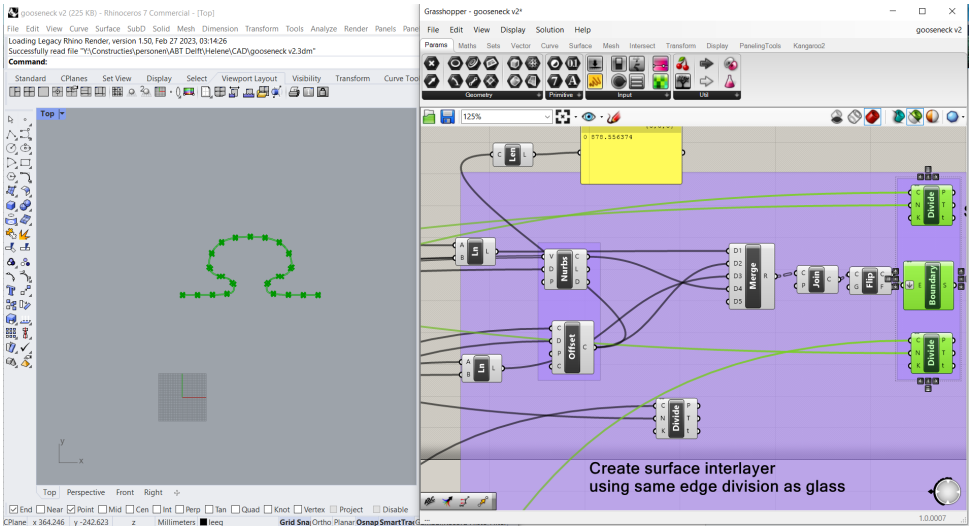

Figure B.1: Description of the parametric Grasshopper model of the Gooseneck design

B.1.2. KANAWA MODEL

CONSTRUCTION BASE SQUARE

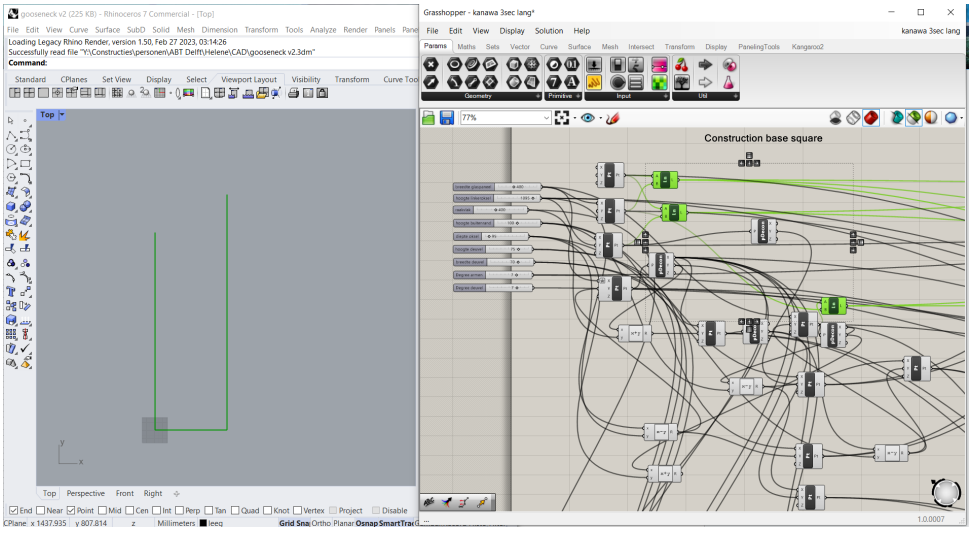

CONSTRUCTION CONTROL POINTS LARGE PARTS

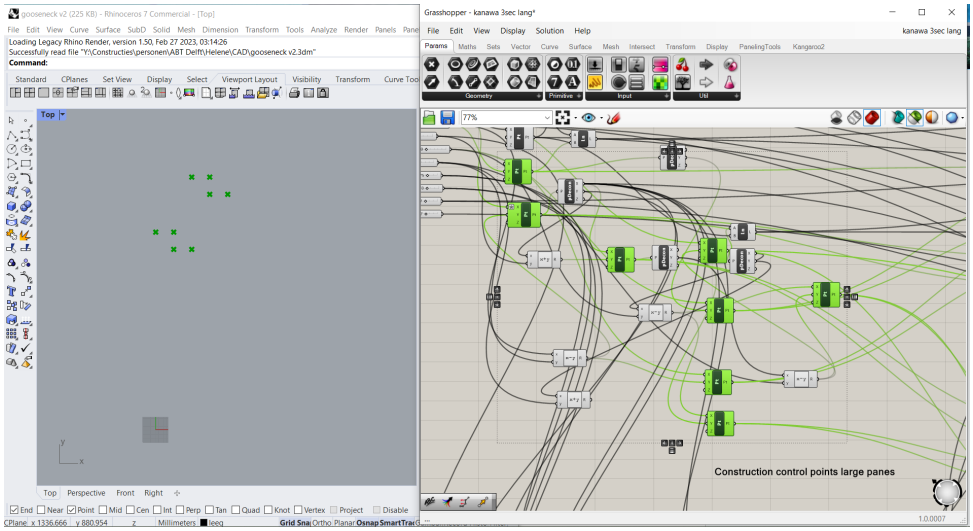

CONSTRUCTION CONTROL POINTS DOWEL

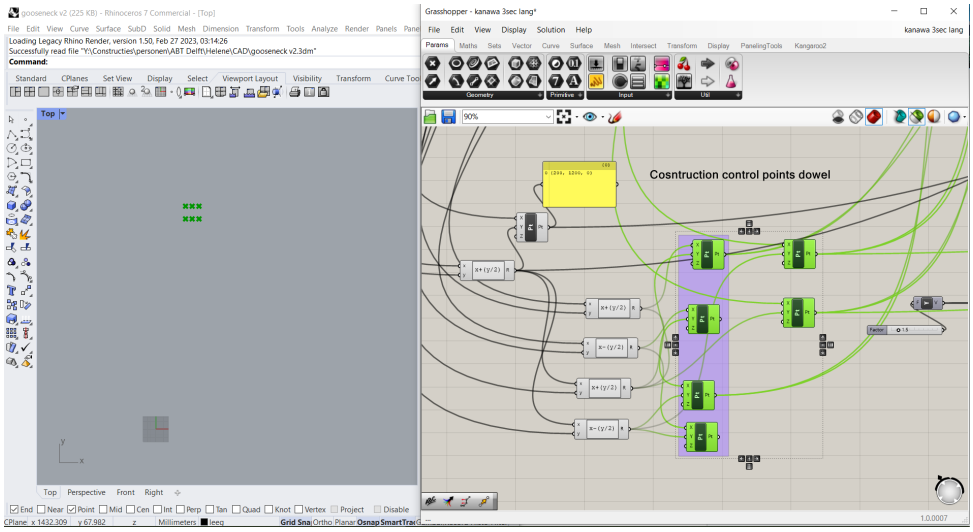

B

BOUNDARY FROM CONTROL POINTS

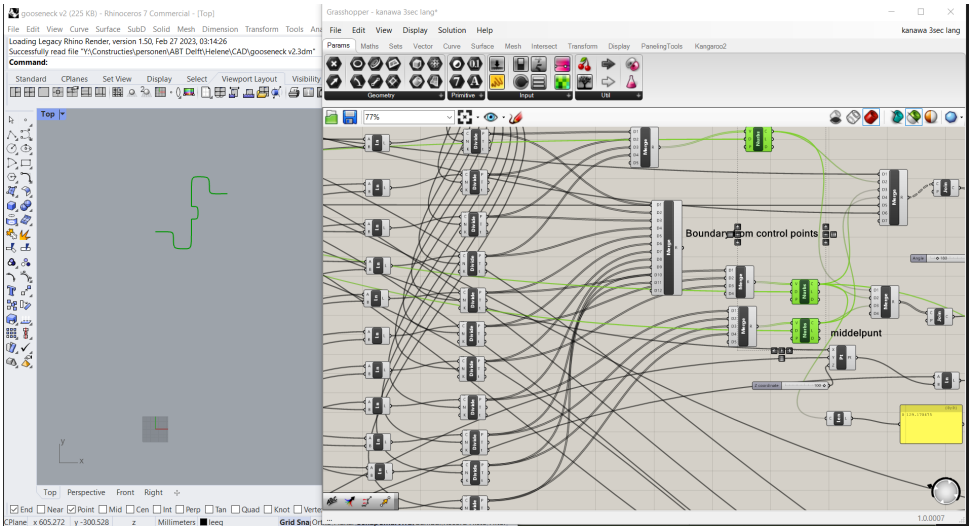

ROTATE ELEMENT AROUND MIDDLE

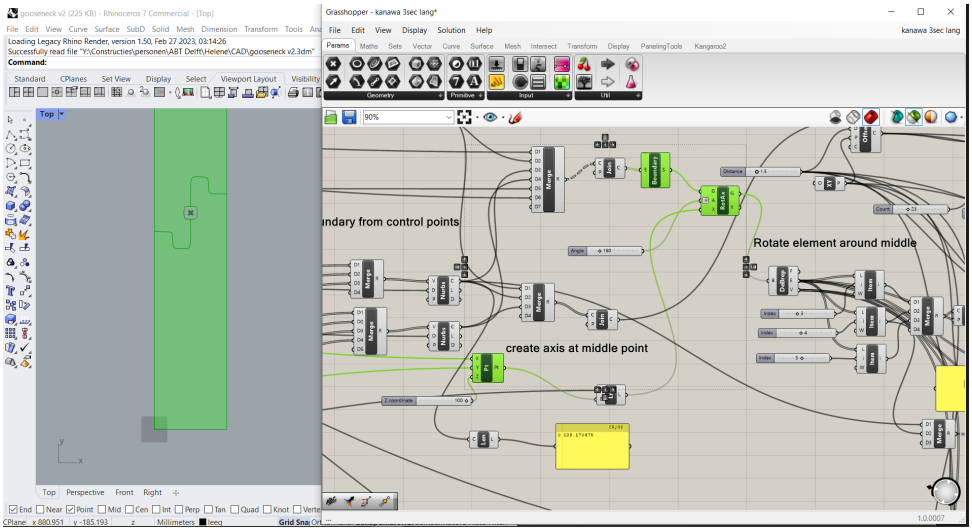

OFFSET CURVE FOR 3 MM GAP

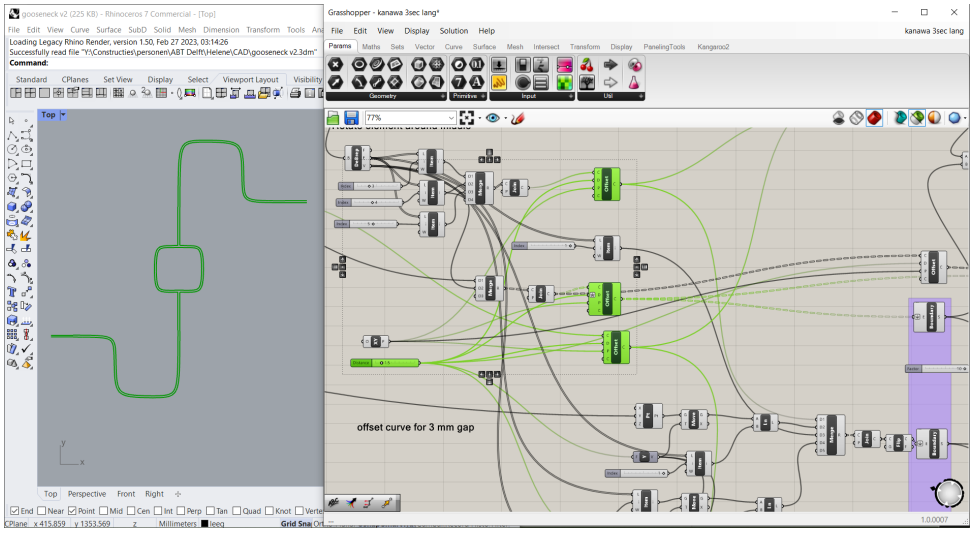

CREATE SURFACE FROM EDGES

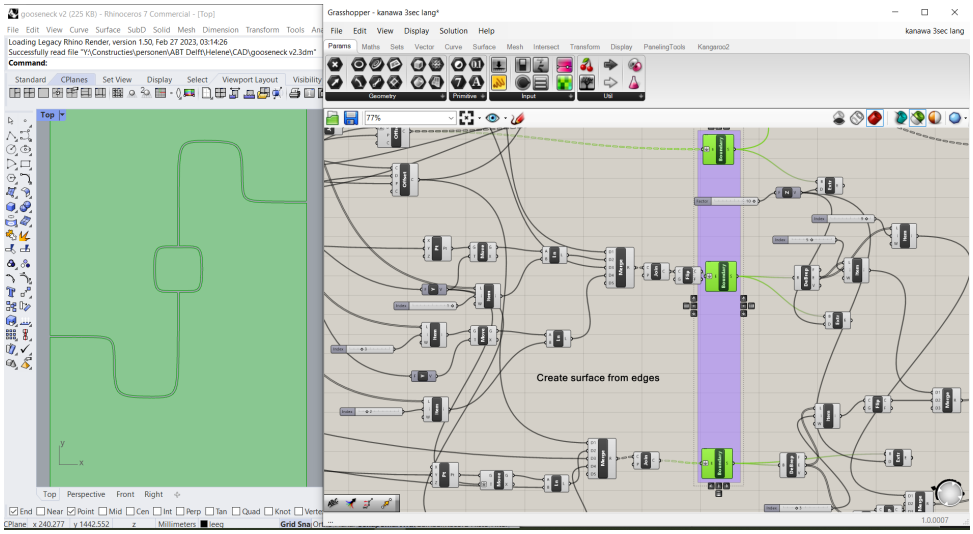

CREATE GEOMETRY OF INTERLAYER

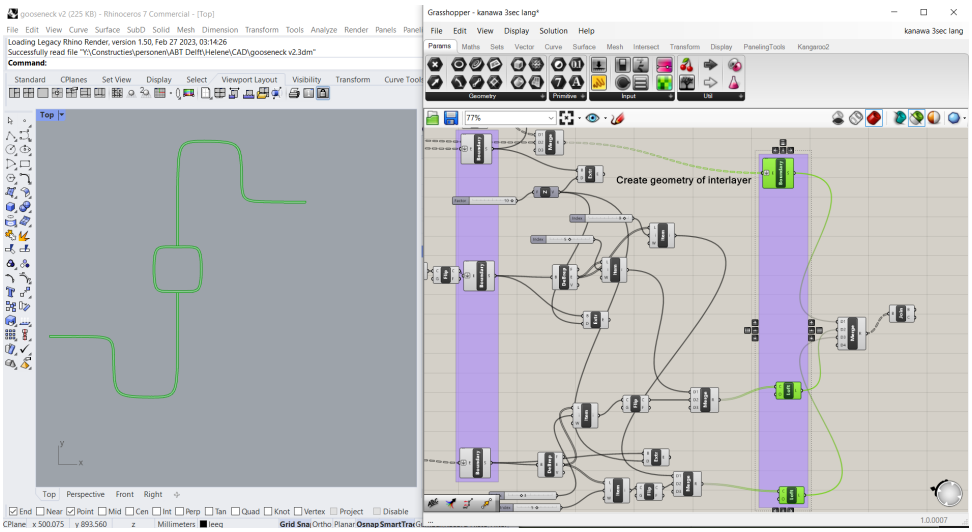

Figure B.2: Description of the parametric Grasshopper model of the Kanawa design

C

Material properties

C.1. EDUPACK DATA

C.1.1. SURLYN

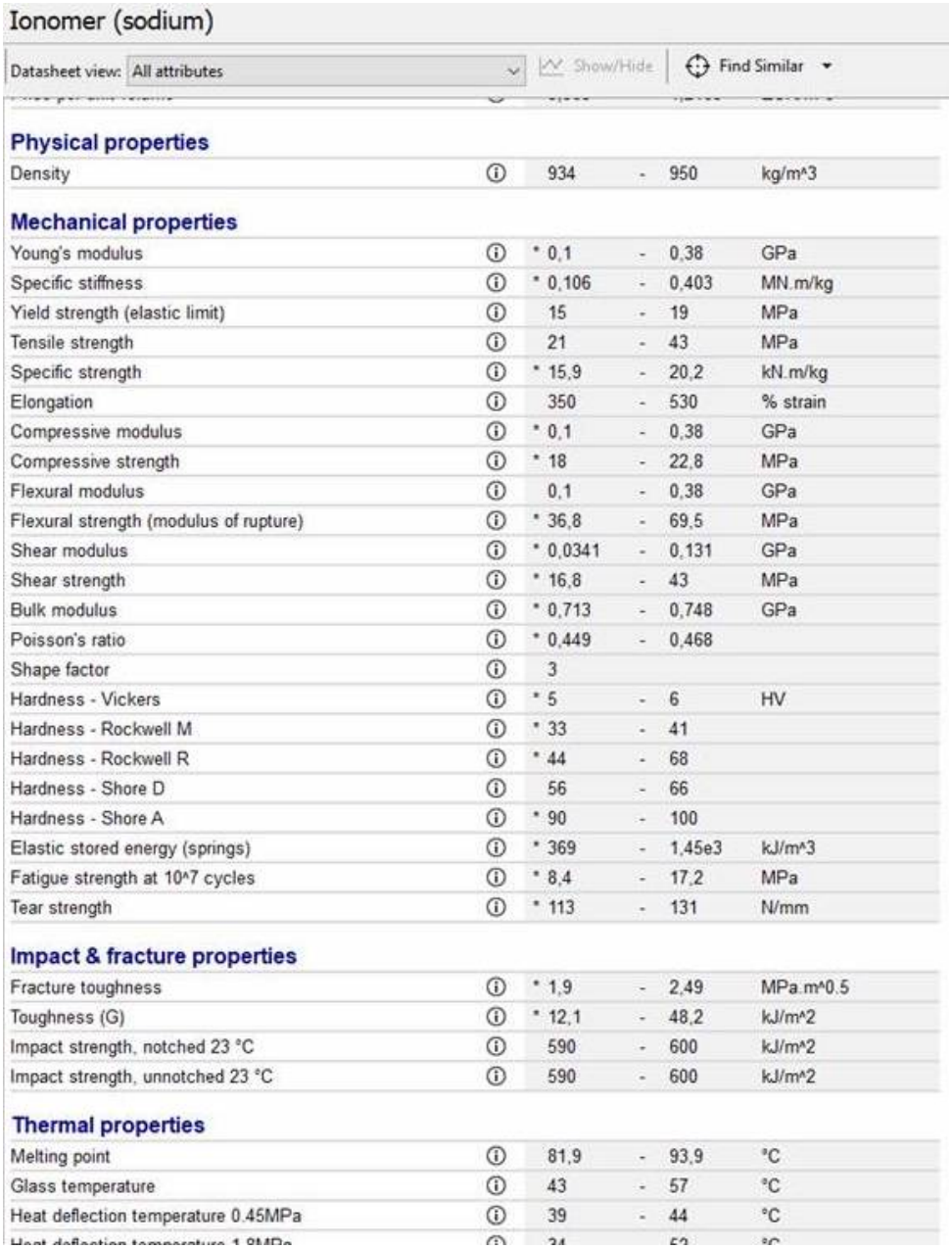

Ionomer (sodium)

Datasheet view: All attributes | Show/Hide | Find Similar

Physical properties					
Density		934	-	950	kg/m^3
Mechanical properties					
Young's modulus		* 0,1	-	0,38	GPa
Specific stiffness		* 0,106	-	0,403	MN.m/kg
Yield strength (elastic limit)		15	-	19	MPa
Tensile strength		21	-	43	MPa
Specific strength		* 15,9	-	20,2	kN.m/kg
Elongation		350	-	530	% strain
Compressive modulus		* 0,1	-	0,38	GPa
Compressive strength		* 18	-	22,8	MPa
Flexural modulus		0,1	-	0,38	GPa
Flexural strength (modulus of rupture)		* 36,8	-	69,5	MPa
Shear modulus		* 0,0341	-	0,131	GPa
Shear strength		* 16,8	-	43	MPa
Bulk modulus		* 0,713	-	0,748	GPa
Poisson's ratio		* 0,449	-	0,468	
Shape factor		3			
Hardness - Vickers		* 5	-	6	HV
Hardness - Rockwell M		* 33	-	41	
Hardness - Rockwell R		* 44	-	68	
Hardness - Shore D		56	-	66	
Hardness - Shore A		* 90	-	100	
Elastic stored energy (springs)		* 369	-	1,45e3	kJ/m^3
Fatigue strength at 10^7 cycles		* 8,4	-	17,2	MPa
Tear strength		* 113	-	131	N/mm
Impact & fracture properties					
Fracture toughness		* 1,9	-	2,49	MPa.m^0.5
Toughness (G)		* 12,1	-	48,2	kJ/m^2
Impact strength, notched 23 °C		590	-	600	kJ/m^2
Impact strength, unnotched 23 °C		590	-	600	kJ/m^2
Thermal properties					
Melting point		81,9	-	93,9	°C
Glass temperature		43	-	57	°C
Heat deflection temperature 0.45MPa		39	-	44	°C

Figure C.1: Surlyn data extracted from Granta EduPack 2022

C.1.2. PVC

PVC (rigid, high impact, molding and extrusion)

Datasheet view: All attributes | Show/Hide | Find Similar

Physical properties					
Density		1,29e3	-	1,46e3	kg/m^3
Mechanical properties					
Young's modulus		2,2	-	3,1	GPa
Specific stiffness		1,59	-	2,28	MN.m/kg
Yield strength (elastic limit)		37,6	-	45,5	MPa
Tensile strength		38	-	46	MPa
Specific strength		26,9	-	33,7	kN.m/kg
Elongation		40	-	80	% strain
Compressive modulus		* 2,2	-	3,1	GPa
Compressive strength		* 37	-	44,3	MPa
Flexural modulus		2,3	-	2,96	GPa
Flexural strength (modulus of rupture)		65	-	81	MPa
Shear modulus		* 0,75	-	1,1	GPa
Bulk modulus		* 3,49	-	5,44	GPa
Poisson's ratio		* 0,395	-	0,405	
Shape factor		6,1			
Hardness - Vickers		12			HV
Hardness - Rockwell M		* 63	-	69	
Hardness - Rockwell R		* 102	-	110	
Hardness - Shore D		77	-	83	
Elastic stored energy (springs)		257	-	417	kJ/m^3
Fatigue strength at 10^7 cycles		* 16,6	-	21,1	MPa
Impact & fracture properties					
Fracture toughness		* 3,63	-	3,85	MPa.m^0.5
Toughness (G)		4,47	-	6,4	kJ/m^2
Impact strength, notched 23 °C		60	-	140	kJ/m^2
Impact strength, notched -30 °C		15	-	35	kJ/m^2
Impact strength, unnotched 23 °C		590	-	600	kJ/m^2

Figure C.2: PVC data extracted from Granta EduPack 2022

C.1.3. PA6

PA6 (molding and extrusion)

Datasheet view: All attributes | Show/Hide | Find Similar

Price per unit volume	* 1,93e3	-	3,84e3	EUR/m^3
Physical properties				
Density	1,13e3	-	1,15e3	kg/m^3
Mechanical properties				
Young's modulus	0,944	-	1,18	GPa
Young's modulus with temperature	1,11	-	1,11	GPa

Parameters: Temperature = 23°C

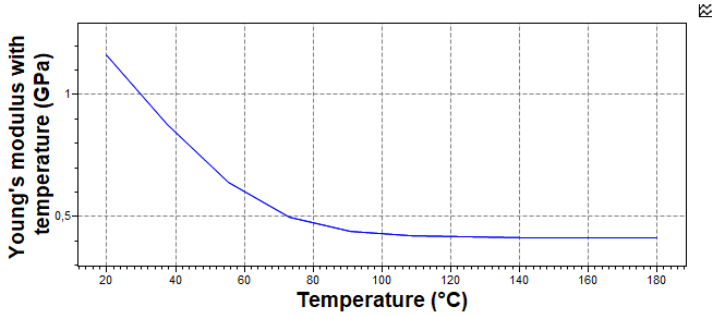

Specific stiffness	0,828	-	1,04	MN.m/kg
Yield strength (elastic limit)	38,6	-	48,2	MPa
Tensile strength	68	-	76	MPa
Specific strength	33,9	-	42,3	kN.m/kg
Elongation	41	-	59	% strain
Elongation at yield	14,6	-	27,7	% strain
Compressive modulus	* 1,01	-	1,11	GPa
Compressive strength	* 41,6	-	46	MPa
Flexural modulus	* 0,77	-	0,923	GPa
Flexural strength (modulus of rupture)	* 43,2	-	52,7	MPa
Shear modulus	* 0,38	-	0,4	GPa
Shear strength	* 19,7	-	24,1	MPa
Bulk modulus	* 1,2	-	1,33	GPa
Poisson's ratio	0,34	-	0,36	
Shape factor	3,79			
Hardness - Vickers	* 12	-	14	HV

Figure C.3: PA6 data extracted from Granta EduPack 2022

C.1.4. POM

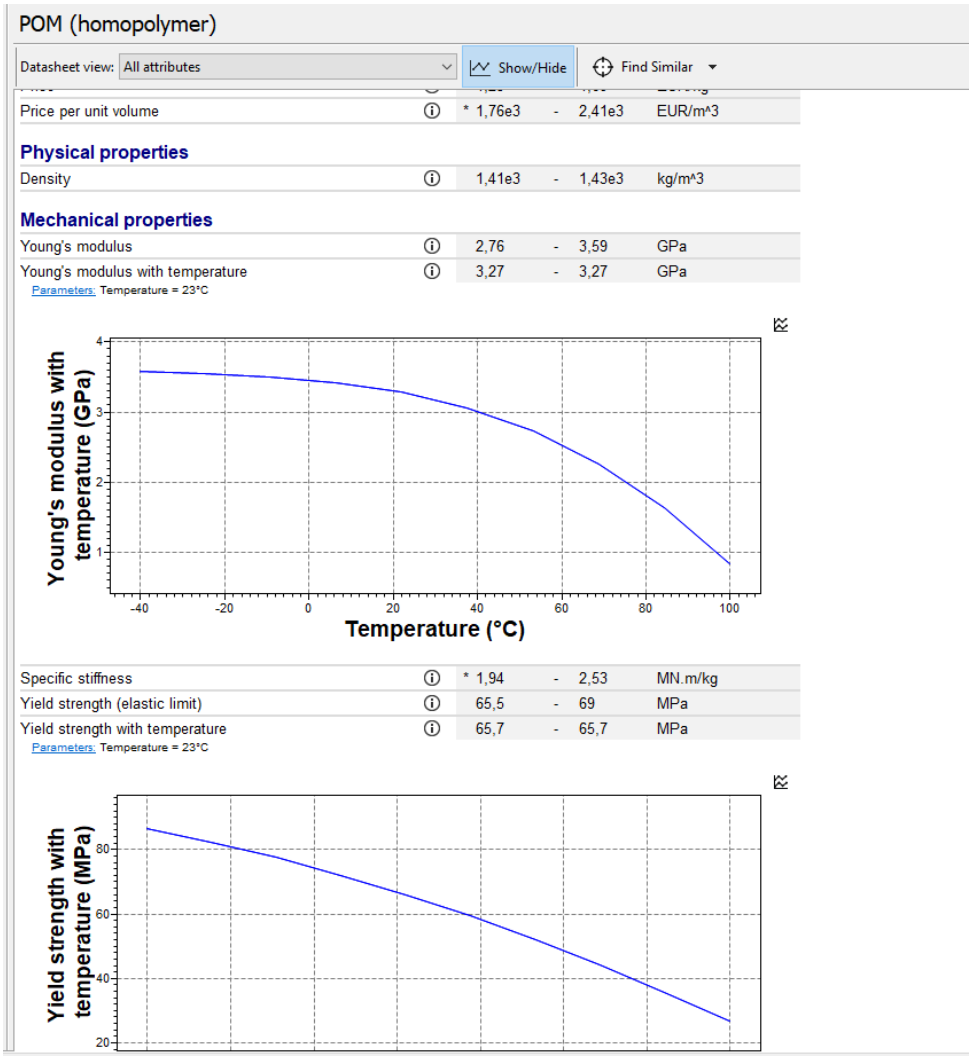

Figure C.4: POM data extracted from Granta EduPack 2022

POM (homopolymer)

Datasheet view: All attributes | Show/Hide | Find Similar

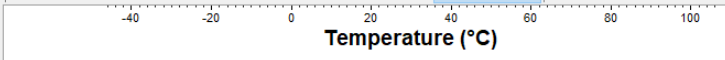

Tensile strength	ⓘ	66,9	-	69	MPa
Specific strength	ⓘ	* 46,1	-	48,6	kN.m/kg
Elongation	ⓘ	10	-	75	% strain
True plastic stress-strain		22,6			MPa

Parameters: Strain = 0,1% strain, Temperature = 23°C

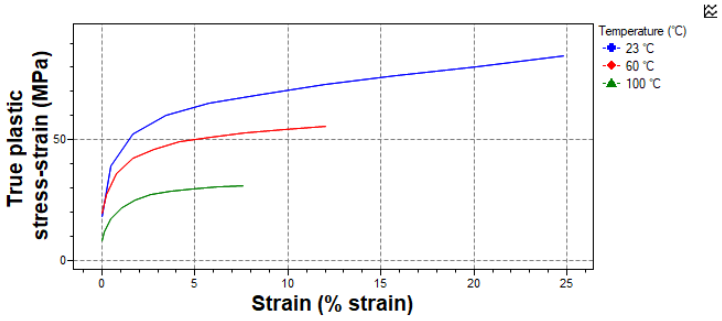

Compressive modulus	ⓘ	4,49	-	4,72	GPa
Compressive strength	ⓘ	* 108	-	124	MPa
Flexural modulus	ⓘ	2,61	-	3,37	GPa
Flexural strength (modulus of rupture)	ⓘ	93,8	-	110	MPa
Shear modulus	ⓘ	* 1,03	-	1,34	GPa
Bulk modulus	ⓘ	* 3,2	-	3,36	GPa
Poisson's ratio	ⓘ	0,33	-	0,35	
Shape factor	ⓘ	5			
Hardness - Vickers	ⓘ	* 20	-	25	HV
Hardness - Rockwell M	ⓘ	92	-	94	
Hardness - Rockwell R	ⓘ	114	-	126	
Elastic stored energy (springs)	ⓘ	* 624	-	826	kJ/m^3
Fatigue strength at 10^7 cycles	ⓘ	* 23,8	-	31	MPa

Figure C.5

TPU (Ether, aromatic, Shore A85/D35)

Datasheet view: All attributes | Show/Hide | Find Similar

Price per unit volume		* 2,28e3	-	3,2e3	EUR/m^3
Physical properties					
Density		1,11e3	-	1,13e3	kg/m^3
Mechanical properties					
Young's modulus		0,0204	-	0,021	GPa
Specific stiffness		0,0182	-	0,0188	MN.m/kg
Yield strength (elastic limit)		* 31,9	-	38,9	MPa
Tensile strength		31,9	-	38,9	MPa
Tensile stress at 100% strain		5,45	-	7,07	MPa
Tensile stress at 300% strain		9,4	-	12,3	MPa
Specific strength		* 28,5	-	34,8	kN.m/kg
Elongation		552	-	645	% strain
Elongation at yield		* 552	-	645	% strain
Compressive modulus		* 0,0197	-	0,0217	GPa
Compressive strength		* 38,3	-	46,7	MPa
Flexural modulus		0,0272	-	0,0398	GPa
Flexural strength (modulus of rupture)		* 53	-	63,5	MPa
Shear modulus		* 0,00679	-	0,00713	GPa
Shear strength		* 25,5	-	38,9	MPa
Bulk modulus		* 0,17	-	0,699	GPa
Poisson's ratio		* 0,48	-	0,495	
Shape factor		1,6			
Hardness - Vickers		* 10	-	12	HV
Hardness - Rockwell M		* 9	-	14	
Hardness - Rockwell R		* 9	-	14	
Hardness - Shore D		30	-	36	
Hardness - Shore A		80	-	90	
Elastic stored energy (springs)		* 2,48e4	-	3,63e4	kJ/m^3
Fatigue strength at 10^7 cycles		* 12,8	-	15,6	MPa
Compression set at 23°C		20,6	-	25,5	%
Compression set at 70°C		42,2	-	64,6	%
Tear strength		78,4	-	95,4	N/mm

Figure C.6: PU data extracted from Granta EduPack 2022

C.2. SUPPLIER DATA

C.2.1. PVC

Technisches Datenblatt PVC-CAW

SIMONA

Handelsname: **PVC-CAW**
Druckdatum: 30.06.2015

Revision: 27.02.2015

	PVC-CAW
Datenblatt-Aktualisierung	27.02.2015
Formmasse extrudiert	PVC-U,EDP,074-05-T33
Formmassennorm extrudiert	DIN EN ISO 1163, Teil 1
Dichte, g/cm³ , DIN EN ISO 1183	1,44
Streckspannung, MPa, DIN EN ISO 527	58
Dehnung bei Streckspannung, % , DIN EN ISO 527	4
Zug-E-Modul, MPa, DIN EN ISO 527	3300
Schlagzähigkeit, KJ/m² , DIN EN ISO 179	-
Kerbschlagzähigkeit, kJ/m², DIN EN ISO 179	4
Shorehärte D (15 s), DIN EN ISO 868	82
Mittlerer thermischer Längenausdehnungskoeffizient, K^{-1} , ISO 11359-2	$0,8 \times 10^{-4}$
Vicat B, °C , DIN EN ISO 306	74
Brandverhalten DIN 4102	DIN 4102 B1 schwerentflammbar 1 bis 4 mm, Allgemeines bauaufsichtliches Prüfzeugnis
Brandverhalten UL 94	UL 94 V-0 ab 1 mm
Brandverhalten NF P 92-501	NF P 92-501 M1 von 1 bis 3 mm
Brandverhalten BS 476	BS 476 class 1 für 3 mm
Durchschlagfestigkeit, kV/mm , DIN IEC 60243-1	39
Spez. Oberflächenwiderstand, Ohm , DIN IEC 60093	10^{13}
Temperatureinsatzbereich, °C	0 bis +60
Physiologische Unbedenklichkeit nach BfR	nein
Physiologische Unbedenklichkeit nach EU	nein
Physiologische Unbedenklichkeit nach FDA	nein

Seite: 1 von 2

Figure C.7



Technisches Datenblatt PVC-CAW

SIMONA

PVC-CAW

Die Daten sind Richtwerte und können in Abhängigkeit von Verarbeitungsverfahren und Probekörperherstellung variieren. Im Regelfall handelt es sich um Durchschnittswerte von Messungen an extrudierten Platten in 4 mm Dicke. Bei ausschließlich im Pressverfahren hergestellten Platten handelt es sich im Regelfall um Messungen an Platten in 20 mm Dicke. Abweichungen sind möglich, wenn Platten in diesen Dicken nicht verfügbar sind. Bei kaschierten Platten beziehen sich die technischen Kennwerte auf die unkaschierten Basisplatten. Die Angaben lassen sich nicht ohne weiteres auf die weiterverarbeiteten Produkte übertragen. Die Eignung von Materialien für einen konkreten Verwendungszweck ist vom Verarbeiter bzw. Anwender zu prüfen. Die technischen Kennwerte sind lediglich eine Planungshilfe. Insbesondere stellen sie keine zugesicherten Eigenschaften dar. Weitere Informationen erhalten Sie in unserem Technical Service Center unter tsc@simona.de.

Seite: 2 von 2

Figure C.8: PVC data as stated by supplier

C.2.2. PA6

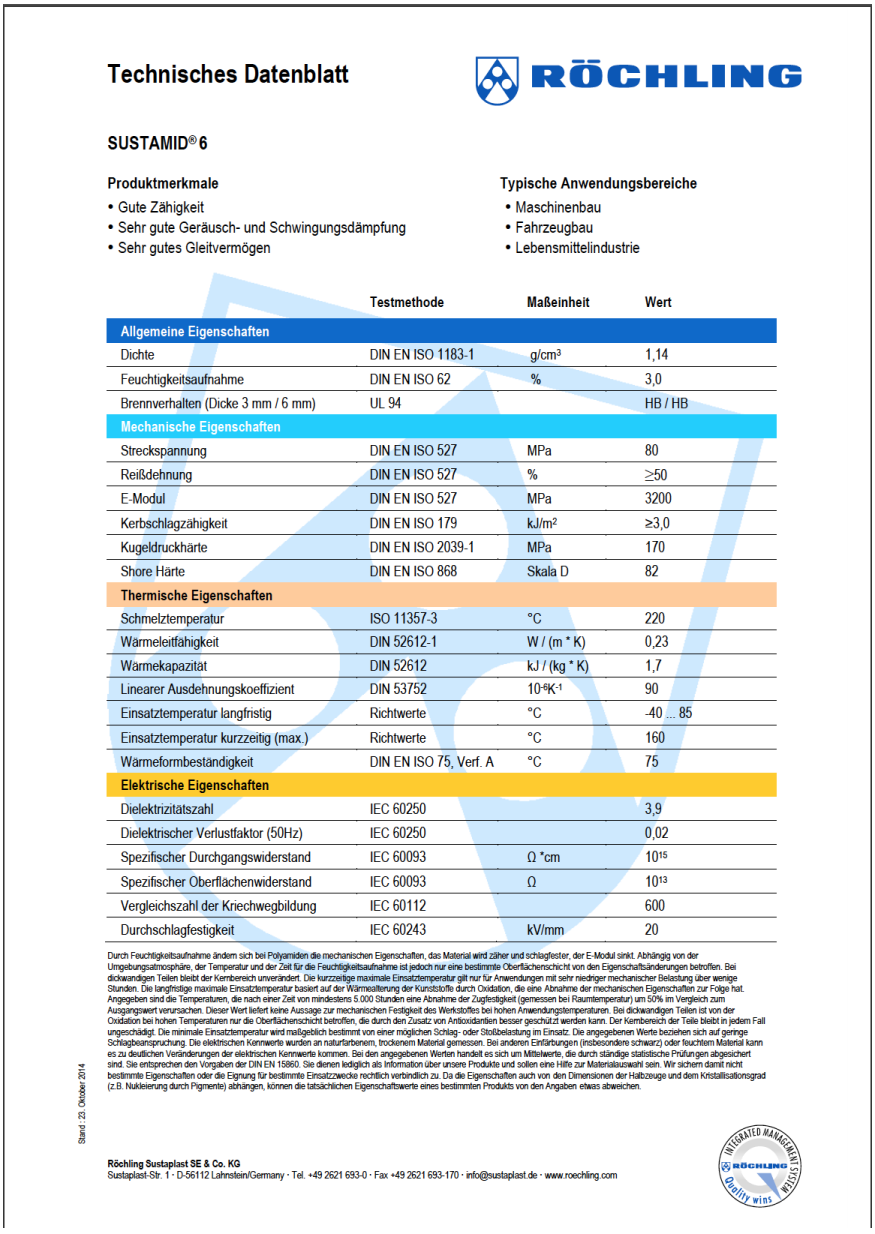

Technisches Datenblatt

RÖCHLING

SUSTAMID® 6

Produktmerkmale
- Gute Zähigkeit
- Sehr gute Geräusch- und Schwingungsdämpfung
- Sehr gutes Gleitvermögen

Typische Anwendungsbereiche
- Maschinenbau
- Fahrzeugbau
- Lebensmittelindustrie

	Testmethode	Maßeinheit	Wert
Allgemeine Eigenschaften			
Dichte	DIN EN ISO 1183-1	g/cm³	1,14
Feuchtigkeitsaufnahme	DIN EN ISO 62	%	3,0
Brennverhalten (Dicke 3 mm / 6 mm)	UL 94		HB / HB
Mechanische Eigenschaften			
Streckspannung	DIN EN ISO 527	MPa	80
Reißdehnung	DIN EN ISO 527	%	≥50
E-Modul	DIN EN ISO 527	MPa	3200
Kerbschlagzähigkeit	DIN EN ISO 179	kJ/m²	≥3,0
Kugeldruckhärte	DIN EN ISO 2039-1	MPa	170
Shore Härte	DIN EN ISO 868	Skala D	82
Thermische Eigenschaften			
Schmelztemperatur	ISO 11357-3	°C	220
Wärmeleitfähigkeit	DIN 52612-1	W / (m * K)	0,23
Wärmekapazität	DIN 52612	kJ / (kg * K)	1,7
Linearer Ausdehnungskoeffizient	DIN 53752	$10^{-6}K^{-1}$	90
Einsatztemperatur langfristig	Richtwerte	°C	-40 ... 85
Einsatztemperatur kurzzeitig (max.)	Richtwerte	°C	160
Wärmeformbeständigkeit	DIN EN ISO 75, Verf. A	°C	75
Elektrische Eigenschaften			
Dielektrizitätszahl	IEC 60250		3,9
Dielektrischer Verlustfaktor (50Hz)	IEC 60250		0,02
Spezifischer Durchgangswiderstand	IEC 60093	Ω *cm	10^{15}
Spezifischer Oberflächenwiderstand	IEC 60093	Ω	10^{13}
Vergleichszahl der Kriechwegbildung	IEC 60112		600
Durchschlagfestigkeit	IEC 60243	kV/mm	20

Durch Feuchtigkeitsaufnahme ändern sich bei Polyamiden die mechanischen Eigenschaften, das Material wird zäher und schlagfester, der E-Modul sinkt. Abhängig von der Umgebungsatmosphäre, der Temperatur und der Zeit für die Feuchtigkeitsaufnahme ist jedoch nur eine bestimmte Oberflächenschicht von den Eigenschaftsänderungen betroffen. Bei dickwandigen Teilen bleibt der Kernbereich unverändert. Die kurzzeitige maximale Einsatztemperatur gilt nur für Anwendungen mit sehr niedriger mechanischer Belastung über wenige Stunden. Die langfristige maximale Einsatztemperatur basiert auf der Wärmealterung der Kunststoffe durch Oxidation, die eine Abnahme der mechanischen Eigenschaften zur Folge hat. Angegeben sind die Temperaturen, die nach einer Zeit von mindestens 5.000 Stunden eine Abnahme der Zugfestigkeit (gemessen bei Raumtemperatur) um 50% im Vergleich zum Ausgangswert verursachen. Dieser Wert liefert keine Aussage zur mechanischen Festigkeit des Werkstoffes bei hohen Anwendungstemperaturen. Bei dickwandigen Teilen ist von der Oxidation bei hohen Temperaturen nur die Oberflächenschicht betroffen, die durch den Zusatz von Antioxidantien besser geschützt werden kann. Der Kernbereich der Teile bleibt in jedem Fall ungeschädigt. Die minimale Einsatztemperatur wird maßgeblich bestimmt von einer möglichen Schlag- oder Stoßbelastung im Einsatz. Die angegebenen Werte beziehen sich auf geringe Schlagbeanspruchung. Die elektrischen Kennwerte wurden an naturfarbenem, trockenem Material gemessen. Bei anderen Einfärbungen (insbesondere schwarz) oder feuchtem Material kann es zu deutlichen Veränderungen der elektrischen Kennwerte kommen. Bei den angegebenen Werten handelt es sich um Mittelwerte, die durch ständige statistische Prüfungen abgesichert sind. Sie entsprechen den Vorgaben der DIN EN 15860. Sie dienen lediglich als Information über unsere Produkte und sollen eine Hilfe zur Materialauswahl sein. Wir sichern damit nicht bestimmte Eigenschaften oder die Eignung für bestimmte Einsatzzwecke rechtlich verbindlich zu. Da die Eigenschaften auch von den Dimensionen der Halbzeuge und dem Kristallisationsgrad (z.B. Nukleierung durch Pigmente) abhängen, können die tatsächlichen Eigenschaftswerte eines bestimmten Produkts von den Angaben etwas abweichen.

Stand: 23. Oktober 2014

Röchling Sustaplast SE & Co. KG
Sustaplast-Str. 1 · D-56112 Lahnstein/Germany · Tel. +49 2621 693-0 · Fax +49 2621 693-170 · info@sustaplast.de · www.roechling.com

INTEGRATED MANAGEMENT SYSTEM RÖCHLING Quality wins

Figure C.9: PA6 data as stated by supplier

C.2.3. POM

Technical Data Sheet

RÖCHLING

SUSTARIN® C

Product characteristics

- Good chemical resistance
- High dimensional stability
- Low moisture absorption

Product applications

- Mechanical engineering
- Electrical industry
- Medical engineering

	Test method	Unit	Value
General properties			
Density	DIN EN ISO 1183-1	g / cm^3	1,41
Water absorption	DIN EN ISO 62	%	0,2
Flammability (Thickness 3 mm / 6 mm)	UL 94		HB / HB
Mechanical properties			
Yield stress	DIN EN ISO 527	MPa	67
Elongation at break	DIN EN ISO 527	%	30
Tensile modulus of elasticity	DIN EN ISO 527	MPa	2800
Notched impact strength	DIN EN ISO 179	kJ / m^2	6
Shore hardness	DIN EN ISO 868	scale D	81
Thermal properties			
Melting temperature	ISO 11357-3	°C	165
Thermal conductivity	DIN 52612-1	W / (m * K)	0,31
Thermal capacity	DIN 52612	kJ / (kg * K)	1,50
Coefficient of linear thermal expansion	DIN 53752	10^{-6} / K	110
Service temperature, long term	Average	°C	-50 … 100
Service temperature, short term (max.)	Average	°C	140
Heat deflection temperature	DIN EN ISO 75, Verf. A, HDT	°C	110
Electrical properties			
Dielectric constant	IEC 60250		3,8
Dielectric dissipation factor (50 Hz)	IEC 60250		0,002
Volume resistivity	DIN EN 62631-3-1	Ω * cm	10^{13}
Surface resistivity	DIN EN 62631-3-2	Ω	10^{13}
Comparative tracking index	IEC 60112		600
Dielectric strength	IEC 60243	kV / mm	40

The short-term maximum application temperature only applies to very low mechanical stress for a few hours. The long-term maximum application temperature is based on the thermal ageing of plastics by oxidation, resulting in a decrease of the mechanical properties. This applies to an exposure to temperatures for at least 5.000 hours causing a 50% loss of the tensile strength from the original value (measured at room temperature). This value says nothing about the mechanical strength of the material at high application temperatures. In case of thick-walled parts, only the surface layer is affected by oxidation from high temperatures. With the addition of antioxidants, a better protection of the surface layer is achieved. In any case, the center area of the material remains unaffected. The minimum application temperature is basically influenced by possible stress factors like impact and/or shock under application. The values stated refer to an minimum degree of impact stress. The electrical properties as stated result from measurements on natural, dry material. With other colours (in particular black) or saturated material, there may be clear differences in the electrical properties. The data stated above are average values ascertained by statistical tests on a regular basis. They are in accordance with DIN EN 15860. They serve as information about our products and are presented as a guide to choose from our range of materials. This, however, does not include an assurance of specific properties or the suitability for particular application purposes that are legally binding. Since the properties also depend on the dimension of the semi-finished products and the degree of crystallization (e.g. nucleating by pigments), the actual values of the properties of a particular product may differ from the indicated values.

Röchling Sustaplast SE & Co. KG
Sustaplast-Str. 1 • D-56112 Lahnstein/Germany • Tel. +49 2621 693-0 • Fax +49 2621 693-170 • info@sustaplast.de • www.roechling.com
Date: 18/05/2016 Version: 1.0.0

Figure C.10: POM data as stated by supplier

C.2.4. PU

C

Herikon
HIGH TECHNICAL POLYURETHANE & SILICONE PRODUCTS

Technical Data Sheet (platen)-Polyurethaan type HK-00501

Hardness shore (SHORE HARDHEID)	°A	65°	75°	85°	95°
Tensile strength (TREKSTERKTE)	MPa	25,00	40,00	40,00	40,00
Elongation at break (REK TOT BREUK)	%	450	500	500	500
Tear strength with nick (SCHEURSTERKTE)	KN/m	10	25	40	60
Resilience	%	--	30	30	30
Abrasion loss (MATERIAALAFNAME)	mm3 loss	70	45	50	55
*Compression set Method B ** (SAMENDRUKBAARHEID)	%	15	20	25	30
Minimum temp.	°C	-40	-40	-40	-40
Maximum temp.	°C	70	70	70	70
Specific Gravity (SOORTELIJK GEWICHT)		1,24	1,24	1,24	1,24

** 25% deflexion 22 hours at 70°C.*

HK-00501

Type HK-00501 is een polyurethaansoort, die voor de meest uitlopende produkten kan worden toegepast, zolang de belasting niet te hoog is. U moet hierbij denken aan plaatmateriaal, stalen strips en vormprodukten.

Hardheidsbereik : 65° Shore A tot 95° Shore A
Temperatuurbereik : -40°C / + 70°C continue

Herikon is member of Groen Industrial Group
Location Almelo: Edisonstraat 11 , 7601 PS Almelo
T +31 (0)546 486 486 • F +31 (0)546 486 480
info@herikon.nl • www.herikon.nl
Location Leerdam: Techniekweg 27a, 4143 HW Leerdam
IBAN: NL14ABNA0479867747 • BIC/Swift-code: ABNANL2A
BTW nr. NL 006974491B01 • KvK Enschede 06044166

Figure C.11: PU data as stated by supplier

C.2.5. ARALDITE

HUNTSMAN
Enriching lives through innovation

C

Advanced Materials

Araldite® 2014-2

Structural Adhesives

TECHNICAL DATA SHEET

Araldite® 2014-2
Two component epoxy paste adhesive

Key properties

- **Grey paste**
- **High temperature and chemical resistance**
- **Very resistant to water and to a wide variety of chemicals**
- **Gap filling, non sagging up to 5mm thickness**

Description

Araldite® 2014-2 is a two component, room temperature curing, thixotropic paste adhesive of high strength with good environmental and excellent chemical resistance. Used for bonding of metals, electronic components, GRP structures and many other items where a higher than normal temperature or more aggressive environment is to be encountered in service.

Product data

Property	2014-2 / A	2014-2 / B	2014-2 (mixed)
*Colour (visual) (A112)**	*beige paste*	*grey paste*	grey paste
Specific gravity	ca. 1.6	ca. 1.5	ca. 1.6
Viscosity at 25°C (Pas)	ca. 100	thixotropic	thixotropic
Pot Life (100 gm at 25°C)	-	-	110 minutes
*Lap shear strength at 25°C (A501)**			*> 14 MPa*

** Specified data are on a regular basis analysed. Data which is described in this document as "typical" is not analysed on a regular basis and is given for information purposes only. Data values are not guaranteed or warranted unless if specifically mentioned.*

Processing

Pretreatment

The strength and durability of a bonded joint are dependant on proper treatment of the surfaces to be bonded.
At the very least, joint surfaces should be cleaned with a good degreasing agent such as acetone, alcohol or other proprietary degreasing agents in order to remove all traces of oil, grease and dirt.
The strongest and most durable joints are obtained by either mechanically abrading or chemically etching ("pickling") the degreased surfaces. Abrading should be followed by a second degreasing treatment.

Mix ratio	Parts by weight	Parts by volume
Araldite® 2014-2 / A	100	100
Araldite® 2014-2 / B	50	50

Araldite® 2014-2 is available in cartridges incorporating mixers and can be applied as ready to use adhesive with the aid of the tool recommended by Huntsman Advanced Materials.

Figure C.12

HUNTSMAN
Enriching lives through innovation

C

Application of adhesive

The resin/hardener mix may be applied manually or robotically to the pretreated and dry joint surfaces. Huntsman's technical support group can assist the user in the selection of an suitable application method as well as suggest a variety of reputable companies that manufacture and service adhesive dispensing equipment.
A layer of adhesive 0.05 to 0.10 mm thick will normally impart the greatest lap shear strength to the joint. Huntsman stresses that proper adhesive joint design is also critical for a durable bond. The joint components should be assembled and secured in a fixed position as soon as the adhesive has been applied.
For more detailed explanations regarding surface preparation and pretreatment, adhesive joint design, and the dual syringe dispensing system, visit www.aralditeadhesives.com

Equipment maintenance

All tools should be cleaned with hot water and soap before adhesives residues have had time to cure. The removal of cured residues is a difficult and time-consuming operation.
If solvents such as acetone are used for cleaning, operatives should take the appropriate precautions and, in addition, avoid skin and eye contact.

Typical times to minimum shear strength

Temperature	°C	10	15	23	40	60	100
Cure time to reach	hours	13	10	5	-	-	-
LSS > 1MPa	minutes	-	-	-	90	20	5
Cure time to reach	hours	25	15	8	2	-	-
LSS > 10MPa	minutes	-	-	-	-	30	6

LSS = Lap shear strength.

Typical cured properties

Unless otherwise stated, the figures given below were all determined by testing standard specimens made by lap-jointing 114 x 25 x 1.6 mm strips of aluminium alloy. The joint area was 12.5 x 25 mm in each case.
The figures were determined with typical production batches using standard testing methods. They are provided solely as technical information and do not constitute a product specification.

Average lap shear strengths of typical metal-to-metal joints (ISO 4587) (typical average values)

Cured for 16 hours at 40°C , tested at 23°C, pretreatment - Sand blasting and degreasing

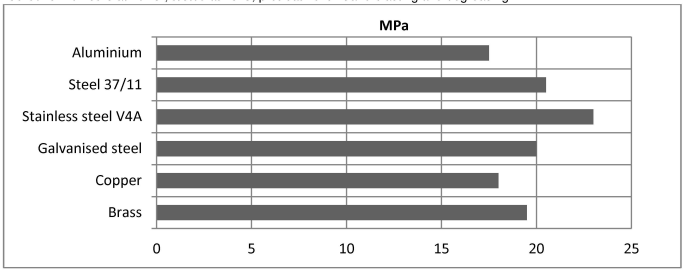

Figure C.13

HUNTSMAN
Enriching lives through innovation

Average lap shear strengths of typical plastic-to-plastic joints (ISO 4587) (typical average values)

Cured for 16 hours at 40°C and tested at 23°C. Pretreatment - Lightly abrade and alcohol degrease.

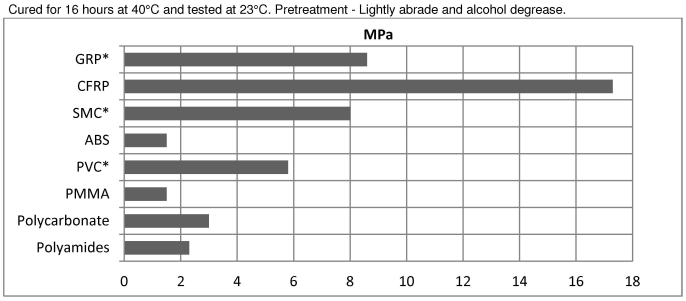

: substrate failure

Lap shear strength versus temperature (ISO 4587) (typical average values)

On aluminium. Pretreatment :sandblasting Cure: (a) = 16 hours at 40°C; (b) = 1 hour at 80°C

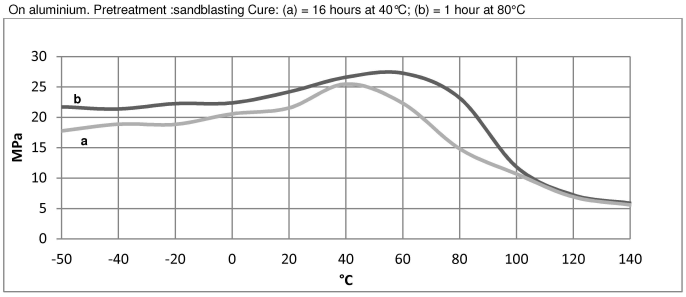

Glass transition temperature (typical average values)

Cure 16 hours at 40°C (DMA)	ca. 69°C
Cure: 24 hours at 23°C + 1 hour at 80°C (DSC)	ca. 85°C

Shear modulus (ISO 6721) (typical average values) Cure: 16 hours/40°C

50°C - 1.2 GPa
75°C - 32 MPa
100°C - 25 MPa
125°C - 22 MPa

Flexural Properties (ISO 178) (typical average values) Cure 16 hours/ 40ºC ,tested at 23°C

Flexural Strength	60 MPa
Flexural Modulus	3500 MPa

Figure C.14

HUNTSMAN
Enriching lives through innovation

Tensile Properties (ISO 527) (typical average values) Cure 16 hours/ 40ºC , tested at 23 ℃

Tensile Strength	30 MPa
Tensile Modulus	3100 MPa
Elongation at break	0,9 %

Additional electrical properties (typical average values)	Test values	Test methods
Dielectric strength (kV/mm)	25	ASTM D-149
Surface resistivity (Ohm)	4.6 E+16	IEC 60093
Volume resistivity (Ohm-cm)	2.7 E+15	IEC 60093
Dielectric constant at 60Hz	4.0	IEC 60250
Loss tangent, % at 60Hz	1.3	IEC 60250

Lap shear strength versus immersion in various media (ISO 4587) (typical average values)

On aluminium, cured for 16 hours at 40 °C and tested at 23°C. Pretreatment - Sand blasting
Unless otherwise stated, L.S.S. was determined after immersion for 30, 60 and 90 days at 23°C

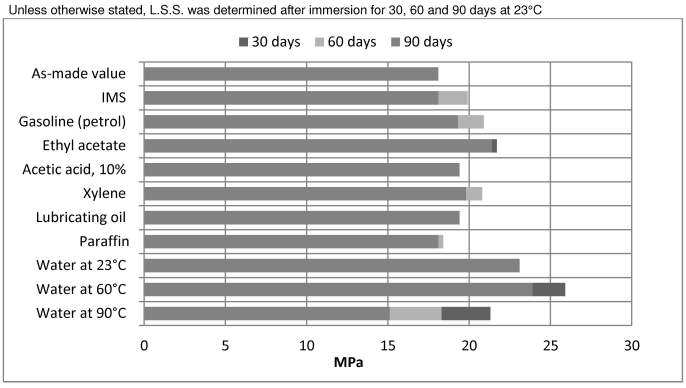

Lap shear strength versus tropical weathering (ISO 4587) (typical average values)

(40℃/ 92% RH), on aluminium, cured for 16 hours at 40 °C and tested at 23°C. Pretreatment - Sand blasting

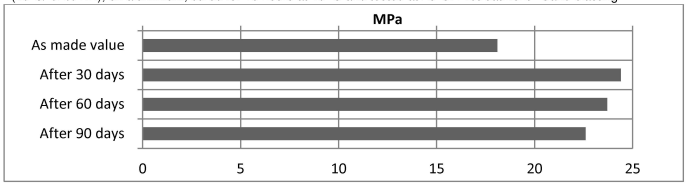

Figure C.15

HUNTSMAN
Enriching lives through innovation

Lap shear strength versus heat ageing (ISO 4587) (typical average values)

On aluminium, cured for 16 hours at 40 °C and tested at 23°C. Pretreatment - Sand blasting

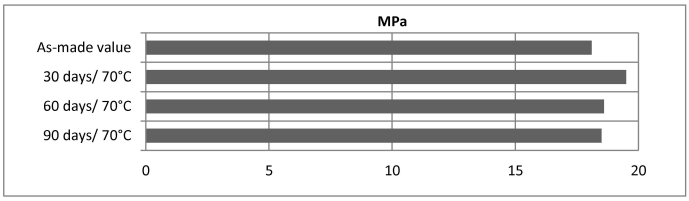

Storage

Araldite® 2014-2 A & B must be stored at room temperature provided the components are stored in sealed containers. The expiry date is indicated on the label.

Handling precautions

Caution

Our products are generally quite harmless to handle provided that certain precautions normally taken when handling chemicals are observed. The uncured materials must not, for instance, be allowed to come into contact with foodstuffs or food utensils, and measures should be taken to prevent the uncured materials from coming in contact with the skin, since people with particularly sensitive skin may be affected. The wearing of impervious rubber or plastic gloves will normally be necessary; likewise the use of eye protection. The skin should be thoroughly cleansed at the end of each working period by washing with soap and warm water. The use of solvents is to be avoided. Disposable paper - not cloth towels - should be used to dry the skin. Adequate ventilation of the working area is recommended. These precautions are described in greater detail in the Material Safety Data sheets for the individual products and should be referred to for fuller information.

Figure C.16

HUNTSMAN
Enriching lives through innovation

C

QUALITY SYSTEM CERTIFICATION
DNV·GL
ISO 9001

Huntsman Advanced Materials (Switzerland) GmbH
Klybeckstrasse 200
CH - 4057 Basel
Switzerland

Tel: +41 (0)61 299 11 11
Fax: +41 (0)61 299 11 12

www.araldite adhesives.com

Huntsman Advanced Materials warrants only that its products meet the specifications agreed with the user. Specified data are analysed on a regular basis. Data which is described in this document as 'typical' or 'guideline' is not analysed on a regular basis and is given for information purposes only. Data values are not guaranteed or warranted unless if specifically mentioned.

The manufacture of materials is the subject of granted patents and patent applications; freedom to operate patented processes is not implied by this publication.

While all the information and recommendations in this publication are, to the best of Huntsman Advanced Material's knowledge, information and belief, accurate at the date of publication, **nothing herein is to be construed as a warranty, whether express or implied, including but without limitation, as to merchantability or fitness for a particular purpose**. **In all cases, it is the responsibility of the user to determine the applicability of such information and recommendations and the suitability of any product for its own particular purpose.**

The behaviour of the products referred to in this publication in manufacturing processes and their suitability in any given end-use environment are dependent upon various conditions such as chemical compatibility, temperature, and other variables, which are not known to Huntsman Advanced Materials. It is the responsibility of the user to evaluate the manufacturing circumstances and the final product under actual end-use requirements and to adequately advise and warn purchasers and users thereof.

Products may be toxic and require special precautions in handling. The user should obtain Safety Data Sheets from Huntsman Advanced Materials containing detailed information on toxicity, together with proper shipping, handling and storage procedures, and should comply with all applicable safety and environmental standards.

Hazards, toxicity and behaviour of the products may differ when used with other materials and are dependent on manufacturing circumstances or other processes. Such hazards, toxicity and behaviour should be determined by the user and made known to handlers, processors and end users.

Except where explicitly agreed otherwise, the sale of products referred to in this publication is subject to the general terms and conditions of sale of Huntsman Advanced Materials LLC or of its affiliated companies including without limitation, Huntsman Advanced Materials (Europe) BVBA, Huntsman Advanced Materials Americas Inc., Huntsman Advanced Materials (UAE) FZE, Huntsman Advanced Materials (Guangdong) Company Limited, and Huntsman Advanced Materials (Hong Kong) Ltd.

Huntsman Advanced Materials is an international business unit of Huntsman Corporation. Huntsman Advanced Materials trades through Huntsman affiliated companies in different countries including but not limited to Huntsman Advanced Materials LLC in the USA and Huntsman Advanced Materials (Europe) BVBA in Europe.

All trademarks mentioned are either property of or licensed to Huntsman Corporation or an affiliate thereof in one or more, but not all, countries.

Copyright © 2017 Huntsman Corporation or an affiliate thereof. All rights reserved

Figure C.17: Araldite data as stated by supplier

D

DERIVATIONS

D.1. DEFINITION AXES

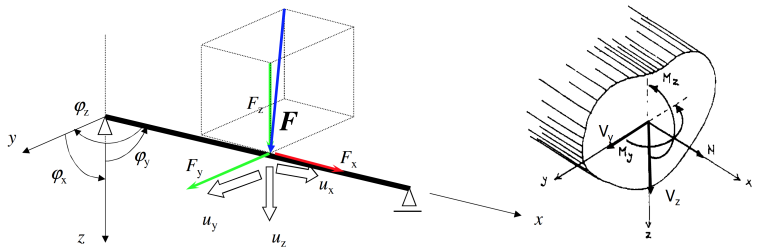

Figure D.1: Global and sectional definitions, based on Hartsuijker, 2001

D.2. MECHANICAL SCHEME PORTAL FRAME

When applying a distributed load q on an element with length L, this will result in a parabolic moment distribution seen in Figure D.2. This results in a maximum moment of

$$M = \frac{1}{8} q L^2 \tag{D.1}$$

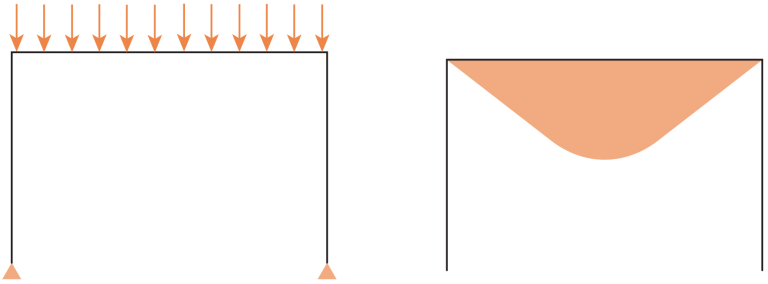

Figure D.2: Schematization moment non-rigid connection

D

Applying the exact same load on a rigid portal frame, will result in a smaller maximum moment, because part of the bending moment is taken up by the rigid corners. This can be seen in Figure D.3. The exact magnitude of the moment depends on the stiffness of the joints in the corner.

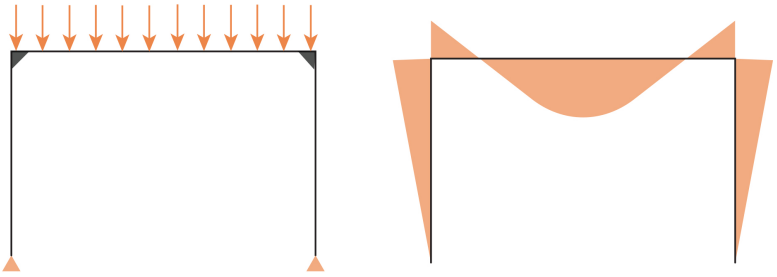

Figure D.3: Schematization moment from distributed load portal frame connection

Due to the rigid connections, the portal frame with height h can also take up vertical loads, as seen in Figure D.4. The magnitude of the moment becomes $F \cdot h$.

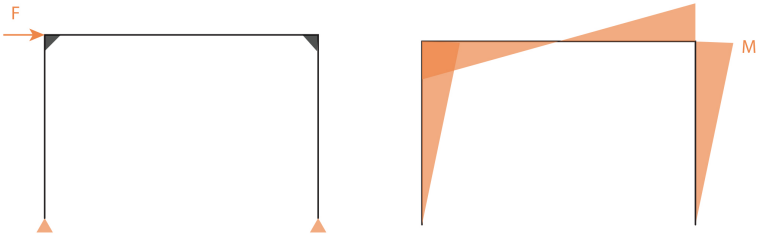

Figure D.4: Schematization moment from vertical load portal frame connection

D.3. DEFLECTION FOUR POINT BENDING

The theoretical deflection of a beam under four point bending is derived using differential equations. The beam is schematized as seen in Figure D.5(b), consisting of two parts. On the left the beam is modelled simply supported, on the right as a clamped beam, which can translate vertically. The two differential equations are:

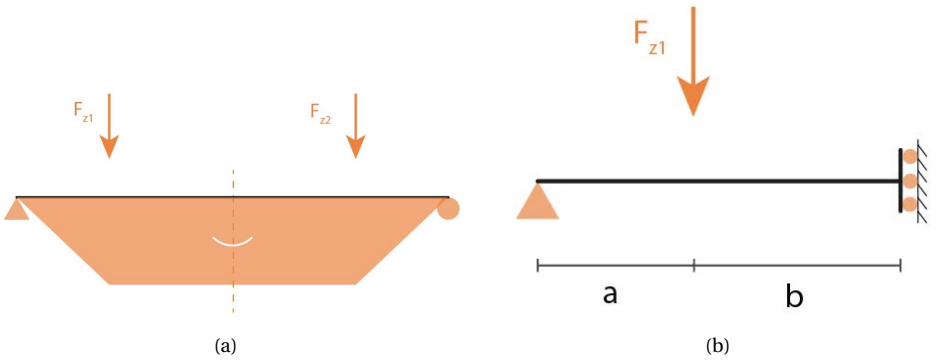

(a) (b)

Figure D.5: Resulting moment due to four point bending test (a) and schematization beam for ODE

$$EI\frac{d^4 w_1}{dx^4} = 0 \tag{D.2}$$

$$EI\frac{d^4 w_2}{dx^4} = 0 \tag{D.3}$$

Solving the differential equations will result in 8 unknowns, so 8 boundary and/or matching conditions are necessary. At $x = 0$ and $x = a+b$ each two boundary conditions apply. Four matching conditions apply, connecting the two fields at $x = a$. The definition of taken shear forces can be seen in Figure D.6. The resulting conditions are as follows:

$$x = 0 \rightarrow w_1 = 0, M_1 = 0 \tag{D.4}$$

$$x = a \rightarrow w_1 = w_2, M_1 = M_2, \phi_1 = \phi_2, V_1 = F + V_2 \tag{D.5}$$

$$x = a+b \rightarrow \phi_2 = 0, V_2 = 0 \tag{D.6}$$

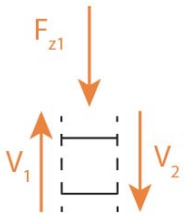

Figure D.6: Definition shear

For field a, this results in a deflection of

$$w_1 = -\frac{Fx^3}{6EI} + \frac{aF(a+2b)x}{2EI} \tag{D.7}$$

And for field b this results in the following formula giving the deflection of the beam. Inserting the values for a, b and F, this will result in the maximum deflection in the middle of the beam.

$$w_2 = -\frac{aFx^2}{2EI} + \frac{aF(a+b)x}{EI} - \frac{a^3F}{6EI} \tag{D.8}$$